SODIUM SPINOR BOSE-EINSTEIN CONDENSATES: ALL-OPTICAL PRODUCTION AND SPIN DYNAMICS

By

JIE JIANG

Bachelor of Science in Optical Information Science
University of Shanghai for Science and Technology
Shanghai, China
2009

Submitted to the Faculty of the
Graduate College of
Oklahoma State University
in partial fulfillment of
the requirements for
the Degree of
DOCTOR OF PHILOSOPHY
December, 2015

SODIUM SPINOR BOSE-EINSTEIN CONDENSATES:
ALL-OPTICAL PRODUCTION AND SPIN DYNAMICS

Dissertation Approved:

Dr. Yingmei Liu

Dissertation Advisor

Dr. Albert T. Rosenberger

Dr. Gil Summy

Dr. Weili Zhang

ACKNOWLEDGMENTS

I would like to first express my sincere gratitude to my thesis advisor Dr. Yingmei Liu, who introduced ultracold quantum gases to me and guided me throughout my PhD study. I am greatly impressed by her profound knowledge, persistent enthusiasm and love in BEC research. It has been a truly rewarding and privilege experience to perform my PhD study under her guidance.

I also want to thank my committee members, Dr. Albert Rosenberger, Dr. Gil Summy, and Dr. Weili Zhang for their advice and support during my PhD study. I thank Dr. Rosenberger for the knowledge in lasers and laser spectroscopy I learnt from him. I thank Dr. Summy for his support in the department and the academic exchange with his lab. Dr. Zhang offered me a unique opportunity to perform microfabrication in a cleanroom, which greatly extended my research experience.

During my more than six years study at OSU, I had opportunities to work with many wonderful people and the team members in Liu's lab have been providing endless help for me which is important to my work. Many thanks extend to my current colleagues Lichao Zhao, Tao Tang, Zihe Chen, and Micah Webb as well as our former members Zongkai Tian, Jared Austin, and Alex Behlen.

Moreover, I would like to thank our best staffs in the department of physics. Susan is super nice and always helps students to deal with different problems. Tamra has helped us a lot on ordering various lab equipments. I also want to thank Sandra who just relocated to registration office, Alisha, Melissa, and Charles.

I also want to express my appreciation to Mike who just retired, Larry, and Randy in machine shop. They have helped us to build many custom designed parts espe-

cially the Zeeman slower, which are essential components in our experimental system. Furthermore, I would like to thank our senior technician Warren. Warren was the first person came into my mind if we needed something or help in the lab. I also want to say thank you to him for allocating a spot to me in PS354 in my first year study.

Last but not least, I am greatly indebted to my father Zhonghua Jiang and my mother Limei Wu for their endless love and support. Finally I want to thank my beloved Yingxia Hu, who has been with me all the time, shined my life with her optimism and smile, and encouraged me during every dark moment I encountered. I dedicate this thesis to them.

Name: JIE JIANG

Date of Degree: DECEMBER, 2015

Title of Study: SODIUM SPINOR BOSE-EINSTEIN CONDENSATES: ALL-OPTICAL PRODUCTION AND SPIN DYNAMICS

Major Field: PHOTONICS

Abstract: In this thesis, I present a novel experimental system and an optimal experimental scheme for an all-optical production of a sodium spinor Bose-Einstein condensate (BEC). With this scheme, I demonstrate that the number of atoms in a pure BEC can be greatly boosted by a factor of 5 over some widely used schemes in a simple single-beam or crossed-beam optical trap. Our scheme avoids technical challenges associated with some all-optical BEC methods and may be applicable to other optically trappable atomic species. I also discuss an upper limit for evaporative cooling efficiency in all-optical BEC approaches, and a good agreement between our theoretical model and experimental data.

In addition, we study the spin-mixing dynamics and phase diagrams of spinor BECs immersed in a microwave dressing field. Due to the interplay of spin-dependent interactions and the quadratic Zeeman energy induced by the microwave field, two types of quantum phase transitions are observed in our F=1 antiferromagnetic sodium spinor BEC system. We also demonstrate that many previously unexplored regions in the phase diagram of spinor condensates can be investigated by adiabatically tuning the microwave field across one of the observed quantum phase transitions. This method overcomes two major experimental challenges associated with some widely used methods, and is applicable to other atomic species. Agreements between our data and the mean-field theory for spinor Bose gases are also discussed.

TABLE OF CONTENTS

Chapter Page

LIST OF TABLES

Table Page

LIST OF FIGURES

Figure Page

CHAPTER 1

INTRODUCTION

1.1 What is a Bose-Einstein condensate?

Atomic Bose-Einstein condensates (BECs) are gases which are so cold that all the atoms collapse into the same quantum state, becoming essentially indistinguishable from one another. In other words, all atoms in BECs have a single collective wave-function for their spatial degrees of freedom. BEC research started from early 1920s. In 1924, Bose sent Einstein a paper to show his idea on deriving the Plank distribution law using the statistical mechanics of photons. Einstein soon realized the importance of this work and extended Bose's idea to the quantum theory of bosonic particles. They predicted a new phase transition, Bose-Einstein condensation, which should happen at an extremely low temperature.

The process of an atomic system undergoing a phase transition from a thermal gas to a BEC can be simply described as follows: a) At high temperature, the system can be understood in a particle picture characterized by the inter-particle distance d or particle density; b) When the temperature of the system is lowered, d becomes smaller and the system can be well characterized by individual matter wave packet with deBroglie wavelength λ_{dB}; c) At the BEC transition temperature, d is comparable to λ_{dB} and a large fraction of particles start to occupy in the same quantum state. The macroscopic occupation in the lowest energy state is called a Bose-Einstein condensation. At zero-temperature, a pure condensate with all particles being in the ground state can be realized.

1.1.1 Experimental realization of Bose-Einstein condensates

Scientists underwent a long road to experimentally achieve a temperature as low as possible in the last century, and each advance towards the absolute zero temperature led to newer and richer physics. In July 1908, the Netherland physicist Heike Kamerlingh Onnes was the first to successfully liquefy helium and achieved a temperature of $\sim$1.5 K, which was the coldest temperature on earth at that time. Three years later, with the temperature in Kelvin regime, Onnes discovered the superconductivity in Mercury samples. Onnes was awarded a Nobel prize in physics in 1913 for his investigations on the properties of matter at low temperatures. In 1938, superfluidity in helium-4 was reported by Kapitsa, Allen, and Misener at the temperature of 2.2 K [1, 2]. In the same year, Fritz London and Laszlo Tisza provided an explanation for superfluid helium by using the ideas of Bose-Einstein condensation [3, 4], which indicated the macroscopic quantum behavior of a BEC. In 1972, superfluidity in helium-3 was revealed by Lee, Richardson, and Osheroff at the temperature of 2 mK [5, 6].

In 1975, the idea of laser cooling technique was first proposed by Wineland and Dehmelt [7], and Hänsh and Schawlow [8], which showed that laser light could be used to cool atoms and ions. Three years later, this idea was first demonstrated by Wineland, Drullinger, and Walls [9]. In 1980s, laser cooling and trapping techniques experienced a rapid development and many well-known innovations were invented to further cool down the atoms. In 1982, W. D. Phillips and his colleagues at NIST developed a Zeeman slower to effectively slow down the sodium atoms [10]. In 1985, optical molasses was realized at Bell Labs by Steven Chu and his co-workers to further low down the temperature of sodium atoms to $\sim$240 μK [11], which approached the Doppler cooling limit. In 1987, a Magneto-optical trap was first demonstrated by Rabb and co-workers [12]. A year later, Cohen-Tannoudji [13] and Steven Chu [14] revealed the first sub-Doppler cooling. Laser cooling was awarded a Nobel prize in

physics in 1997.

It took scientists almost 70 years to experimentally realize BECs after Bose and Einstein made the prediction. The first BEC of rubidium atoms was achieved by Eric Cornell and Carl Wieman in 1995, while the first sodium BEC was created by Wolfgang Ketterle in the same year [15, 16, 17]. They shared the Nobel prize in Physics in 2001. The realization of BECs is an important breakthrough in physics, not only because a BEC represents a new form of matter, but also because it makes the observation of microscopic quantum effects on a macroscopic scale possible. Up to now, BECs have been successfully realized in Rubidum [15], Sodium [16], Lithium [17], Potassium [18], Cesium [19], Ytterbium [20], Calcium [21], Strontium [22, 23]. The first degenerate Fermi gases was achieved in JILA in 1999 [24] and molecular BECs were demonstrated four years later in 2003 [25, 26, 27].

1.1.2 A brief review of experiments with ultracold atoms

Ultracold quantum gases have led to a revolutionary change to AMO (atomic, molecular, and optical) physics community. And BECs have been applied to a lot of research areas, such as many-body physics, precision measurements, quantum information science, and quantum optics. The research of ultracold atoms underwent a fast growth since its first experimental realization. Here some representative experiments are listed. The beauty of a BEC is that it provides scientists a highly controllable experimental system that can be applied to investigate interactions among atoms and reveal quantum behaviors in a macroscopic scale. Weak atomic interactions are responsible for non-linear phenomena such as the pioneering BEC vortices experiments, which indicate a signature of the superfluidity of BECs [28, 29, 30]. After the first observation of Feshbach resonances that can tune the interaction between atoms [31], Feshbach resonances have been extended to form various molecular BECs from paired fermions and enriched the study of BEC-BCS crossover region [32]. In addition, the

matter-wave nature of a BEC makes it possible to produce a coherent beam of Bose-condensed atoms instead of photons, which is known as the atom laser. The first atom laser was developed by Ketterle's group in MIT [33] and the pursuit of a truly continuous wave (CW) atom laser never stops [34, 35, 36]. Besides this, since BECs are highly controllable on the phase and amplitude of matter waves, they have been applied to generate new atom interferometry for high precision measurements, for example, measuring the Newtonian gravitational constant [37]. The Cold Atom Laboratory of NASA will even be launched into the International Space Station to study ultracold quantum gases in the microgravity environment in 2016.

Another active field in the BEC research is to investigate ultracold quantum gases in optical lattices. An optical lattice is a standing wave formed by the interference of a pair of laser beams. If multiple pairs of laser beams are applied in an experimental system, it is possible to mimic different crystal structure of a material by simply changing the geometric parameters of the lattice laser beams. Up to now, many different types of optical lattices have been achieved, such as a cubic optical lattice [38], a triangular optical lattice [39], a honeycomb optical lattice [40], and a Kagome optical lattice [41]. One of the most famous experiments performed with a BEC in optical lattices was the demonstration of a superfluid (SF) to Mott-insulator (MI) phase transition [42]. The phase transition was realized by changing the lattice laser beam intensity, which tuned the tunneling rate and the on-site interactions. SF-MI quantum phase transitions were also demonstrated in one-dimensional (1D) and two-dimensional (2D) systems [43, 44]. Furthermore, the detection of SF-MI phase transitions was improved to single-atom level in 2010 [45]. Studying quantum computation with neutral atoms trapped in optical lattices being qubits has also attracted a lot of interest. The single-site addressability in optical lattices has been carried out and plays an important role in realizing a quantum computer [46, 47, 48]. Moreover, an optical lattice clock has been experimentally achieved and its measurement

is based on the frequency of an optical transition within atoms trapped in optical lattices [49]. An world record optical lattice clock with accuracy and stability at the 10^{-18}-s level was achieved in JILA one year ago [50].

There are many BEC research groups worldwide. It is expected that a lot of exciting applications with BECs will be realized in the near future, such as atom lasers, high precision magnetometers, and quantum computers.

1.2 Spinor condensates

A spinor condensate is a BEC with multiple spin components among which coherent interconversions must exist. In early BEC experiments, magnetic traps were used to confine atoms in one Zeeman sub-level, which froze the spin degree of freedom of atoms. By using an optical trap to release the spin degree of freedom, the first spinor condensate was experimentally demonstrated by Stamper-Kurn with F=1 sodium atoms in 1998 [51]. Three years later, the first rubidium spinor condensate was realized in Georgia Tech by using an all-optical BEC production method [52].

For F=1 spinor condensates, such as those realized in our experimental system, their wavefunctions have a vector order parameter and their Hamiltonian in an external field may be expressed as

$$H = \sum_{i=1}^{N} \left[\frac{p_i^2}{2m} + V_{ext}(\vec{r_i}) + E_Z \right] + \frac{1}{2} \sum_{i=1}^{N} U_{int}. \tag{1.1}$$

Here V_{ext}, E_Z, and U_{int} represent external trapping potential such as an optical dipole trap, Zeeman energy shift due to an external field, and the interaction between two atoms during collisions, respectively. N is the number of atoms in the condensate and m is the mass of the atoms.

A F=1 spinor condensate consists of three spin components, $m_F = -1, 0, +1$ states, reflecting its three magnetic Zeeman sublevels. The atomic interactions are dominated by two-body s-wave collisions in a spinor condensate. According to Ref. [53,

54], the general form of the contact interaction between two identical bosons due to s-wave collisions may be expressed as

$$U_{int}(\vec{r_1} - \vec{r_2}) = \delta(\vec{r_1} - \vec{r_2}) \sum_{f=0}^{2F} (g_f \mathbf{P}_f). \tag{1.2}$$

The strength of the interaction is

$$g_f = \frac{4\pi\hbar^2 a_f}{m}, \tag{1.3}$$

where a_f is the s-wave scattering length in the total spin f channel and $\vec{f} = \vec{F_1} + \vec{F_2}$, $\mathbf{P}_f$ is the projection operator which projects a pair of atoms into a total hyperfine spin f state and $\sum_{f=0}^{2F} \mathbf{P}_f = 1$ for identical bosons. Because of the symmetry requirements for identical Bosons, only $f = 0$ or 2 channels are allowed for a F=1 spinor condensate. From the composition law of spin operators, we can obtain [55, 56]

$$\vec{F_1} \cdot \vec{F_2} = \frac{\vec{f}^2 - \vec{F_1}^{\,2} - \vec{F_2}^{\,2}}{2} = \frac{f(f+1) - 2F(F+1)}{2}, \tag{1.4}$$

where $\vec{F_i}$ is the spin operator for atom i. Thus we can have the relation $\vec{F_1} \cdot \vec{F_2} = \sum_{f=0}^{2F} \lambda_f \mathbf{P}_f$, where $\lambda_f = \frac{1}{2}[f(f+1) - 2F(F+1)]$. For F=1 atoms,

$$\vec{F_1} \cdot \vec{F_2} = \sum_{f=0}^{2F} \lambda_f \mathbf{P}_f = \mathbf{P}_2 - 2\mathbf{P}_0, \tag{1.5}$$

and

$$\sum_{f=0}^{2F} \mathbf{P}_f = 1 = \mathbf{P}_2 + \mathbf{P}_0. \tag{1.6}$$

Together with Eq. (1.5) and Eq. (1.6), it is possible to rewrite Eq. (1.2) as [53, 54],

$$\begin{aligned} U_{int} &= \delta(\vec{r_1} - \vec{r_2}) \sum_{f=0}^{2F} (g_f \mathbf{P}_f) \\ &= \delta(\vec{r_1} - \vec{r_2})(g_0 \mathbf{P}_0 + g_2 \mathbf{P}_2) \\ &= \delta(\vec{r_1} - \vec{r_2})(c_0 + c_2 \vec{F_1} \cdot \vec{F_2}). \end{aligned} \tag{1.7}$$

The contribution to the Hamiltonian of a spinor condensate due to contact interactions can thus be illustrated by two terms: the spin-independent term c_0 and the

spin-dependent term characterized by c_2. c_0 and c_2 are given by

$$c_0 = \frac{2g_2 + g_0}{3} = \frac{4\pi\hbar^2}{m}\frac{2a_{f=2} + a_{f=0}}{3}, \tag{1.8}$$

and

$$c_2 = \frac{g_2 - g_0}{3} = \frac{4\pi\hbar^2}{m}\frac{a_{f=2} - a_{f=0}}{3}. \tag{1.9}$$

The spin-dependent interaction c_2 couples different Zeeman states, which leads to interesting spinor dynamics. The ground state features of the atoms are also dependent of the sign of c_2. Traditionally, F=1 spinor condensates are divided into two different categories based on the sign of c_2: a ferromagnetic spinor BEC with $c_2 < 0$ (i.e., $a_{f=2} < a_{f=0}$), for example, a rubidium system; and an antiferromagnetic spinor BEC with $c_2 > 0$ (i.e., $a_{f=2} > a_{f=0}$), for example, a sodium spinor condensate.

The Zeeman energy term also plays an important role in the spin-mixing dynamics. During the coherent interconversions, the linear Zeeman shift remains the same while the quadratic Zeeman energy is different. The net quadratic Zeeman energy q_{net} is resulted from external magnetic fields (q_B) and/or microwave dressing fields (q_M) experimentally [57, 58].

A spinor BEC has provided exciting opportunities to study quantum magnetism, superfluidity, strong correlations, spin-squeezing, and massive entanglement [55, 56, 59, 60, 61]. One of the known results in spinor BECs is the spin-mixing dynamics, which means that different spin components can exchange population coherently. For instance, two $|F = 1, m_F = 0\rangle$ atoms can collide into one $|F = 1, m_F = -1\rangle$ atom and one $|F = 1, m_F = +1\rangle$ atom. Spin-mixing dynamics and phase diagrams of spinor BECs in free space, due to the interplay of the spin-dependent interaction and q_{net}, have been well studied using sodium [58, 62, 63, 64, 65, 66, 67] and rubidium atoms [68, 69, 70, 71, 72]. In these experiments, the relationship between the spin oscillation period and q_{net} was investigated, a transition from a running phase to an oscillating phase was observed, and the equilibrium states of spinor BECs were studied. In

this thesis, our efforts are focused on the study of spin-mixing dynamics and the phase diagram of antiferromagnetic sodium spinor condensates in free space. We have developed a novel method, and demonstrated that many previously unexplored regions in the phase diagram of F=1 spinor BECs can be investigated by this new method.

1.3 Atomic properties of sodium atoms

Alkali metal and alkali earth atoms are popular choices in BEC experiments due to their well studied spectra and a relatively strong magnetic moment. In our experimental system, we choose sodium atoms as the atomic source. Since the required cooling and trapping beams for sodium atoms are visible (yellow), optical alignments and optimizations in a sodium system may be much easier than those using invisible laser beams (e.g., a rubidium system). Unlike the rubidium systems, sodium spinor BECs are antiferromagnetic spinor BECs which have some unique advantages [55]. Here some basic atomic properties of sodium atoms used in our experiments and this thesis are listed. Most of them are derived from Ref. [73].

Atomic Number	Z	11
Total Nucleons	$Z+N$	23
Atomic Mass	M	22.989 769 280 7(28) amu
Density at 25 °C	ρ	0.97 g/cm^3
Melting Point	T_{M}	97.8 °C
Boiling Point	T_{B}	883 °C
Nuclear Spin	I	3/2

Table 1.1: Some physical properties of sodium atoms.

Transition		$3^2S_{1/2} \rightarrow 3^2P_{3/2}$
Frequency	ω_a	$2\pi \times 508.8487162(13)$ THz
Transition Energy	$\hbar\omega_a$	2.104 429 011(51) eV
Wavelength (Vacuum)	λ	589.158 326 4(15) nm
Wavelength (Air)	λ_{air}	589.000 226(18) nm
Lifetime	τ	16.2492(77) ns
Natural Linewidth	Γ	$2\pi \times 9.7946(46)$ MHz
Recoil Velocity	v_r	2.9461 cm/s
Recoil Energy	ω_r	$2\pi \times 25.002$ kHz
Recoil Temperature	T_r	2.3998 μK
Doppler Temperature	T_D	235.03 μK
Saturation Intensity	I_{sat}	6.2600(21) mW/cm^2
Resonant Cross Section ($\sigma^{\pm}$ light)	σ_0	$1.6573163925(60) \times 10^{-9}$ cm^2

Table 1.2: Some properties of the sodium D_2 line transitions.

1.4 Thesis outline

In this thesis, I report the first production of a sodium spinor BEC in Oklahoma. The spin-mixing dynamics and the phase diagram of F=1 antiferromagnetic spinor BECs are also studied.

The first chapter introduces some basic definitions and knowledge of a BEC and a spinor BEC as well as a short review of experiments using ultracold atoms. Chapter 2 reviews the underlying physics involved in laser cooling and trapping techniques, which are applied in our daily experiment.

Chapter 3 to Chapter 5 describe one of the major achievements of my PhD study: the production of the first sodium spinor condensates in Oklahoma. Since I spent almost 2/3 of my PhD career on building this magic machine from every small pieces, detailed designs, setups, and alignment procedures for various apparatuses are described. Chapter 3 illustrates our ultra-high vacuum system with a pressure in the 10^{-12} Torr range. Chapter 4 elaborates our novel BEC apparatus and designs, which include the optical setup, a Zeeman slower, a magneto-optical trap, imaging systems, and a crossed optical dipole trap. Chapter 5 presents our optimum ODT loading scheme, which demonstrates that the number of atoms in a pure BEC can be greatly boosted by a factor of 5 over some widely used schemes. Our model for evaporative cooling is also shown in this chapter. With our optimum scheme, a pure F=1 BEC of 1.2×10^5 sodium atoms at the temperature of 50 nK is achieved. In addition, Chapter 5 describes our experimental results on the spin-mixing dynamics of F=1 spinor condensates due to the interplay of spin-dependent interactions and the quadratic Zeeman energy.

Chapter 6 studies the equilibrium states of F=1 spinor condensates with the phase diagram of sodium spinor condensates being mapped. Two types of quantum phase transitions in a sodium spinor condensate immersed in a microwave dressing field are observed. In addition, we demonstrate that many previously unexplored regions

in the phase diagram can be investigated by a novel method, i.e., by adiabatically tuning the microwave field across one of the observed quantum phase transitions. This method overcomes two major experimental challenges associated with some widely used methods, and is applicable to other atomic species. Agreements between our data and the mean-field theory for spinor Bose gases are also discussed.

In the end, Chapter 7 summarizes the work accomplished in this thesis, and proposes to study the first-order SF-MI phase transitions in spinor condensates confined by optical lattices.

CHAPTER 2

Laser cooling and trapping

Laser cooling and trapping techniques play important roles in realizing BECs. In this chapter, I review some widely used laser cooling and trapping techniques (such as Doppler cooling, magneto-optical trap (MOT), optical dipole trap (ODT), evaporative cooling) and discuss their applications in our system.

2.1 Doppler cooling

For a two level atomic system, if a laser frequency is close to the atomic resonance, the absorption of a photon leads the atom to its excited state and results in a corresponding momentum kick between them. An atom at its excited state cannot further absorb light and has to return to the ground state by a spontaneous emission. The resulting fluorescence also has a momentum kick, but in a random direction, which leads to an average zero total momentum transfer during the spontaneous emission. The force in this momentum transfer process can be described as [74]

$$\vec{F} = d\vec{p}/dt = \hbar\vec{k}\gamma_a, \tag{2.1}$$

where $\hbar k$ is a momentum kick for one photon. The absorption rate is

$$\gamma_a = \frac{s_0\Gamma/2}{1 + s_0 + (\frac{\delta+\omega_D}{\Gamma/2})^2}. \tag{2.2}$$

Here Γ is the natural linewidth of the atomic transition, $\omega_D = -\vec{k}\cdot\vec{v}$ is the Doppler shift, δ is the detuning of the laser light from the atomic resonance, $s_0 = I/I_{sat}$ is the laser intensity saturation parameter, and $I_{sat} = 6.26$ mW/cm^2 for sodium atoms.

In order to cool down the atoms, we need the force exerted on the atoms always to be opposed to their moving direction and act as a friction force. We now consider atoms traveling in a pair of identical laser beams in opposite directions with their frequencies detuned below the atomic resonance (which is called "red-detuned"). Because of the Doppler effect, atoms traveling towards the laser beam will see it shifted upward and thus are closer to the atomic resonance. On the other hand, atoms moving away from the other beam will see it shifted downward and therefore are out of resonance. As a result, atoms absorb more photons from the laser beam opposite to their traveling direction, and experience a viscous force to slow down their velocity. The force resulted from two counter-propagating laser beams can be described as:

$$\begin{aligned}\vec{F}_{total} = \vec{F}_{+} + \vec{F}_{-} &= \frac{\hbar\vec{k}\Gamma}{2}\frac{s_0}{1+s_0+(\frac{\delta-kv}{\Gamma/2})^2} - \frac{\hbar\vec{k}\Gamma}{2}\frac{s_0}{1+s_0+(\frac{\delta+kv}{\Gamma/2})^2} \\ &= \frac{\hbar\vec{k}\Gamma}{2}\frac{s_0\cdot\frac{16\delta kv}{\Gamma^2}}{(1+s_0)^2+(1+s_0)\frac{8(\delta^2+k^2v^2)}{\Gamma^2}+\frac{16(\delta^2-k^2v^2)}{\Gamma^4}}\end{aligned} \tag{2.3}$$

By neglecting the high order terms, Eq. (2.3) can be simplified as:

$$\vec{F}_{total} \cong \frac{8\hbar k^2\delta s_0/\Gamma}{(1+s_0+(2\delta/\Gamma)^2)^2}\vec{v} = -\alpha\vec{v} \tag{2.4}$$

This optical force is proportional to the atoms' velocity and behaves like a friction force. Noting that, we have to use red-detuned laser beams to decrease the velocity of the atoms. With three pairs of intersecting, orthogonal, and counter-propagating laser beams, atoms moving in different directions can be confined and cooled in a small region, which is well known as the optical molasses [11].

2.2 Doppler and sub-Doppler cooling limit

In the Doppler cooling process, atoms continuously absorb and scatter photons so that cooling and heating both occur in the system. The heating due to spontaneous emissions leads to a lowest temperature that can be achieved with Doppler cooling. The system reaches equilibrium when cooling and heating equal to each other. The

Doppler cooling limit is thus reached, and can be described as [74]

$$T_D = \frac{\hbar\Gamma}{2k_{\mathrm{B}}}. \tag{2.5}$$

For ^{23}Na atoms, the Doppler cooling limit is 235 μK.

Right after the optical molasses was introduced, scientists in NIST found a surprising result that the temperature of a gas of sodium atoms released from optical molasses was much lower than the Doppler limit [75]. A new theory, known as the polarization gradient cooling, was proposed by Claude Cohen-Tannoudji [13] and Steven Chu [14] in 1989. This theory includes laser polarization gradients due to the interference and different ground-state sublevels of the alkali atoms, which mainly contains two models. The first uses a pair of orthogonal linearly-polarized beams, which is called Linear $\perp$ Linear configuration. While the second is described by two orthogonal circularly-polarized beams and is known as $\sigma^+ - \sigma^-$ configuration. Detailed and well explained cooling mechanisms are given by Ref. [13, 14, 74]. Although the viscous damping in sub-Doppler cooling is much larger than that of the Doppler cooling, there is still a limitation due to spontaneous emissions. The sub-Doppler cooling limit is determined by the recoil energy of a photon and can be expressed by [74]

$$T_r = \frac{\hbar^2 k^2}{k_{\mathrm{B}} M}. \tag{2.6}$$

For ^{23}Na atoms, the recoil limit is 2.4 μK.

2.3 Magneto-optical trap (MOT)

Laser is a powerful tool to cool the atoms, however, it is not sufficient to trap the atoms only by using laser light alone. Because the scattering force is heavily dependent on the velocity of the atoms, atoms may inevitably diffuse out of the system. To confine the atoms, a magnetic quadrupole field is applied to the optical molasses to provide an additional position dependent force. Such a trap is well known as the

magneto-optical trap (MOT). MOT was first invented in 1987 [12] and various types of MOTs have been introduced such as a pyramidal MOT [76, 77], a 2-dimensional (2D) MOT [78, 79, 80], and a surface MOT [81, 82]. Here we mainly focus on the widely used 3-dimensional (3D) MOT, which is also an essential part of our BEC system.

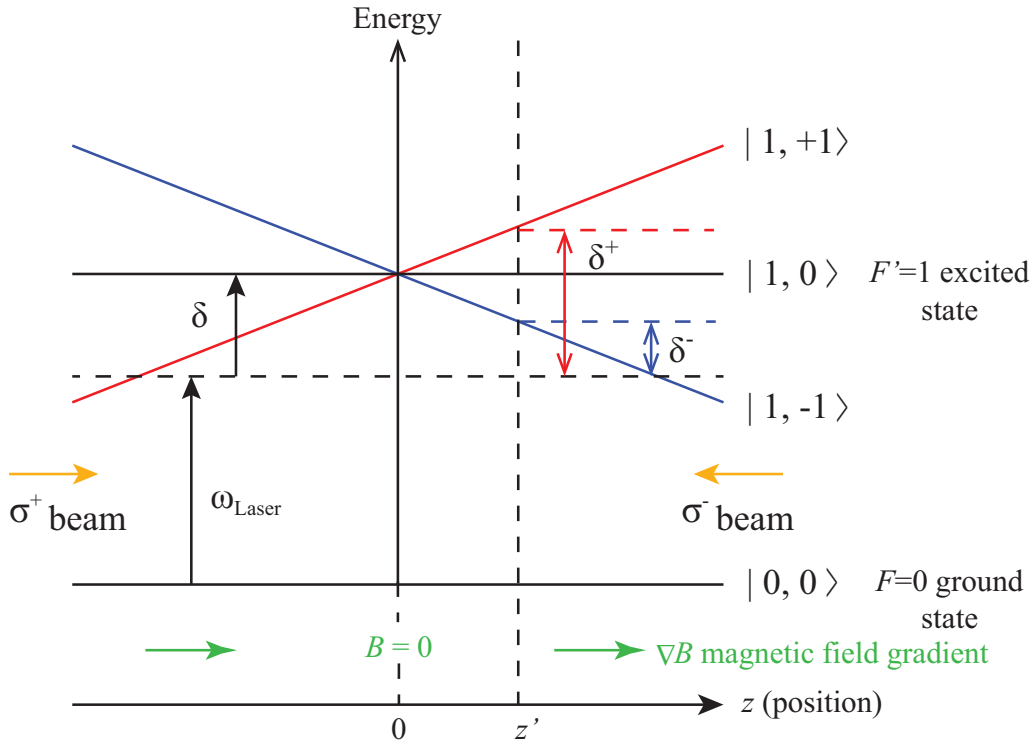

Figure 2.1: Illustration of a MOT along one dimension. Because of the Zeeman effect and σ^+ to σ^- laser polarization configuration, atoms are driven to the center of the trap.

Figure 2.1 shows the basic principle of a MOT in one dimension (1D). For simplicity, we consider an atomic transition from $F = 0 \rightarrow F' = 1$ in the presence of a magnetic quadrupole field where $B = B(z) = Az$. Here A is the magnetic field gradient. The excited state would split into three sub-levels due to the Zeeman effect, which are $M_e = -1$ ($|1, -1\rangle$), $M_e = 0$ ($|1, 0\rangle$), and $M_e = +1$ ($|1, +1\rangle$) states. Two red-detuned ($\delta < 0$) laser beams with opposite circular polarizations (σ^+ and σ^-)

counter propagate to each other. For example, when an atom is at position $z = z^{'}$ in Fig. 2.1, its $M_e = -1$ state is closer to the resonance with the σ^- laser beam traveling from right to left, which means that more photons are absorbed from this beam. As a result, atoms are driven toward the center of the trap. On the other side, since $M_e = +1$ state is closer to the resonance with the σ^+ beam, similarly, atoms are again pushed to the center of the trap. With three pairs of lase beams counter propagating in three orthogonal directions, a 3D MOT can be achieved.

After taking the magnetic field effect into account, we can express the total force acting on an atom in a MOT as follows,

$$\vec{F}_{MOT} = \vec{F}_+ + \vec{F}_- = \frac{\hbar\vec{k}\Gamma}{2}\frac{s_0}{1+s_0+(\frac{\delta-kv+\mu^{'}B/\hbar}{\Gamma/2})^2} - \frac{\hbar\vec{k}\Gamma}{2}\frac{s_0}{1+s_0+(\frac{\delta+kv-\mu^{'}B/\hbar}{\Gamma/2})^2}. \quad (2.7)$$

Here $\mu^{'} = (g_e M_e - g_g M_g)\mu_B$ is the effective magnetic moment, g is the Landé g-factor, and μ_B is the Bohr magneton. After expanding Eq. (2.7) and solving for small Doppler and Zeeman shifts, we can obtain a both velocity and position dependent force similar to a damped harmonic oscillator

$$\vec{F}_{MOT}(v, z) = -\alpha\vec{v} - \beta\vec{z}, \quad (2.8)$$

where α and β are two damping coefficients.

2.4 Optical dipole trap (ODT)

An Optical dipole trap (ODT) is a powerful tool to realize BECs. Compared to magnetic traps in which only atoms at weak-field-seeking states can be confined, an ODT can simultaneously trap all spin components, and thus can be applied to a wider range of atomic species. The potential of an ODT is caused by AC Stark shift and can be expressed by [83]

$$U(\mathbf{r}) = -\frac{3\pi c^2}{2\omega_a^3}\left(\frac{\Gamma}{\omega_a - \omega_L} + \frac{\Gamma}{\omega_a + \omega_L}\right) I(\mathbf{r}), \quad (2.9)$$

and the scattering rate that induces heating can be described as

$$\Gamma_{sc}(\mathbf{r}) = \frac{3\pi c^2}{2\hbar\omega_a^3}\left(\frac{\omega_L}{\omega_a}\right)^3\left(\frac{\Gamma}{\omega_a-\omega_L}+\frac{\Gamma}{\omega_a+\omega_L}\right)^2 I(\mathbf{r}). \tag{2.10}$$

Here ω_a is the atomic resonance, ω_L is the frequency of the laser beam, Γ is the natural linewidth ($2\pi \times 9.8$ MHz for sodium atoms), and $I(\mathrm{r})$ is the laser beam intensity. We define $\Delta = \omega_L - \omega_a$ as the laser frequency detuning, and assume $|\Delta| \ll \omega_a$ if ω_L is tuned close to the resonance ω_a. By applying the rotating-wave approximation [84] and assuming $\omega_L/\omega_a \approx 1$, Eq. (2.9) and Eq. (2.10) can be further simplified as [83]

$$U(\mathbf{r}) = \frac{3\pi c^2}{2\omega_a^3}\frac{\Gamma}{\Delta}I(\mathbf{r}), \tag{2.11}$$

$$\Gamma_{sc}(\mathbf{r}) = \frac{3\pi c^2}{2\hbar\omega_a^3}\left(\frac{\Gamma}{\Delta}\right)^2 I(\mathbf{r}). \tag{2.12}$$

These two expressions clearly show two important points for optical dipole traps. First, the sign of the detuning determines the interaction induced by the trap. For a red-detuned ($\Delta < 0$) trap, the trap potential is negative so that atoms will be attracted into the trap's potential minimum. On the other hand, a blue-detuned ($\Delta < 0$) trap generates a positive energy shift, therefore atoms will be repelled from the trap. The second point is that the potential depth scales as I/Δ while the scattering rate scales with I/Δ^2. A higher laser beam intensity or a smaller detuning can provide a tighter confinement for atoms according to Eq. (2.11). However, since the scattering rate Γ_{sc} would increase faster if we decrease Δ than increasing the intensity I. As a result, in order to reduce the scattering rate to minimize the heating, it is useful to apply a laser beam with a large detuning combined with a high intensity for an ODT.

A red-detuned and tightly-focused Gaussian laser beam can generate a simple ODT. The radial direction of the beam offers the tight confinement while its axial direction has the weaker confinement. The intensity profile of a focused Gaussian

beam with a total power P can be expressed by

$$I(r,z) = \frac{2P}{\pi w^2(z)} \exp\left(\frac{-2r^2}{w^2(z)}\right), \tag{2.13}$$

where r represents the radial coordinate. $w(z)$ is the $1/e^2$ beam radius along the axial direction (z axis), which is given by

$$w(z) = w(0)\sqrt{1 + \left(\frac{z}{z_R}\right)^2}. \tag{2.14}$$

Here w_0 is known as the beam waist and $z_R = \pi w_0^2/\lambda$ is the Rayleigh length where the beam radius increases to $\sqrt{2}w_0$.

The trap depth is defined as the $U = |U(r = z = 0)|$. If U is much larger than the thermal energy of the atomic cloud, the optical dipole potential can be approximated with a cylindrical harmonic oscillator by expanding the intensity profile to the first order, which is expressed by

$$U(\mathbf{r}) \approx -U\left[1 - 2\left(\frac{r}{w_0}\right)^2 - \left(\frac{z}{z_R}\right)^2\right], \tag{2.15}$$

where the corresponding trap depth U is

$$U = \frac{3\pi c^2}{2\omega_a^3}\left(\frac{\Gamma}{\omega_a - \omega_L} + \frac{\Gamma}{\omega_a + \omega_L}\right) I_0 > 0. \tag{2.16}$$

I_0 is the peak intensity at the center of the trap, which is given by $I_0 = 2P/(\pi w_0^2)$. Then both the radial and axial trap frequencies can be derived as

$$\omega_r = \sqrt{\frac{4U}{m w_0^2}}, \tag{2.17}$$

$$\omega_z = \sqrt{\frac{2U}{m z_R^2}}, \tag{2.18}$$

where m is the mass of the atom.

By using two orthogonally crossed laser beams, we can create an ODT with tight confinements in all dimensions. The resultant potential can be obtained by summing two individual trap potential given by Eq. (2.9) together, which is $U_{\mathrm{CB}}(\mathbf{r}) = U_1(\mathbf{r}) +$

$U_2(\mathbf{r})$. Note that we ignore the effect such as the influence of the gravity here. In our case, our first ODT beam (input beam) is along the x axis while the second beam (return beam) travels along the y axis. Thus we can express the trap frequencies in all three directions as follows

$$\omega_x = \sqrt{\frac{4U_2}{mw_2^2}}, \tag{2.19}$$

$$\omega_y = \sqrt{\frac{4U_1}{mw_1^2}}, \tag{2.20}$$

$$\omega_z = \sqrt{\frac{4U_2}{mw_2^2} + \frac{4U_1}{mw_1^2}}. \tag{2.21}$$

The depth of the crossed ODTs can also be described by $U_{\mathrm{CB}} = U_1 + U_2$, where U_1 and U_2 are individual trap depths derived from Eq. (2.16). If two laser beams have the same geometrical parameters and are set at the same power, one can find that $U_{\mathrm{CB}} = 2U$ (twice of the single beam) and the aspect ratio $\omega_z/\omega_{x,y}$ would be $\sqrt{2}$.

2.5 Evaporative cooling

Evaporative cooling is the last step for achieving the quantum degeneracy in most BEC experiments. Similar to cooling a cup of coffee in our daily life, evaporation allows atoms with the highest energy to leave the trap. Because of the Maxwell-Boltzmann distribution, atoms at the tail of the thermal distribution will have energy much higher than their average energy. With those atoms removed from the trap, the energy of the atomic cloud is thus reduced. The temperature of the atomic system is also decreased after the rethermalization of the remaining atoms via elastic collisions. One primary requirement for the evaporative cooling is that the thermalization time should be short enough compared to the lifetime of the system. Because the lifetime is limited by inelastic collisions while the thermalization time relies on elastic collisions, the ratio between these two plays an important role in the evaporative cooling. I will explain this in details in Chapter 5.

Harald Hess originally proposed the idea of the evaporative cooling and used it to capture the hydrogen atoms in magnetic traps [85, 86, 87]. Evaporative cooling in an ODT was first achieved in 1998 [88]. The main idea for evaporation in an ODT is that the trap depth is lowered, which is simply done by lowering down the power of the ODT laser beams [88]. Therefore, atoms with high energy cannot stay in the trap and should be evaporated. After one continuously decreases the laser beam power, the atomic density increases, the temperature of the system is reduced, and thus the phase space density is greatly increased, which finally leads to the quantum degeneracy.

In the evaporative cooling process, the total number of atoms, the collision rates, and the phase space density are important parameters to characterize the cooling efficiency. A simple model based on scaling laws is widely used to describe the relation between the optical trap depth U and these parameters [89, 90]. Based on this model, a detailed explanation of our evaporative cooling process is illustrated in Chapter 5.

CHAPTER 3

The vacuum system

A good vacuum system plays a crucial role in generating BECs. Since the background gas pressure can affect the lifetime of trapped atoms, we need to minimize collisions between background gas atoms and trapped atoms by keeping the pressure of the vacuum system as low as possible. Thus an ultra-high vacuum (UHV) system is necessary for preventing large atom number loss and prolonging the lifetime of trapped atoms to a few seconds. In this chapter, I first elaborate the layout of our UHV vacuum system with a pressure in the 10^{-12} Torr range, its designs, and useful installation procedures including a procedure for baking the system. Then, our standard sodium metal change procedure as well as the procedure for maintaining a good vacuum system are described.

3.1 Overview of our vacuum system

Our novel vacuum system are designed to satisfy the following two important requirements. First, the atomic flux arriving at the main chamber must be large enough and the atom loading rate must be sufficiently quick. So the total length of the system cannot be too long. Second, the pressure inside the main chamber must be low enough to create a BEC, which indicates the main chamber should be separated from other high vacuum pressure areas of the apparatus.

Our final vacuum system design is divided into three major sections, which are the sodium oven chamber, the intermediate chamber, and the main chamber, as shown in Fig. 3.1. The sodium oven chamber is where the atomic source locates,

and is heated up to a high temperature to provide continuous and stable atomic flux. The intermediate chamber is separated from other chambers by two differential pump tubes, which enable us to pump down the pressure by almost two orders of magnitude. The main chamber, where BECs are created and new physics starts, sits at the end of the Zeeman slower tubing. The final vacuum pressure inside our main chamber is $\sim 5 \times 10^{-12}$ Torr. In order to keep the pressure low in our vacuum system, we use three ion pumps to daily pump the system. Two gate valves are installed before and after the intermediate chamber and always leave at the closed position when we are not running the experiment.

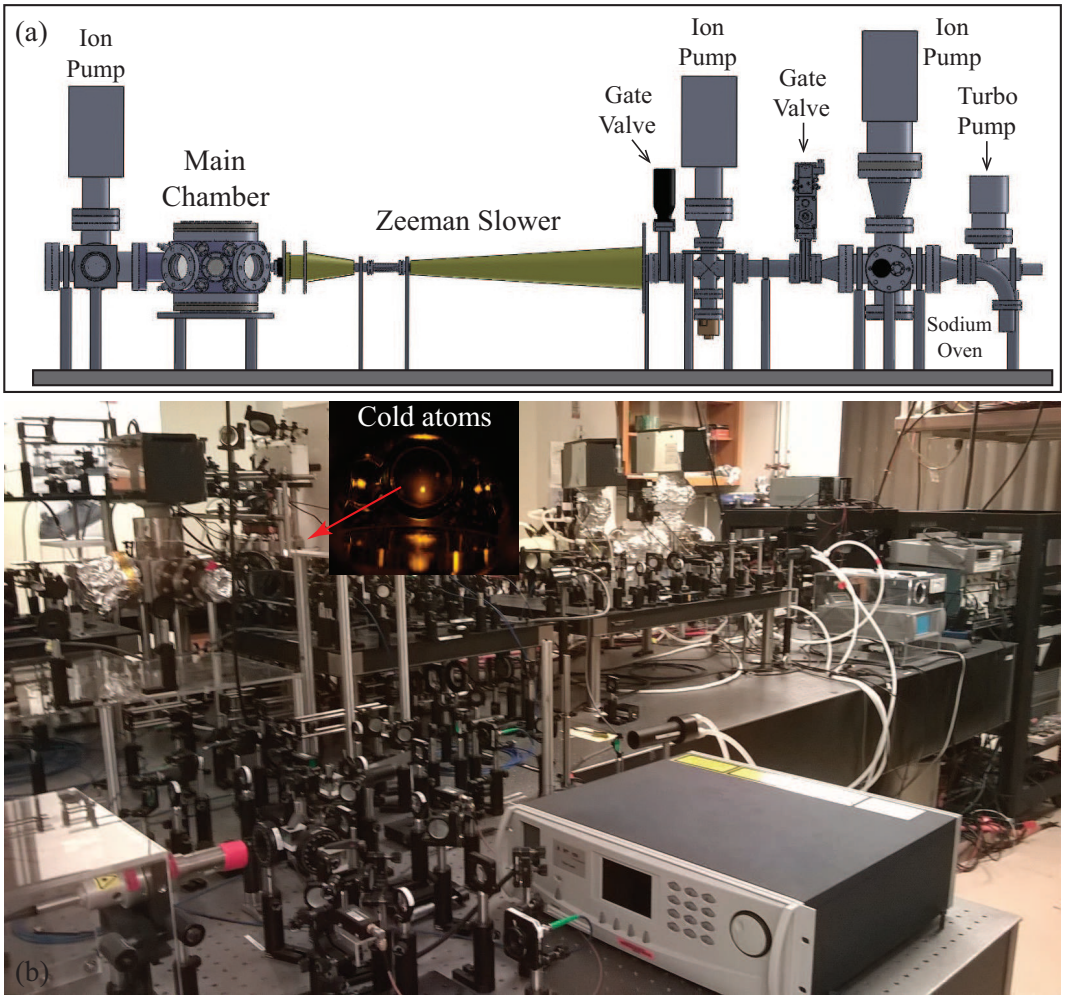

Figure 3.1: (a) Schematic of our experimental setup. (b) Actual apparatus in our lab.

3.2 The sodium oven chamber

The first part of our vacuum system is the sodium oven chamber, which contains the sodium oven, a 6-way cross attached with a 75 liter/second ion pump, and a 4.5" 4-way cross with a turbo pump, as shown in Fig. 3.2. The sodium oven is made by a half nipple and a 90° elbow, where 25 g solid sodium metal is heated up by band heaters to 260 °C, 270 °C, and 310 °C, respectively. Note that the temperature at the half nipple should be set at the lowest temperature, (260 °C), since Na atoms tend to deposit at the cold surface. This is also the reason why we heat up the bottom of the 6-way cross (a 2.75" blank) to 120 °C, which is higher than the sodium melting point 98 °C, and thus can prevent sodium metal clog in the oven chamber. In order to collimate the atomic beam, a double-sided flange with a 6 mm diameter center hole is inserted after the elbow. Then the oven part is attached to the 6-way cross with a conical adapter. A square cooper cold plate with a 9 mm centering hole is placed along the atomic beam path to collect hot scattered atoms. A pneumatic atomic shutter controlled by an air solenoid valve is inserted to shutter the atomic beam during the experiment. A 75 liter/second ion pump and a custom-made baffle are placed on the top of the 6-way cross to pump down the pressure.

We then connect our 4.5" 4-way cross to the remaining port of the 6-way cross. A rough gauge is installed there to daily monitor the vacuum pressure. An angle valve is placed on the opposite side of the rough gauge to seal the system or open the system when sodium change is needed. We then attach a turbo pump and our Ar gas line (see details in section 3.4) to the angle valve. Finally, an AR-coated window is connected to the 4-way cross to view the atomic beam and enable a daily alignment of the slower beam.

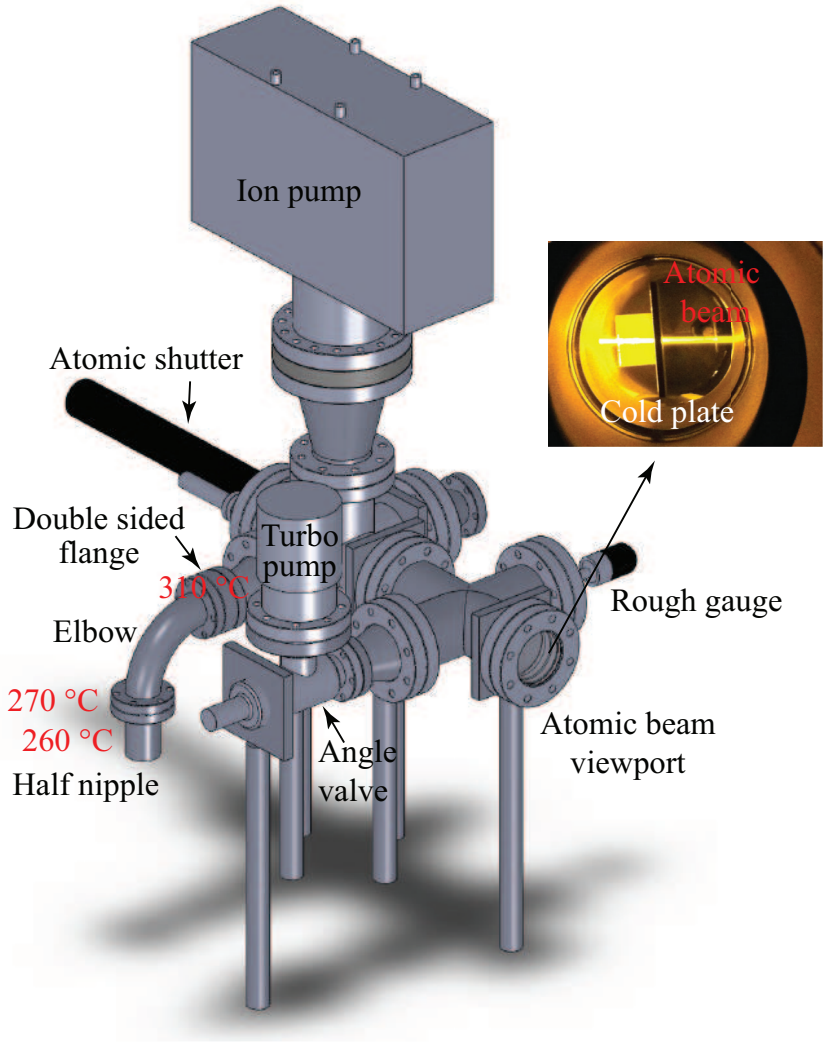

Figure 3.2: Isometric view of the sodium oven chamber.

3.3 UHV chambers

UHV refers to a vacuum pressure lower than $\sim 10^{-9}$ Torr. In our system, the UHV chambers are intermediate chamber and main chamber, as shown in Fig. 3.3. The intermediate chamber is equipped with two differential pumping tubes (DFT) to separate main chamber area from atomic oven chamber that is low pressure area. The DFT is custom made by welding a stainless steel vacuum tube onto the thorough center of a 2.75" double-sided flange, as shown in the inset of Fig. 3.3. The two

DPTs have different parameters: the first DPT is made with a 5" long and 0.25" OD stainless steel vacuum tubing, while the second DPT has a 2.5" long and 0.375" OD vacuum tubing. With the combination of these two DFTs and a 55 liter/second ion pump, we are able to achieve a pressure ratio of ∼500 between the intermediate chamber and the main chamber. Two gate valves are used before the main chamber for preventing potential contaminations/leaks when the experiment is not running or during sodium metal changes. An ion gauge that can measure up to 10^{-13} Torr is located at the bottom of the 2.75" six way cross to monitor the vacuum pressure.

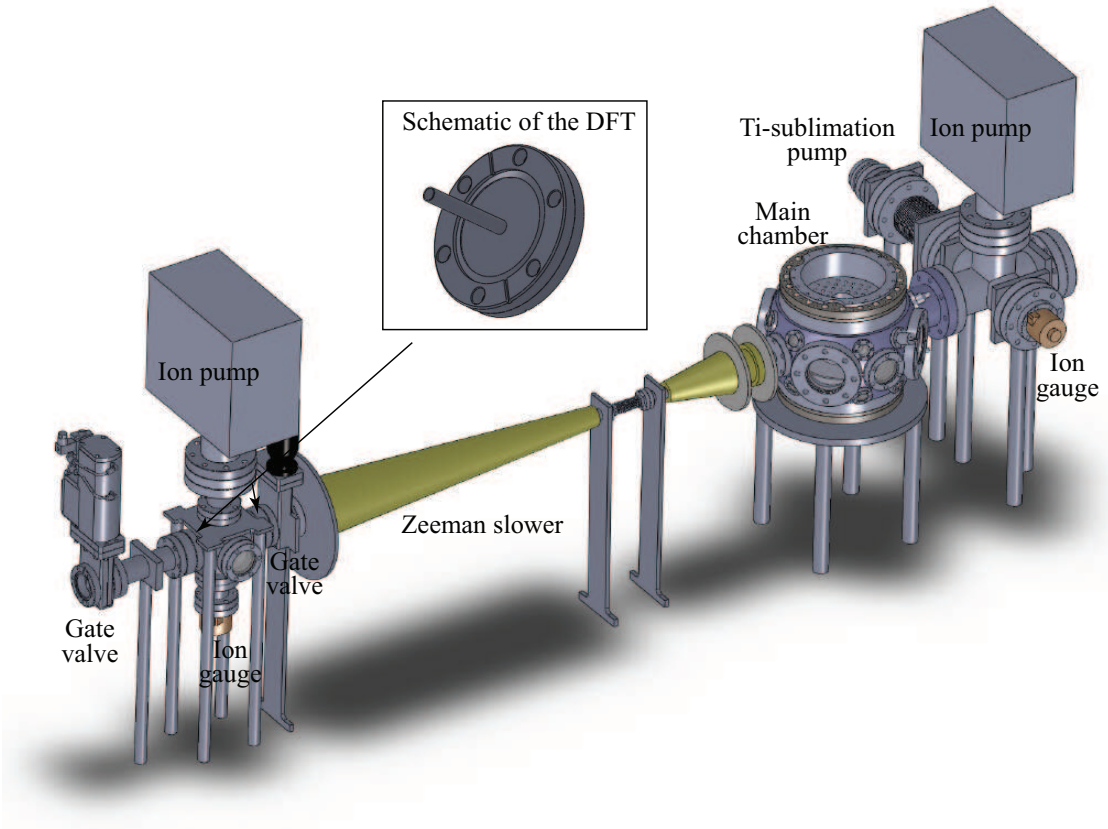

Figure 3.3: Isometric view of the intermediate chamber and the main chamber. Inset: schematic of the differential pumping tube (DFT).

Right after the intermediate chamber is the Zeeman slower, which slows sodium atoms down. The main chamber where BEC occurs is at the end of the Zeeman slower. It is equipped with 7 pairs of AR-coated quartz viewports (whose ODs are 1.33, 2.75,

4.5, and 6 inches) along different directions, which provides optical accesses for our MOT, ODT, and optical lattice setups. A titanium sublimation pump is located next to the main chamber, for further improving the pressure in the main chamber. At the end of the 5-way cross is an viewport for the slower beam. This viewport is kept at 70 °C to eliminate the sodium deposition on the viewport surface.

3.4 Procedures for cleaning, baking, and installing vacuum parts

In order to reach the desired pressure as quickly as possible, the vacuum system must be installed with extra care. Thorough cleaning all vacuum parts is the first necessary step. Typical contaminants in the vacuum system include: 1) oil and grease left on the vacuum components, bolts, and gaskets; 2) small particles and dust; 3) condensed vapors such as water vapor absorbed on the walls of the vacuum system and air inside the vacuum chambers. To eliminate the major contaminants on the surface of the vacuum parts, we develop a 4-step cleaning procedure to ensure our system is grease and dust free.

- Ultrasonically clean metal vacuum parts in a solution consisting of 50% simple green solution (degreaser) and 50% distilled water for one hour at a high temperature of around 70 degrees of Celsius.

- Rinse the vacuum parts with distilled water and ultrasonically clean them in distilled water for one hour at a high temperature of around 70 degrees of Celsius.

- Rinse the vacuum parts with Acetone (HPLC grade) and ultrasonically clean them in Acetone for 30 minutes at the room temperature.

- Rinse the vacuum parts with Methanol (HPLC grade) and ultrasonically clean them in Methanol for 30 minutes at the room temperature.

It is important to note that all fragile vacuum parts, such as viewports, gate valves, ion gauges, and vacuum pumps, can NOT be ultrasonically cleaned. Also Acetone can NOT be used to clean any vacuum part consisting of rubber components.

All the metal vacuum parts are then wrapped with aluminum foils for the preliminary air bake-out. The air bake-out serves as an essential procedure before the UHV system installation, which can significantly increase the desorption and diffusion rates, and thus greatly shortens the final vacuum pumping-down time. In our system, we baked clean metal vacuum parts in a custom-made oven covered with fiber glass insulation tapes and aluminum foils. The temperature inside the oven was raised to 320 °C (the maximum baking temperature for most of our metal vacuum parts is 450 °C) with the temperature gradient of 50 °C/hr and kept at this value for a week. After the air bake-out, the color of metal surfaces would change from silver to shiny gold. If the color tends to be violet, it indicates over baking and the baking temperature should be lowed down.

The assembling process for the vacuum system is straightforward but extra care must be taken. First, clean grease-free and powder-free gloves must be worn during the whole assembling, and one should change the gloves frequently. All the gaskets, bolts, and nuts used in our vacuum system are silver-plated to avoid using anti-seize grease. During the installation process, gaskets should be aligned well into the flanges, and all the bolts were hand tighten first and then fully tighten by a wrench one by one in a diagonal direction until little gap can be seen between the flanges. Extra attention should be paid when one tightening viewports since they may break easily if force applied on them is not uniform.

After the system was fully assembled, we started to pump down the pressure. However, the final pressure was limited in the 10^{-11} Torr range after several days and decreased very slowly, which was not good enough for generating BECs. This may be due to the fact that large amounts of air was left in the system and other residual gases

could be trapped in the metal vacuum parts, which limited desorption and diffusion rates, and thus made the pumping process hard. So it was necessary to apply a final system bake-out to increase the pumping rate and improve the final vacuum pressure. We applied band heaters and heating tapes to the system and raised the temperature to 150 °C slowly, and baked the system for several days. All the three ion pumps were turned off first for nearly two days at the beginning of the baking to avoid damaging the pumps. During the baking process, we also degassed ion gauges for about one hour to pumped dirts out. The Ti-sublimation pump was operated as well for one hour to force the hydrogen gas escaping from the metals, which improved the vacuum pressure inside the main chamber (Note that the Ti-sublimation pump can be turned on only when the pressure is less than 10^{-8} Torr). We began to switch off the heaters and cooled down our system after the pressure inside the main chamber stayed stable at 2×10^{-10} Torr for a few days. After cooling the apparatus down to the room temperature and using the Ti-sublimation pump for 10 more minutes at the end, our vacuum system finally reached a UHV of $< 5 \times 10^{-12}$ Torr, which means that the lifetime of the trapped atoms could be as long as tens of seconds. Fig. 3.4 shows the change of vacuum pressure before, during, and after the baking.

3.5 Sodium change

An ampoule of 25 g sodium metal can be used for about half an year in our lab before we have to break the vacuum and do a sodium metal change. The lifetime of the sodium metal is also closely related to the temperature applied to the atomic oven. The higher the temperature is, the more atomic flux would be generated, however, the lifetime of the sodium metal would decrease. In our system, the typical lifetime of a 25 g sodium metal is $\sim$ 800 hours when the oven is set at 260 °C. In order to pump the vacuum pressure from the atmosphere back to the UHV quickly, we have developed a standard sodium change procedure.

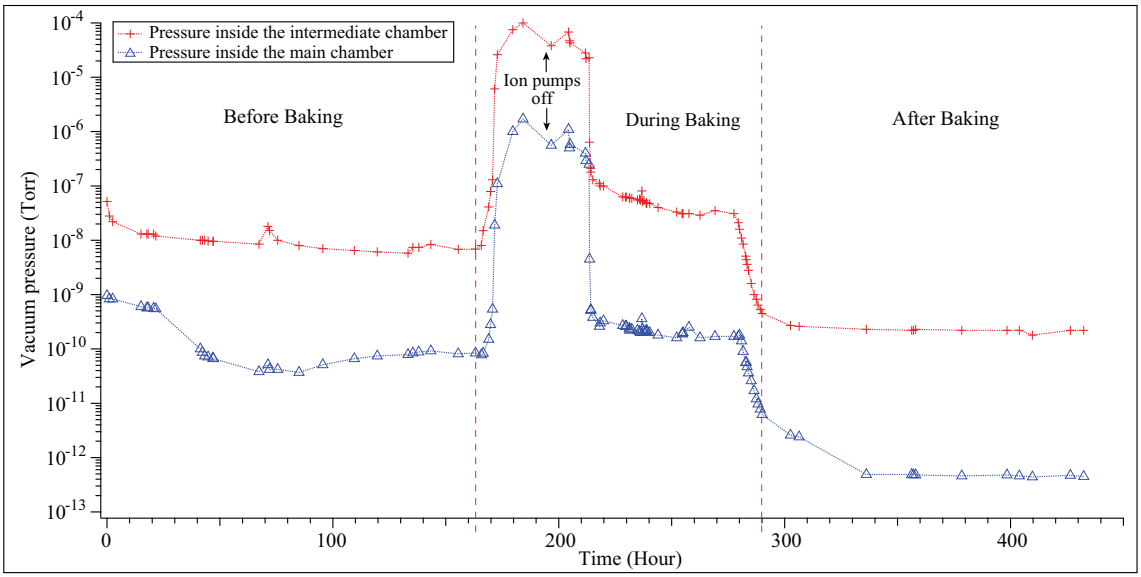

Figure 3.4: Vacuum pressure in two chambers before, during, and after the baking.

Figure. 3.5 shows the setup used during sodium changes, which includes a gas line filled with pure Argon (Ar) gas to vent the system, a roughing ramp, and a Turbo pump. First, before a sodium change, the entire apparatus should be cooled down to the room temperature, the two gate valves should be closed, and the ion pump in the oven chamber should be switched off. Second, we clean all the parts before the all-metal angle valve (i.e., the Ar gas line, the roughing pump, rough valves, connectors, and the Turbo pump) by repeating the following procedure a few times: turn on the roughing pumping and the Turbo pump for 20 minutes or until the reading of the rough gauge stays at its minimum value; turn off the two pumps; and then fill pure Ar gas into the system until the rough gauge reads 1 atm. Third, we turn off the two pumps, open the rough and angle valves in the oven chamber, and vent the oven chamber with pure Ar gas. Fourth, we leave the Ar gas flowing in the oven chamber, while breaking the vacuum of the chamber by removing the half nipple of the sodium oven first, then taking the cold plate and atomic shutter out and thoroughly cleaning them. To avoid unnecessary contaminations, we seal all openings with either a 4.5" or a 2.75" blank. Fifth, while leaving the Ar gas flowing in the oven chamber, we put

back the cleaned cold plate and atomic shutter, and reload the sodium oven with a new ampoule of 25 g sodium metal as quick as possible to avoid oxidizing the sodium metal. After the sodium metal change, our system can usually get back to the UHV after a 2-day vacuum pumping-down.

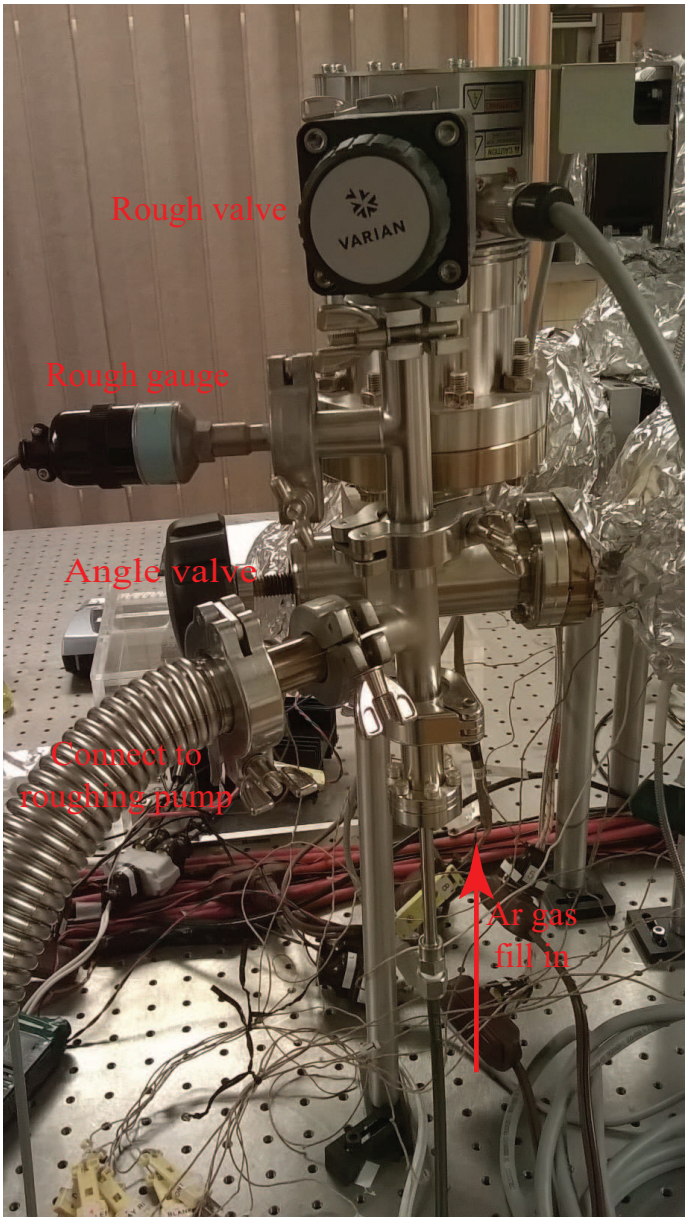

Figure 3.5: Setup for the sodium metal change.

CHAPTER 4

A refrigerator: Experimental setups for laser-cooled atoms

This chapter presents our novel experimental setups for a sodium spinor BEC. Two papers related to these topics were published:

- J. Jiang, L. Zhao, M. Webb, N. Jiang, H. Yang, and Y. Liu, *Simple and efficient all-optical production of spinor condensates*, Phys. Rev. A **88**, 033620 (2013).
- L. Zhao, J. Jiang, Y. Liu, *Optimizing a spin-flip Zeeman slower*, arXiv:1401.7181.

Laser cooling and trapping technique is a powerful tool to create cold atoms. In this chapter, I will explain some necessary experimental setups for achieving sodium BECs, such as optical setups, a spin-flip Zeeman slower, a magneto-optical trap (MOT), and a crossed optical dipole trap (ODT). In our system, hot sodium atoms are first slowed by a spin-flip Zeeman slower, captured in a standard MOT, cooled through a polarization gradient cooling process to 40 μK, loaded and evaporatively cooled in a crossed ODT.

4.1 Optical layout

A stable and efficient optical system is an essential component of a BEC apparatus. In our system, all laser beams except the ODT and optical lattice beams are derived from a Matisse dye laser. This dye laser uses a mixture of 2 g Rhodamine 590 laser dye (Exciton, inc) and 4 Liter Ethylene Glycol, and is pumped by a 10 W laser beam at 532 nm. The typical operating pressure for the dye circulator is set at 15 Bar. The output power of 620 mW at $\lambda = 589.159$ nm from the dye laser is sufficient for our

experiments. In general, fresh laser dye can be used to run experiments continuously for about 21 days. To prevent a long-term frequency drift, we use the saturated absorption spectroscopy technique with a sodium vapor cell to externally lock our laser at 100 MHz below the sodium D_2 line (see details in section 4.4).

All laser beams necessary for the laser cooling and trapping process in our system are shown in Fig. 4.1. The cooling beam is red detuned by δ_{cooling}=20 MHz below the $3^2S_{1/2}|F=2\rangle \rightarrow 3^2P_{3/2}|F'=3\rangle$ transition. This transition is known as a cycling transition. In this transition, atoms are first excited to the $3^2P_{3/2}$ $|F'=3\rangle$ state and then back to the $3^2S_{1/2}|F=2\rangle$ state due to the spontaneous emission. These atoms can be recycled and pumped back to the excited state again for further cooling. However, in fact, some atoms may be pumped to the different excited states and decay to the $3^2S_{1/2}|F=1\rangle$ state, which can not be recycled, and thus accumulate at the $3^2S_{1/2}|F=1\rangle$ state. In order to overcome this problem, a repumping beam, which is 1708 MHz detuned from the cycling transition, is used to pump these atoms back to the $3^2P_{3/2}|F'=2\rangle$ excited state to ensure the atoms can be recycled in the cooling process. Our $F=2$ imaging beam is set at -2 MHz below the $3^2S_{1/2}|F=2\rangle \rightarrow 3^2P_{3/2}|F'=3\rangle$ transition and the slowing beam is red detuned by 542 MHz from the cycling transition.

Figure 4.2 shows the optical layout to generate a number of laser beams at different frequencies for a laser cooling and trapping process in our system. By utilizing a polarizing beam-splitting (PBS) cube and a half-wave ($\lambda/2$) plate, one laser beam is split into two orthogonal paths and the power of each beam can be adjusted by rotating the $\lambda/2$ plate before the PBS. It is worthy to note that PBS1 and PBS2 are used to align all laser beams back to their original positions after a dye change. M1 and M2 are the two mirrors that finely adjust the imaging beams. We use one commercial acousto-optic modulator (AOM) from IntraAction to detune the laser frequency for different optical paths. All the actual center frequencies of the AOMs, labeled in

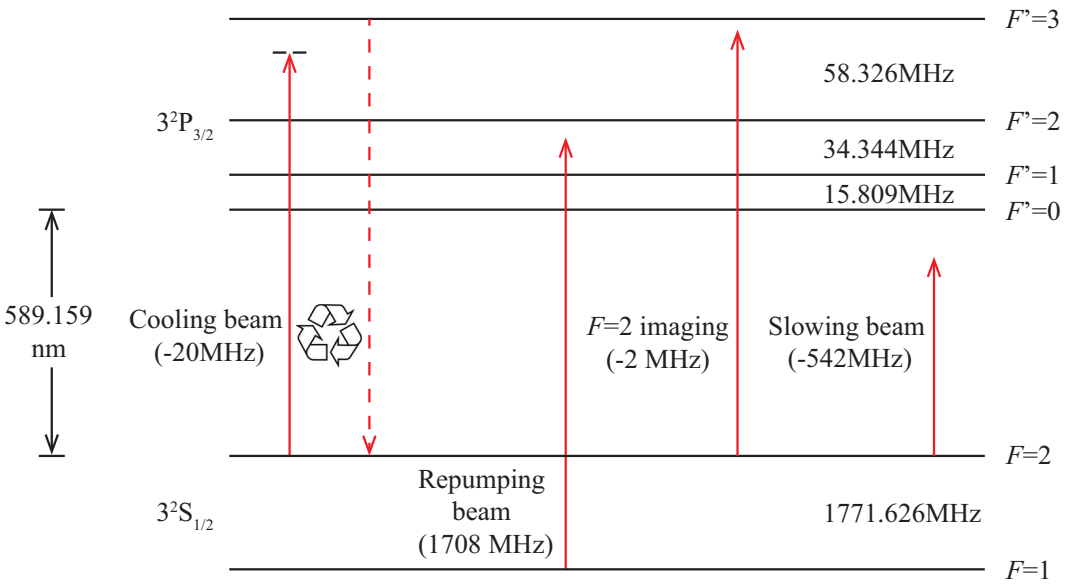

Figure 4.1: Schematic of various laser beams used in laser cooling and trapping sodium atoms.

Fig. 4.2, can be set on front panels or modulated by analog signals controlled with our PC. A double-pass AOM scheme is applied to modulate frequencies or amplitudes of a few laser beams (e.g., the MOT cooling beam) within a wide range in an experimental sequence (see details in the next section). A custom-made EOM from Newfocus is used to apply a 1.7 GHz sideband to the slowing beam, which pumps atoms in the slowing process to the F=2 state. All laser beams with proper frequencies are then delivered to the main chamber with single-mode polarization-maintaining (PM) optical fibers. These PM fibers minimize laser pointing fluctuations as well as purify beams' spatial modes. A special fiber we use in the MOT setup is an optical fiber array made by Evanescent Optics Inc, which has two inputs and six outputs. This fiber array allows a perfect overlapping of the MOT cooling and repumping beams. All the fibers are well aligned with coupling efficiencies above 50% by choosing a proper telescope to match a laser beam with individual fiber's core size. Commercial fiber collimation packages from Thorlabs (e.g., F230FC-A, etc) are also used for each fiber to reduce the difficulty during the alignment and output well defined collimated

beam. A $\lambda/2$ waveplate is applied before each PM fiber to align the polarized laser beam into the slow axis of the fiber. An optical shutter with 3 ms response time (Uniblitz LS series and VMM-D4 controller) is inserted in each optical path in order to quickly extinguish unnecessary laser beams during an experimental sequence. Each element in Fig. 4.2 is automatically controlled by a digital or analog signal generated by NI or Spincore DAQ cards. Figure 4.3 shows our dye laser and optical setup.

4.2 Double-pass AOM

AOMs are widely used in the laser cooling and trapping experiments since they can conveniently detune frequencies of laser beams. When an rf signal with frequency of Ω is sent into the AOM, sound waves at the speed of v_s would be created, and thus the index of refraction of the crystal is modulated at $\Lambda = v_s/\Omega$. At this time, the incoming laser light passes through the "phase grating" like media would lead to interference patterns similar to Bragg diffractions.

In our setup, we mainly use the single-pass and double-pass AOMs to detune the laser frequencies, switch on/off the light, and modulate the laser beam intensity. First, the single-pass AOM can easily detune the laser frequency to a fixed desired value, which is good for some laser beams, such as the imaging beam whose frequency detuning is kept unchanged during an experimental sequence. Normally, the diffraction efficiency is above 80% by using a proper telescope. However, for other laser beams such as the MOT cooling beams, their frequency needs to be changed during one experimental cycle. The frequency change leads to laser beams being misaligned from their corresponding fibers. In order to eliminate this problem, we apply a double-pass AOM scheme to maintain the laser beam pointing as well as provide a large frequency detuning [91].

Figure 4.4 shows a typical scheme for a double-pass AOM. The diffracted beam (+1 order away from the AOM's SMA connector) is retro-reflected by a mirror and passed

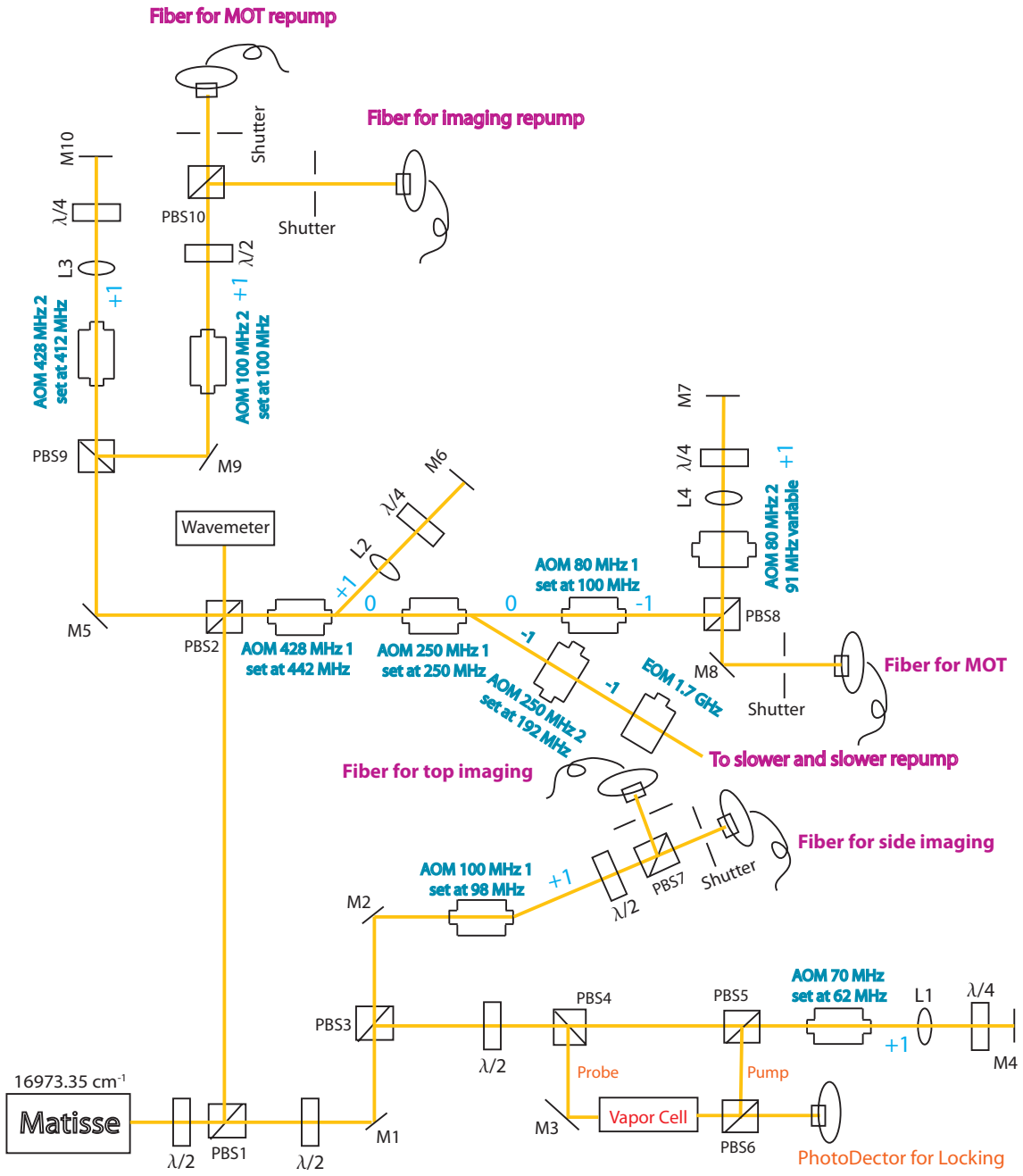

Figure 4.2: Optical layout for generating laser beams of different frequencies. These beams are used to construct a 3D MOT. PBS, M, L, $\lambda/2$, $\lambda/4$ and AOM correspond to a polarizing beamsplitting cube, a mirror, a lens, a half-wave plate, a quarter-wave plate, and an acousto-optic modulator, respectively.

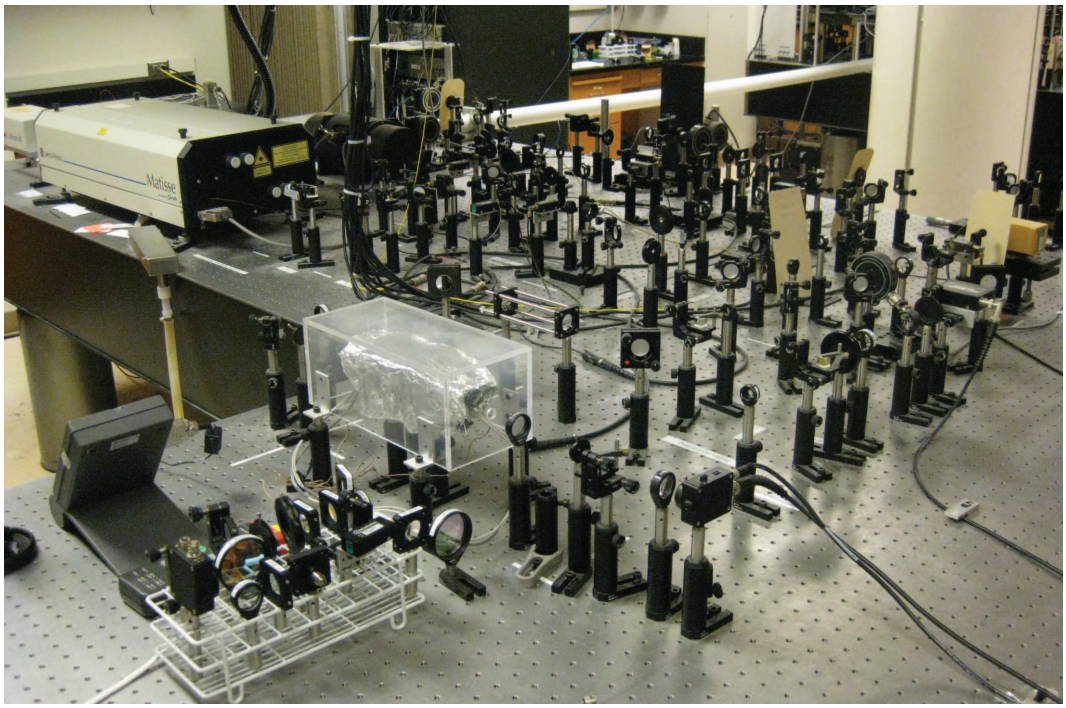

Figure 4.3: A photo to show the dye laser and optical setup in our lab.

through the AOM again, which means that its frequency detuning is also doubled. The second pass beam counter-propagates along with the original zero order beam and can be changed by π in polarization by using a cube and a $\lambda/4$ waveplate. A lens is placed at its focal length after the AOM to ensure that the retro-reflected beam remains the same size when passing back through the AOM, which can maximize the AOM's efficiency. The typical efficiency for a double pass AOM is $\sim$60% in our system. With a double-pass AOM scheme, the final diffracted beam (+2 order) overlaps with the incident beam no matter whether there is a frequency modulation or not, which is important for laser cooling and trapping experiments.

4.3 Polarization of laser beams

To enhance the performance of the system, it is important to set the correct polarization for each different laser beam. First, the linearly-polarized laser beam should pass through the slow axis of the PM fiber. The slow axis alignment is a popular

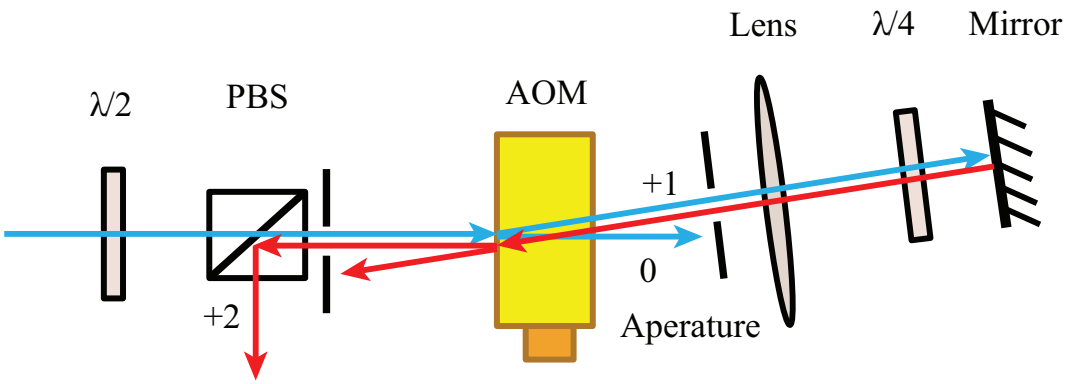

Figure 4.4: Schematic of a double-pass AOM setup.

choice in fiber optics technology nowadays. The better the polarized light is aligned along the slow axis, the longer time the polarization would be maintained. The good position can be found by measuring the distinguish ratio of the fiber output beam. In our system, we put a $\lambda/2$ waveplate and a PBS after the output fiber and used a power-meter to detect the laser beam power after the PBS. By rotating the two $\lambda/2$ waveplates before and after the fiber, we found the maximum distinguished ratio where polarization drifts the least. At this point, the fiber output beam's polarization should stay stable regardless of the change in the room temperature or small external stresses applied on the fiber. In addition, in order to continuously measure the distinguished ratio, we built a motorized rotatable polarizer, which was assembled with a computer fan and a linear polarizer. This polarizer replaced the role of the $\lambda/2$ waveplate after the fiber. With the light signal collected by a photodetector and sent to an oscilloscope, we could easily change the input $\lambda/2$ waveplate to achieve the best distinguished ratio.

Second, the polarization of the six MOT beams and the slowing beam should be either σ^+ or σ^- polarized. Figure 4.5 shows the schematic to set up the σ^+ or σ^- polarized laser beam. The laser beam after the fiber is set to be linearly (horizontally) polarized by using a $\lambda/2$ and a PBS. The first $\lambda/4$ waveplate, acting as an analyzer, is used to transform this beam into the circular polarization, which can be achieved

by rotating the waveplate until the power ratio of the laser beams passing along two orthogonal axes (transmitting axis and absorbing axis) of the final linear polarizer is 1:1. The second $\lambda/4$ waveplate is then inserted into the beam path to determine σ^+ or σ^- polarization. The laser beam would be changed back to linear polarization after the analyzer now. Rotating the second $\lambda/4$, the laser beam is σ^+ (or σ^-) polarized when the power after the linear polarizer is minimum (or maximum). In the end, the analyzer (the first $\lambda/4$) should be removed from the beam path.

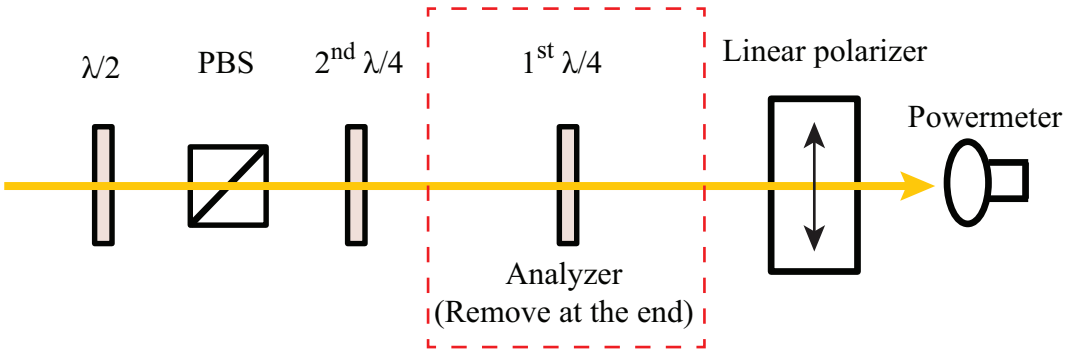

Figure 4.5: Schematic to set up the σ^+ or σ^- polarized laser beam.

4.4 Frequency stabilization

The natural linewidth of ^{23}Na atoms is 9.8 MHz, which requires the linewidth of our dye laser to be much narrower than this value. Although the specified linewidth of our dye laser is $\sim$1 MHz, its center frequency can drift by a significant amount over long time due to room temperature changes or piezo actuator relaxation processes in the reference cell. To compensate this frequency drift, we apply the saturated absorption spectroscopy technique with a sodium vapor cell to externally lock our laser.

Each atom has unique absorption frequencies according to its hyperfine structure, but its related spectral lines are not resolved due to the Doppler broadening. The reason is that the atoms obey Maxwell-Boltzmann temperature distribution of velocities at a given temperature. Thus, some atoms would stay stationary, while others

moving with different velocities. If one laser beam at the atomic resonance ν_0 is used in the system, only those atoms with zero velocity along the laser beam can interact with it. Other atoms with a speed of v_z can only be resonant with the laser beam when its frequency is tuned to $\nu = \nu_0(1 \pm c/v_z)$, which satisfies the Doppler shift condition. Here c is the speed of light. This gives us a Doppler broadened spectrum. In order to eliminate the Doppler broadening, the saturated absorption spectroscopy was developed [92]. In this technology, two laser beams (the pump beam and the probe beam) counter propagate through the vapor cell. When the laser frequency is tuned to one of the two resonances, the pump and the probe beams both compete for the zero velocity class atoms and the absorption of the probe beam is reduced, which creates the transmission peaks in the Doppler-broadened profile. Additionally, crossover peaks occur when the laser is at the half way between the two resonances. The pump beam puts more atoms in resonance with the probe beam. So the pump beam will actually increase the population of the ground state that the probe is resonant with, and the absorption of the probe beam will be enhanced.

Figure 4.6 shows the schematic of our saturated absorption spectroscopy. The intensive pump beam and weak probe beam counter propagate through the sodium vapor cell, and the absorption signal is collected by a photodetector from Thorlabs (PDA36A). In order to lock the laser with this absorption signal, we use a lock-in amplifier (Stanford Research Systems SR810) to produce an error signal. A reference sine wave generated by the lock-in amplifier with a frequency of 20.31 kHz and an amplitude of 0.39 V is used to modulate the frequency of the pump beam AOM. Then this sine wave along with the absorption signal are mixed by the lock-in amplifier to generate an error/dispersion signal, which is digitized with one AI channel by a NI USB6008 DAQ card and processed by the Matisse software. Finally, the Matisse laser controller would feed it back on the reference cell piezo actuator and keep the Matisee laser at the desired atomic resonance frequency. We scanned the power ratio between

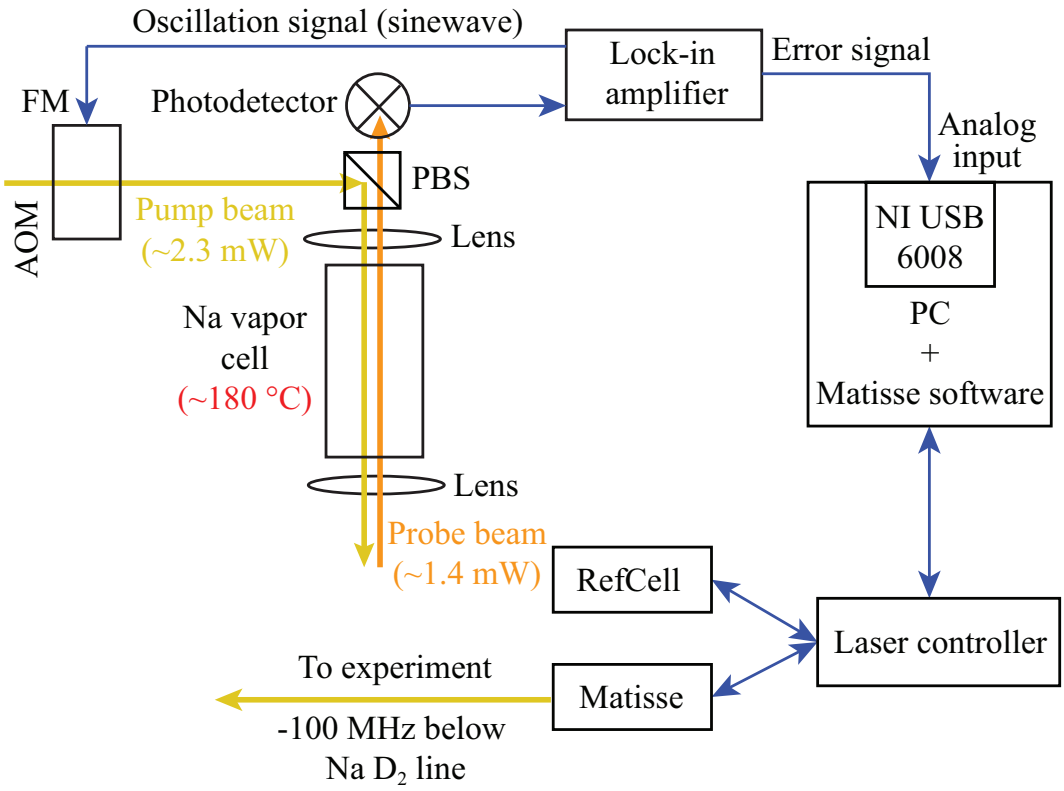

Figure 4.6: Schematic of our saturated absorption spectroscopy.

the pump and probe beams as well as the temperature of the sodium cell. The best power ratio for pump/probe beam is ∼2:1 in our system. In our daily routine, the pump beam power is often set at ∼2.3 mW while the power of the probe beam is ∼1.4 mW. Two long focal lenses are placed in each beam path to shrink down the beam size. The sodium vapor cell is wrapped with fiber glass insulation tapes and aluminum foils, and is heated up to ∼180 °C with two band heaters, as shown in Fig. 4.7. Note that heating must be uniform over the cell, since sodium metals tend to be deposit on cold surfaces. Sodium depositions may block the laser beam paths and result in an unstable lock-in signal. The vapor cell is kept at 140 °C when we do not run experiments. A typical absorption signal collected by the photodetector as well as its dispersion signal recorded in an oscilloscope are shown in Fig. 4.8. Our laser is locked 100 MHz below the F=2 to F'=3 transition with a typical RMS frequency deviation of ∼60 KHz.

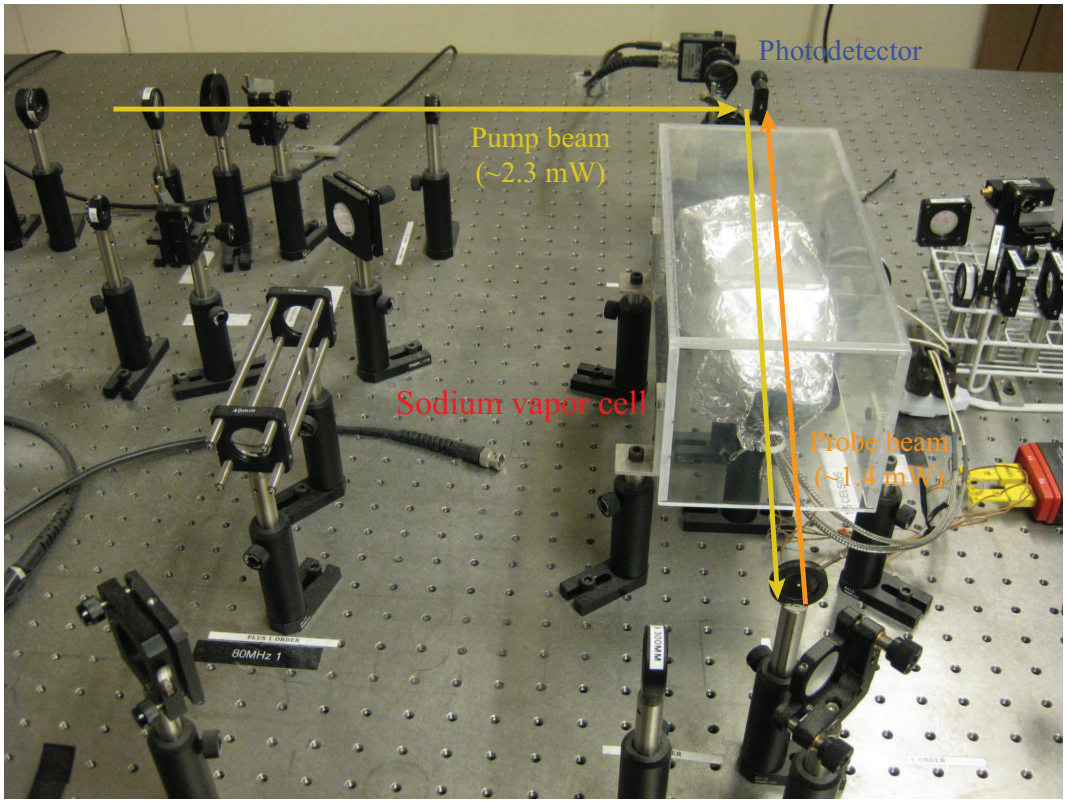

Figure 4.7: Our sodium vapor cell.

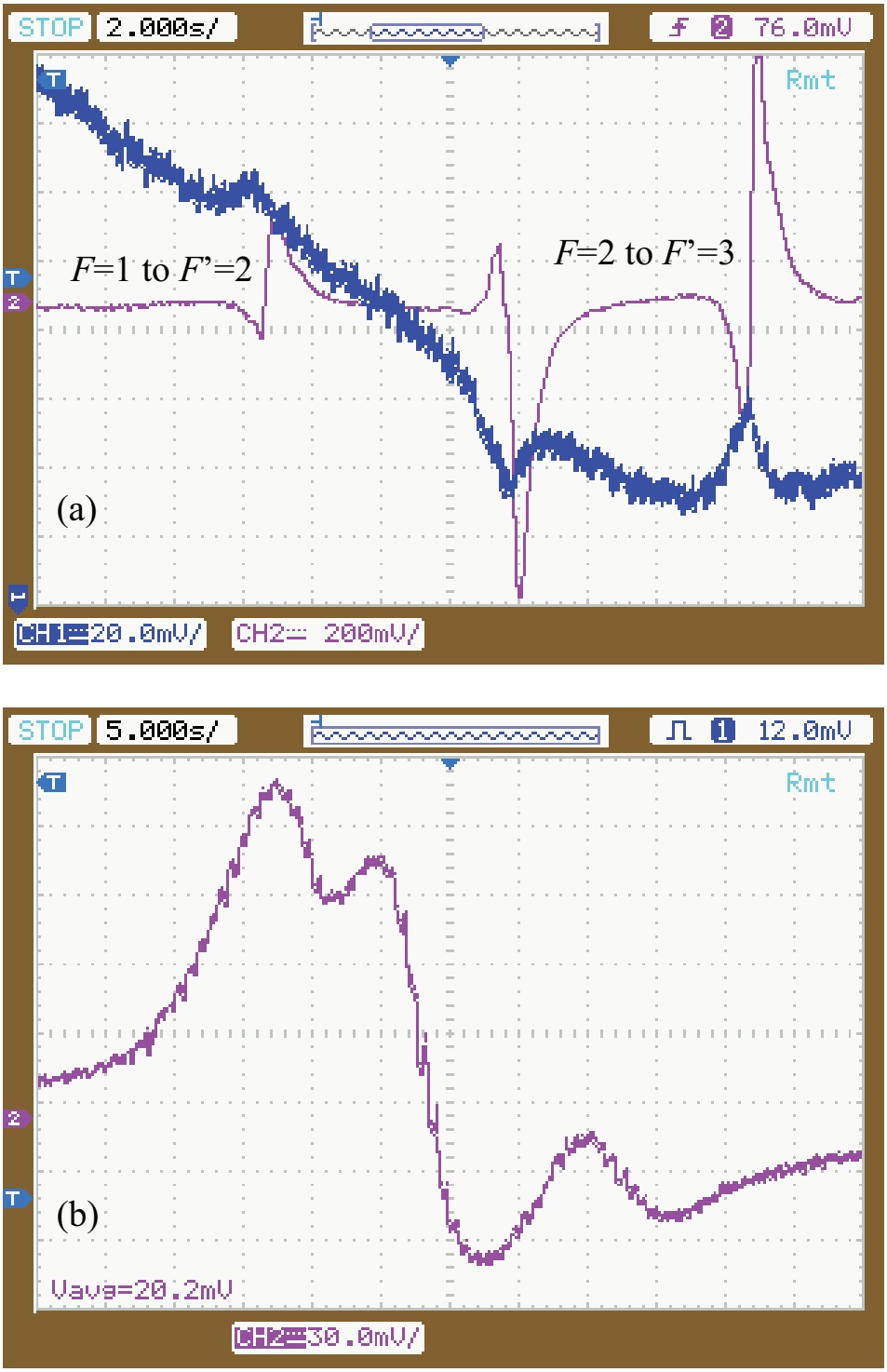

Figure 4.8: (a). Measured absorption and dispersion Doppler free spectral features. The absorption signal from a photodiode (purple line), and the dispersion signal from the lock-in amplifier (blue line) are recorded on a digital oscilloscope. (b). An expanded view of our F=2 to F'=3 peak.

4.5 Spin flip Zeeman slower

A MOT can only capture atoms whose velocities are smaller than v_c, its maximum capture velocity, which is $v_c = 55$ m/s in our system. To improve the MOT capture efficiency, a number of slowers have been invented to significantly slow hot atoms down before they overlap with the MOT [10, 74, 93, 94, 95, 96, 97]. In a slower, atoms and a resonant laser beam of frequency ω counter-propagate along the x axis. The longitudinal velocity and Doppler shift of these atoms decrease after they absorb resonant photons. These slowed atoms are thus no longer resonant with the laser beam and cannot be further slowed down. To continuously reduce the atoms' velocity along the beam path, one can vary ω accordingly as with the frequency chirp method [98] or by using broadband lasers [99]. Another convenient method is to keep ω unchanged, while compensating differences in the Doppler shift with a spatially varying magnetic field generated by a Zeeman slower [10, 74, 93, 94, 95, 96, 97].

When the alkali atoms pass through the Zeeman slower, only the atoms whose velocities satisfy $kv(x) + 2\pi\delta + \mu B(x)/\hbar = 0$ are on resonance with the slowing laser beam, where μ is the magnetic moment, k is the wavevector of the laser beam, δ is the frequency detuning of the laser beam from atomic resonance, and $\hbar$ is the reduced Planck's constant. In other words, only the atoms with velocity $v(x) = -[2\pi\delta + \mu B(x)/\hbar]/k$ can be slowed by the slower [94]. The corresponding acceleration a_s can be expressed as

$$\frac{dB(x)}{dx} = -a_s \frac{\hbar k}{\mu v} \ , \tag{4.1}$$

where $a_s = \eta a_{\max}$ is the actual acceleration provided by the slower, $a_{\max} = \frac{\hbar k \Gamma}{2M}$ is the maximum achievable acceleration, Γ is the natural linewidth of the atomic transition, M is the atom mass, and η is a safe factor to account for magnetic field imperfections in a given slower and the finite intensity of the laser beam.

In our system we choose a spin-flip Zeeman slower, which consists of three different

sections along the x axis (i.e., a decreasing field coil, a spin-flip section, and an increasing field coil), as shown in Fig. 4.9. The first section produces a magnetic field with decreasing magnetic field strength B. Because B is very large (~ 650 Gauss) at the entrance of the slower, ω only needs to be red-detuned by δ of a few hundred MHz from the D_2 line of ^{23}Na atoms. This frequency detuning is easily achieved with an AOM, but is still large enough to avoid perturbing MOT laser beams. The spin-flip section contains no coils as to maintain $B = 0$. The increasing field coil creates a magnetic field with increasing B but in the opposite direction to the decreasing field section. Because the magnetic field quickly dies off outside the slower, the slower can be placed close to the MOT, which results in more atoms being captured.

Our Zeeman slower is wound on a stainless steel tube that measures 22.5 mm inner diameter and 25.5 mm outer diameter, which is similar to the design of Ref. [97]. Compared to the single-layer Zeeman slower with variable pitch coils [100], the advantage of this design is that it provides enormous flexibilities to optimize magnetic fields with large enough B for slowing atoms with high initial velocities (e.g., sodium and lithium atoms). Figure 4.9 shows the schematic of the Zeeman slower and the real setup in our lab. The slower coil we use is a Kapton tape coated hallow copper wire with 0.3175 cm$\times$0.323 cm outer dimension and 0.155 cm inner dimension. The first layer of our decreasing field coil has 188 turns and its length is 0.60 m. Its second layer is 0.57 m long and wrapped on the surface of the first layer. Similarly, the following layers are wrapped on the surface of its corresponding previous layer. The increasing field coil is constructed in a similar way and is divided into two parts. The two parts both have five layers, with the electric current flowing in the opposite direction through the top two layers of the second part. These two layers are compensation field coils to minimize the residual magnetic field strength generated by the slower in the main chamber. The spin-flip section is simply a bellow, which allows atoms to be fully re-polarized and damps out mechanical vibrations generated by vacuum pumps.

To precisely adjust magnetic field strength inside the slower, the total 22 layers are divided into six groups, and different layers in each group are connected in series and controlled by one DC power supply with our fast feedback circuit. Since more than 20 A current would flow through the slower, we connect coils in each different section with a water cooling system to lower down the temperature. The water cooling system consists of a heater exchanger, a boost pump with the pressure of 150 psi, and two manifolds to split chilling water into tubes for different devices such as Zeeman slower coils, MOT coils, ODT beam dampers, etc.

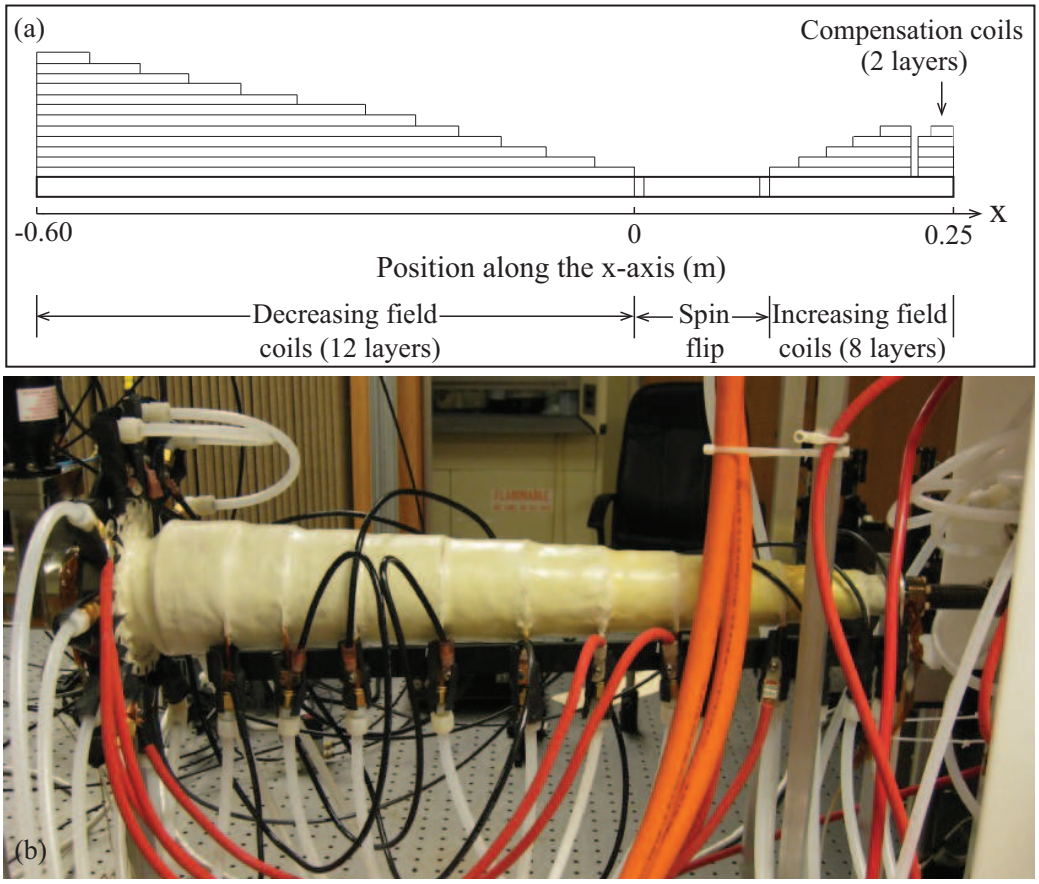

Figure 4.9: (a) Schematic of the spin-flip Zeeman slower setup. (b) The actual Zeeman slower setup in our lab.

In order to improve the efficiency of a slower, different parameters such as the slowing laser beam's intensity and frequency detuning, current flow in each magnetic

coil, and the length of each section in the slower can be tuned for optimization. The detailed optimization procedure can be found in Ref. [101] or my labmate Lichao's dissertation.

4.6 3D MOT

4.6.1 MOT setup

After sodium atoms being slowed down with our Zeeman slower, we use a Magneto-optical trap (MOT) to further cool down the atoms. In our experimental setup, the 3D MOT is constructed with six cooling beams in three orthogonal directions and a pair of 24-turn anti-Helmholtz coils, as shown in Fig. 4.10(a). Each MOT cooling beam is detuned by $\delta_{\text{cooling}} = -20$ MHz from the cycling transition, has a power of 4.6 mW, and combines with one 2.2 mW MOT repumping beam in a same single-mode fiber. Every MOT repumping beam is detuned by $\delta_{\text{repump}} = -5$ MHz from the $|\text{F} = 1\rangle$ to $|\text{F}' = 2\rangle$ transition. Since we have a two in six out fiber array (as mentioned in section 4.1), overlapping for the cooling and repumping beams would be perfect. One additional advantage of this fiber array is that it allows us to individual control each different MOT beam easily. As shown in Fig. 4.10(b), every MOT beam is expanded to 1.2" in diameter by using a cage system from Thorlabs, which is a less-costly replacement of a translation stage. A $\lambda/4$ waveplate is placed along each beam path to make the polarization either σ^+ or σ^-.

A pair of anti-Helmholtz coils made with hallow copper coils (the same coil used for our Zeeman slower) is located inside the 8" top and bottom viewports, which provides the necessary magnetic field gradient ($\sim$480 mG/cm/A) to the MOT trap. The coils have total 6 layers with 4 turns in each layer and the average diameter for each coil is about 4". The MOT coils are also applied to generate a small magnetic field gradient during evaporative cooling in order to fully purify all atoms of a BEC to one Zeeman sub-level. In addition, the magnetic field gradient generated by the

MOT coils is used in Stern-Gerlach detections to separate multiple spin components in spinor condensates. Each coil is also connected to the water cooling system, which allows for applying a high current of up to 350 A through the coils.

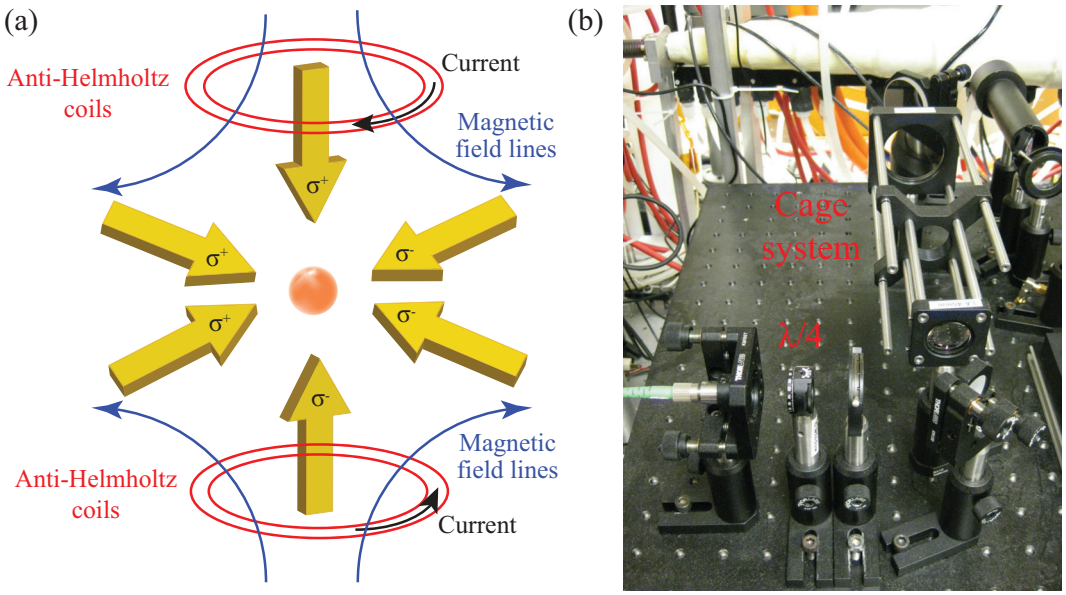

Figure 4.10: (a). Schematic of the MOT. Six circularly polarized laser beams shine from three orthogonal directions. Two anti-Helmholtz coils provide an inhomogeneous magnetic quadrupole field. (b). A cage system used to expand the MOT beam.

4.6.2 MOT alignments

The alignment of a MOT depends on the following parameters: 1) the intensity and frequency detuning of the MOT cooling beams; 2) the intensity and frequency detuning of the repumping beams; 3) a perfect overlap of all beams; 4) the polarization of each beam; 5) the magnetic field gradient. In the initial alignment, it is helpful to use laser beams of high powers. In our system, the initial laser beam powers were set at ∼25 mW and ∼4.5 mW for each cooling beam and repumping beam, respectively. Since the top and bottom MOT laser beams were Doppler-free with atoms, we first optimized the alignment for this pair of beams and slightly scanned their laser frequency by looking at the brightness of trapped atoms. When they were

overlapped well, one beam would pass through the other beam's optical path and be seen on its fiber mount. Note that the initial overlap position for each pair of beams should be at the center of viewports. The top and bottom MOT beams provided us a reference to align the side MOT beams. We slightly detuned the laser frequency from this reference and overlapped two pairs of side beams with top and bottom beams. We also scanned the currents of the slower coils, which changed the velocities of the atoms entering the MOT. We then further optimized the six MOT beams by adjusting their intensities until a weak MOT appeared. Top and bottom MOT beams capture all atoms, which provide strong confinement. Side MOT beams only capture slowed atoms, which have relative weak confinement. It is worth to mention that the polarizations of each MOT beam and the slowing beam play an important role in the MOT alignment. If the polarization or the MOT alignment is not right, MOT would be weak and trapped atoms can escape toward the direction of the misaligned beam. In our system, the optimum MOT occurred when all horizontal MOT beams were set at the σ^- polarization and vertical MOT beams were σ^+ polarized. This was due to the fact that the σ^+ to σ^- polarization configuration was also related to the the direction of the magnetic field, which set the quantization axis. One useful tip we found was that the position of the side beams should be slightly higher than the center of the viewports. After optimizing all parameters, we typically collect 2×10^9 sodium atoms in a MOT in 8.5 s, at peak density of $> 10^{11}$ cm^{-3}. Figure. 4.11 shows an actual photo of our first MOT.

4.7 Polarization gradient cooling

In our system, we apply a three-step polarization gradient cooling process after 8.5 s of MOT loading to efficiently cool 3×10^8 atoms to 40 μK, as shown in our experiment sequence in Fig. 5.7. The first polarization gradient cooling step, the strong MOT stage, compresses the MOT for 20 ms by increasing the power of each cooling beam

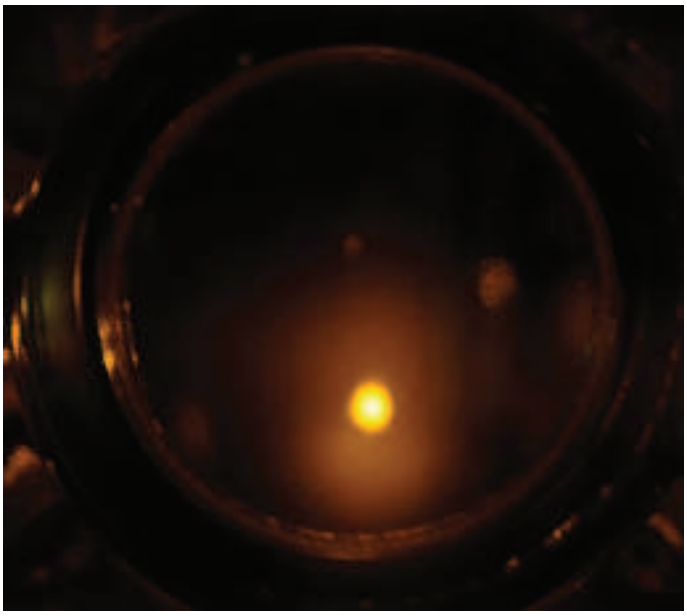

Figure 4.11: An actual photo of our MOT.

to 12 mW while changing δ_{cooling} to -15 MHz. In this step, the power of each MOT repumping beam is also drastically reduced to 45 μW. Then during a 5 ms pre-molasses step, every cooling beam is further red detuned in addition to its power being increased to 11 mW. This is followed by a 18 ms optical molasses, in which a cooling beam is detuned to $\delta_{\text{cooling}} = -45$ MHz and its power linearly drops to 5.6 mW. The magnetic field gradient is also reduced to 3 G/cm over the 18 ms. To depump atoms into the F=1 hyperfine states, the repumping beams are extinguished 1 ms before cooling beams and MOT coils are turned off. Table 4.1 shows the laser beam power budget we need in our MOT loading and cooling process.

Since both the slowing beam and repumping beam only need little power during the polarization gradient cooling, we redistribute a large amount of their power to the MOT beams by modulating the amplitude of the AOM 428 MHZ 1 and the AOM 250 MHZ 1. With this trick, we can provide enough power to each optical path at different cooling stages without increasing the laser output power. This prolongs the lifetime of the laser dye.

Stage	Slowing beam	MOT cooling beam	MOT repumping beam
Power check	25 mW	4.4 mW	2.15 mW
MOT Loading	100 mW	3.6 mW	2.15 mW
Strong MOT	0	9.1 mW	45 μW
PreMolasses1	0	11 mW	45 μW
PreMolasses2	0	10.2 mW	45 μW
Molasses	0	5.6 mW	45 μW

Table 4.1: Laser beam power for slowing beam and each MOT beam after the fiber.

4.8 Absorption imaging

4.8.1 Imaging system setup

We use absorption imaging preceded by a few milliseconds time-of-flight (TOF) to detect a MOT or a BEC. In a TOF, an atomic cloud is released from an optical or a magnetic trap and then expands ballistically. As shown in Fig. 4.12, the atomic cloud absorbs the resonant imaging light, and leaves a shadow area in an absorption image which is collected by a charge-coupled device (CCD) camera. This image is then sent to the computer for post quantitative analysis.

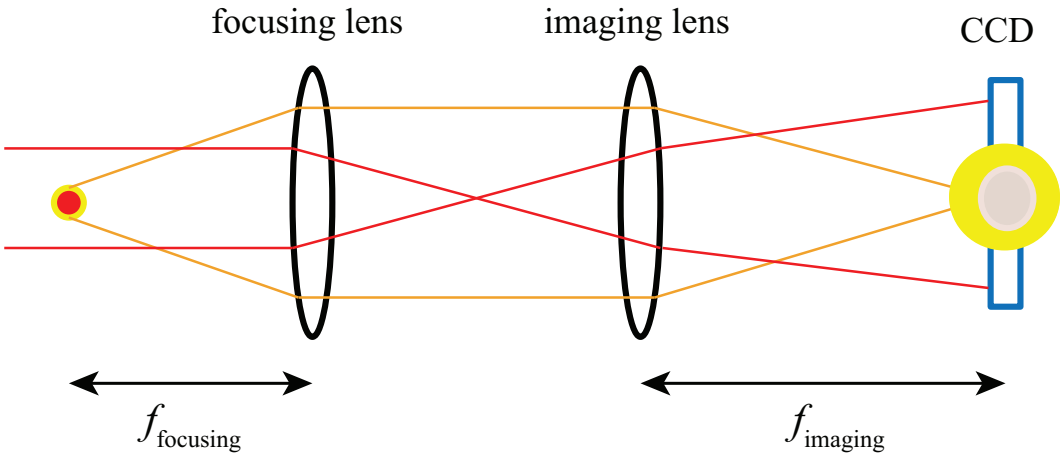

Figure 4.12: Schematic of absorption imagimg.

Figure 4.13 shows the schematic of our side absorption imaging setup. There are two imaging beam paths traveling through different viewports, which allow us to detect trapped atoms from two directions. The F=2 imaging beam delivered by a PM fiber passes through a $\lambda/2$ waveplate, a PBS, and a $\lambda/4$ waveplate, which lead the imaging beam to being circularly polarized. A telescope is used to expand and collimate the beam to a diameter of $\sim$10 mm. The laser beam power required for the imaging is usually low since overwhelming power would result in optical bleaching and blackout. For our current setup, a power of $\sim$100 μW is enough and can be measured through our imaging LabVIEW program. The two flipper mirrors (Newport 9891) allow us to select a desired imaging path. With flipper mirror 1 standing up and flipper mirror 2 laying down, our side imaging path-A passing through the 2.75" viewports is chosen. On the other hand, we can detect cold atoms from the side imaging path-B from the two 4.5" viewports. In the experiment, different imaging magnifications are used to detect a MOT or a BEC. For instance, along the side imaging path-A, we use a small magnification of M=1.5 to detect a MOT and a large magnification of M=3.5 for a BEC measurement. This can be done by using different combinations of lens. For example, we can detach the 750 mm imaging lens to make M=1.5 in order to detect a MOT. For the imaging path alignment, it is important to note that a lense should be located away from the atomic cloud by a distance exactly equaling to its focal length, and the distance between the imaging lens and the CCD chip should equal the focal length of the imaging lens. The CCD camera in our system is made by PointGrey (GRAS-14S3M-C) with a pixel size of 4.65 μm when M=1. In our system, there is an imaging path along the vertical direction as well. Compared to the side imaging, the advantage of this top imaging is that we do not need to worry about atoms fly out of the region of the CCD chip during the time-of-flight (TOF).

To detect F=1 atoms, it is necessary to turn on a repumping light originated

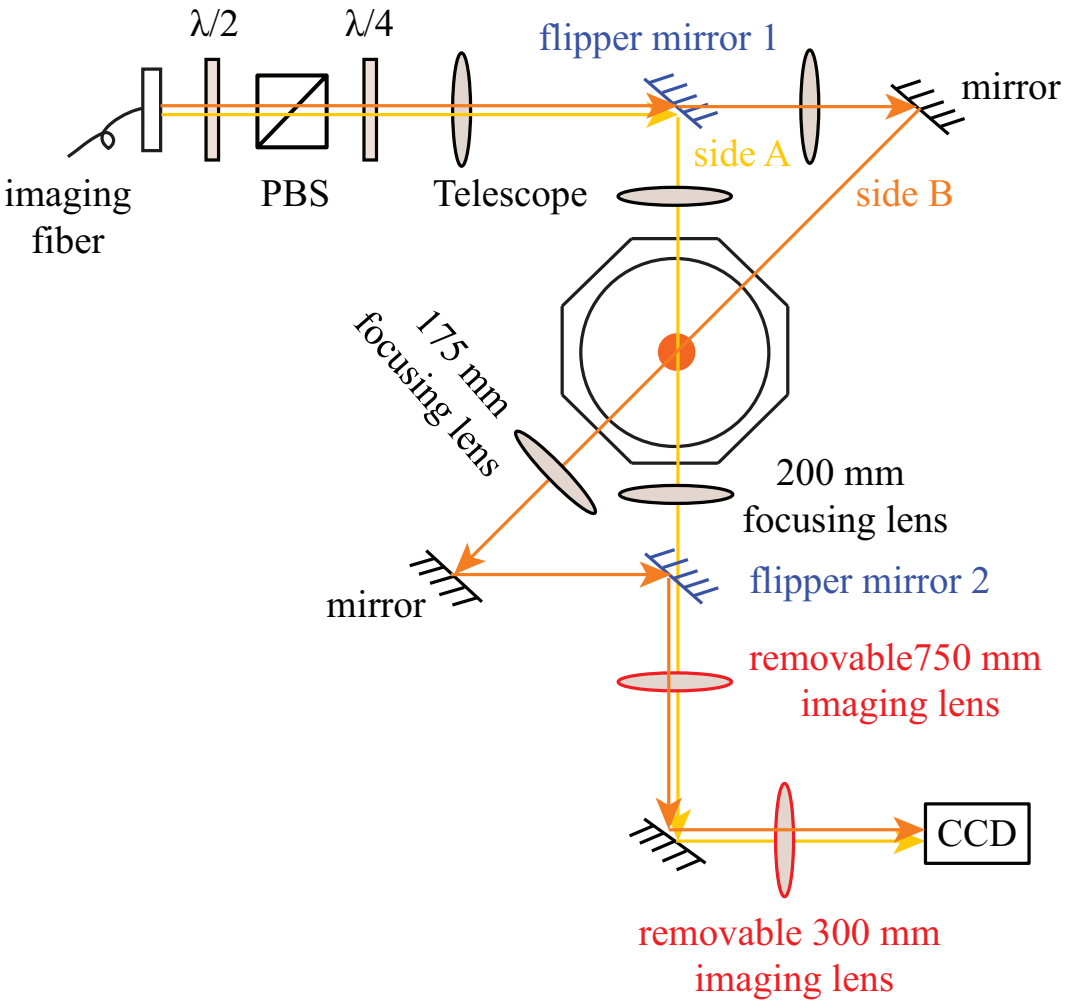

Figure 4.13: Schematic of our imaging system. Two side imaging paths at the same frequency are illustrated in yellow and red color for the clarification purpose only.

from the MOT repumping beam for 50 μs to pump the atoms to the F=2 state. The atoms are then probed by the F=2 imaging light for 80 μs. To improve the imaging efficiency, the repumping light is kept on during the 80 μs probe period. Absorption images are captured by the CCD camera. A TTL logic signal is used to trigger the camera. Note that since the response time of optical shutters is around 3 ms, we use an AOM to provide a sufficiently fast control to the imaging beam. The interval between three different pictures is 300 ms, which ensures that the system have enough time to transfer and process the data.

4.8.2 Image analysis

For an absorption imaging process, the intensity $I(x, y, z)$ of an imaging beam traveling in the vertical direction (z-axis) would decrease after the beam passes trough the atomic cloud, which can be expressed as

$$\frac{dI(x, y, z)}{dz} = -\sigma n(x, y, z) I(x, y, z). \tag{4.2}$$

Here $n(x, y, z)$ is the atomic density and σ is the absorption cross section.

If we define $I_0(x, y)$ as the light intensity before the imaging beam passes through the atomic cloud, the light intensity after the absorption is

$$I(x, y) = I_0(x, y) exp[-\sigma \int n(x, y, z) dz]. \tag{4.3}$$

The optical density profile of the atomic cloud can be calculated as

$$OD(x, y) = -\ln \frac{I(x, y)}{I_0(x, y)}. \tag{4.4}$$

This can be done by taking two pictures, the absorption image with atoms $I(x, y)$ and the probe image without atoms $I_0(x, y)$. We take an additional picture without the imaging light and atoms to extract the background noise intensity $I_{bg}(x, y)$. Then $OD(x, y)$ can be rewritten as follows,

$$OD(x, y) = -\ln \frac{I(x, y) - I_{bg}(x, y)}{I_0(x, y) - I_{bg}(x, y)}. \tag{4.5}$$

Some experimental factors such as distortion, effects due to imperfect optical elements, and uneven intensity distributions of the imaging lights can be eliminated in the calculation since the absorption imaging takes count of the relative transmission of the imaging light as long as the position of the CCD camera is fixed. We can thus extract information of the atomic cloud such as its atom number and temperature from the absorption images as described below.

Atom number Based on the optical density profile, the total number of atoms N_{count} can be calculated by Eq. (4.5) by summing up all the absorption signals collected by the CCD camera in TOF images, which is given by

$$N_{count} = \frac{A_{pix}}{\sigma} \sum_{pixels} OD(x, y). \tag{4.6}$$

Here A_{pix} is the effective pixel area at different magnification M, and σ is the absorption cross-section. Note that $A_{pix} = A_{M=1}B^2/M^2$, where $A_{M=1}$ is (4.65 μm)^2 for our camera and B represents the number of pixels binned together in the Igor program.

Atom temperature TOF images show momentum distributions of atomic clouds. In free expansion, the momentum distribution of atoms would be changed to spatial distribution, which can be used to measure the temperature. By applying a 2D gaussian fit, we can extract the width of the atomic cloud. The expansion of the atomic cloud as a function of time follows $x(t) = \sqrt{x^2(0) + \upsilon^2 t^2}$. Here $x(t)$ is the size of the atomic cloud after an expansion, $x(0)$ represents the initial size, and υ is the velocity of the atoms. According to the equipartition theorem, the temperature of the atomic cloud can be found by $x(t) = \sqrt{x^2(0) + (k_{\mathrm{B}}T/M)t^2}$ at different TOF. Figure 4.14 shows a typical fit to extract the temperature of a MOT.

4.9 Crossed optical dipole traps

An optical dipole trap (ODT) is one of the most important setups in our system since we use all-optical method to create BECs. The laser cooled atoms are loaded into

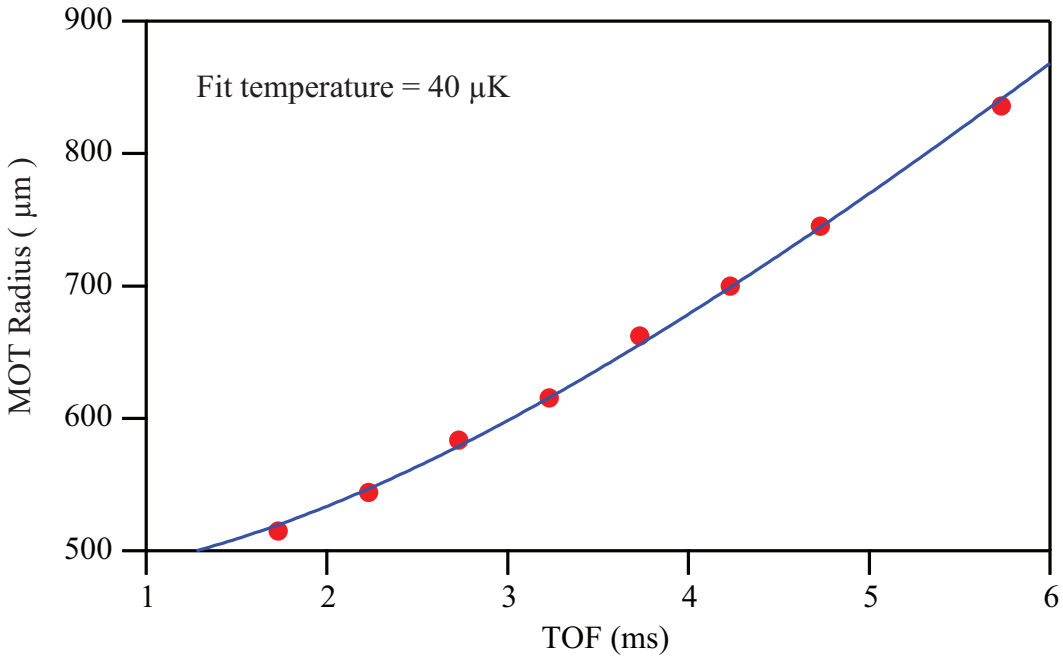

Figure 4.14: A typical fit to extract the temperature of a MOT.

the ODT and then a forced evaporative cooling is applied to achieve BECs.

4.9.1 Setup of a crossed ODT

In our system, a crossed ODT consists of two far-detuned beams which originate from an infrared (IR) laser (IPG photonics YLR-50-1064-LP) with an outputting power of 15 W at 1064 nm. The power of the ODT laser beam is controlled by an AOM. A custom-made high power single-mode PM fiber (Toptica, Inc) is used to deliver the laser beam power to the main chamber. The advantage of using a fiber is to polish the beam mode and minimize pointing fluctuations due to imperfections of the IR laser and thermal contractions of an AOM. The typical coupling efficiency for this high power fiber is above 70% after we choose a proper telescope. Care must be taken when dealing with this fiber since any small misalignment may cause the fiber to be burned. According to my own experience, a F220FC-1064 fiber collimation package from Thorlabs would be a good choice to align this fiber because its core size is a little larger than those of our yellow fibers. Also the optimized distance between the

lenses would be slightly different when the laser output power changed. In order to achieve a desired beam waist of our ODT with as few optics as possible, we use a combination of one Thorlabs F810FC-1064 collimation package and a single IR lens to focus down the laser beam. Atoms which are transferred from the MOT into the tightly-focused crossed ODT demonstrate a long lifetime of 8 s and a large collision rate. These are essential for all-optical BEC approaches. Figure. 4.15 shows the schematic of our crossed ODT setup. The trap potential of the crossed ODTs can be described as $P = P_1 + P_2 + P_g$, where P_1 and P_2 are trap potentials of the two single beam ODTs, and P_g is due to the influence of gravity, as shown in Fig. 4.16.

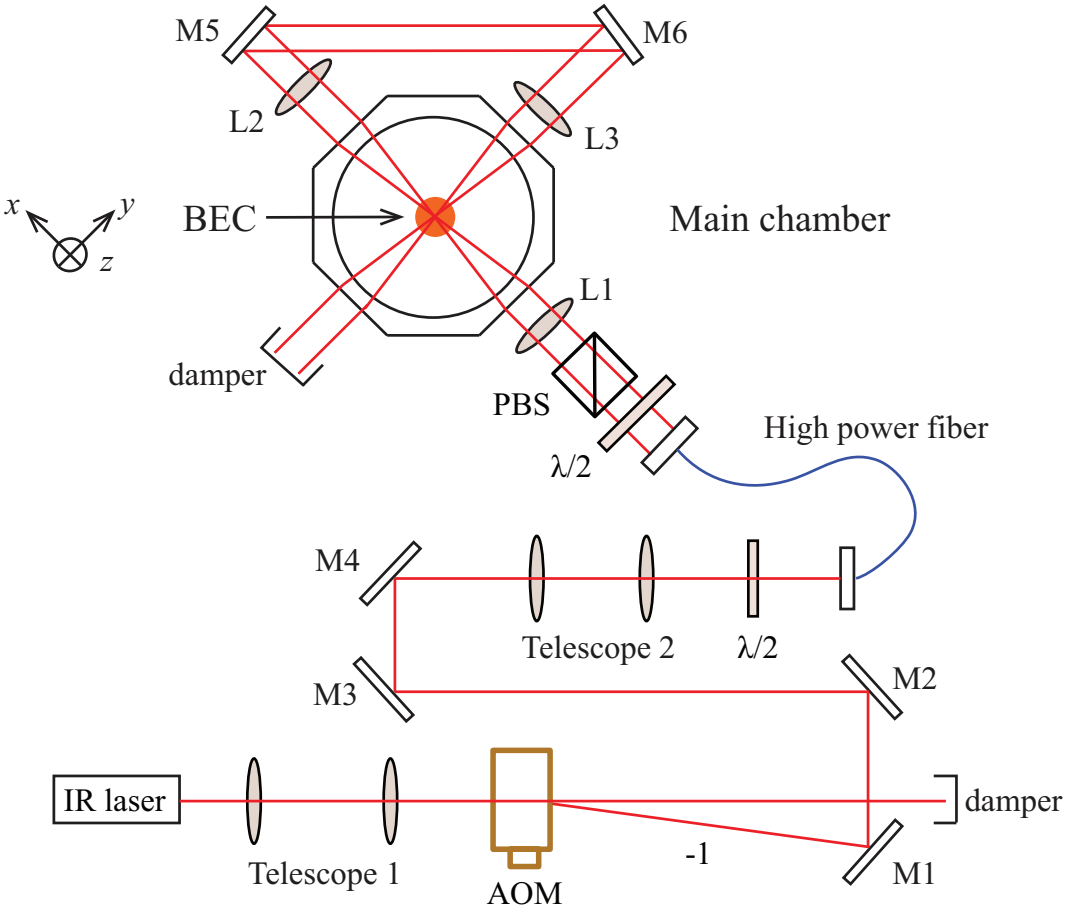

Figure 4.15: Schematic of the crossed ODT setup around the main chamber. The positive z-axis represents the direction of gravity.

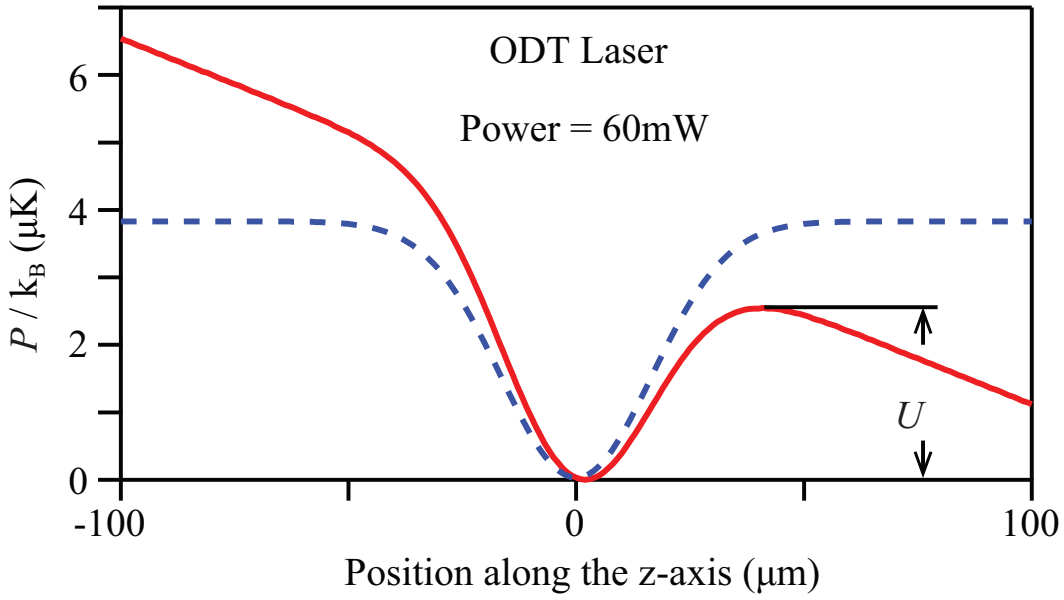

Figure 4.16: The definition of the ODT trap depth U. The solid red line and dashed blue line represent the crossed ODT's trap potential energy P as a function of position along the z-axis with or without taking into account of the influence of gravity, respectively. Here $x = y = 0$ and the ODT laser power is 60 mW.

4.9.2 ODT beam alignment

It is not an easy task to find the initial signal for the ODT beam, so we developed a procedure to align the ODT beam with the help of our yellow laser light. First, we mimicked the desired optical beam path traveling through the atoms on an optical table and used a beam profiler (Thorlabs BC106N-VIS) to roughly calibrate the beam waist, which provided us a general idea of the choice of the focusing lens and the output fiber collimator. Second, we constructed the ODT beam path with all IR-coating optics but with a resonant yellow beam. In other words, we replaced our high power IR fiber with a yellow light fiber for a rough alignment. Here the F=2 imaging light was chosen since it could easily tell us whether we successfully align the beam to the atomic cloud or not. Once the MOT was "killed" by the imaging beam, this indicated that this beam path passed through the atomic cloud. Then at least two apertures should be accurately set before and after the chamber as two references for the following IR laser beam alignment. To improve the accuracy of the alignment, we generally located a third aperture or left a mark on the wall in a far field along the beam path.

Now the Toptica IR fiber could be switched back to align the ODT beam pass through the two apertures, and the focusing lens should be located at the position estimated by the beam profiler. With the IR laser set at a high power, the position of the ODT beam in our MOT could be observed from absorption images. The ODT beam was then aligned to the MOT center in both horizontal and vertical directions by the pictures taken from side and top CCD cameras, as shown in Fig. 4.17(a). After this initial rough alignment, some evaporative cooling was applied to locate the intersection point of the two ODT beams. The focus of the ODT beam could be found by recording the center position of the trapped atoms after a short or long hold time inside the ODT, since atoms tend to be attracted to the beam waist position. In addition, the polarization of the ODT beam was found to also contribute to the

alignment: the best crossed ODT is only achieved when the input ODT beam is horizontally linearly-polarized. If the input ODT beam was vertically polarized, it was hard to find a cross point from the two ODT beams. Last but not the least, I would emphasize the importance of a well focused imaging system since one might not be able to identify the initial signal of the ODT beam if the imaging system was defocused too much. In this situation, the ODT beam in the absorption image would tend to be very wide and blur although the MOT picture still looked good. After a careful alignment for our two ODT beams, a crossed ODT was achieved, as shown in Fig. 4.17(b).

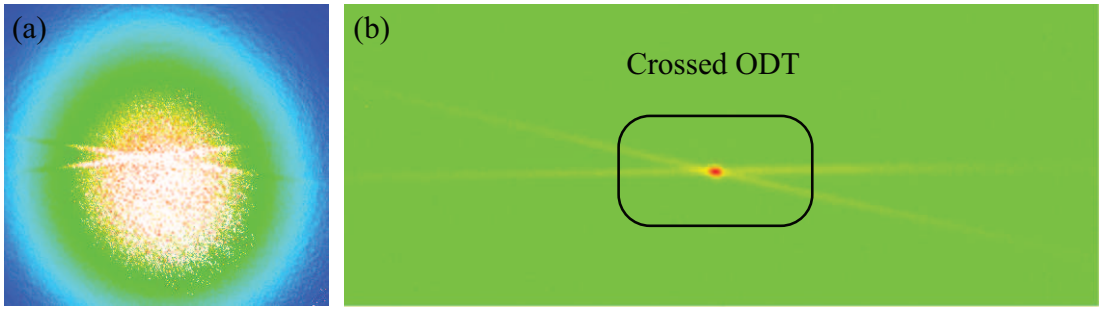

Figure 4.17: (a). A typical side view absorption image of our crossed ODT with the presence of MOT. (b). A typical side view absorption image of our crossed ODT after some evaporation.

4.9.3 Calibration of the waist of an ODT beam

We determine the waist of an ODT beam by measuring its trap frequency with two methods. First, we measure the radial frequency of a single ODT beam with the well-known parametric heating method [102]. In this method, we recorded the number of atoms in the ODT after sinusoidally modulating U at various modulation frequency f_{m}. The number of atoms exhibits parametric resonances at $f_{\mathrm{m}} = l \cdot f_{\mathrm{ODT}}$, where f_{ODT} is the ODT's radial frequency and l is a positive integer number. By knowing the trap frequency and laser power, we can derive the value of the beam waist according to

Eq. (2.17) and Eq. (2.18). In our experiment, we lowed down the power of our ODT beam to 0.8 W during the evaporative cooling process and applied a ∼20% sinusoidal amplitude modulation for 50 ms. After scanning the different modulation frequencies and recording the atom number with TOF pictures, we found that $f_{\mathrm{ODT}} \approx 900$ Hz, as shown in Fig. 4.18.

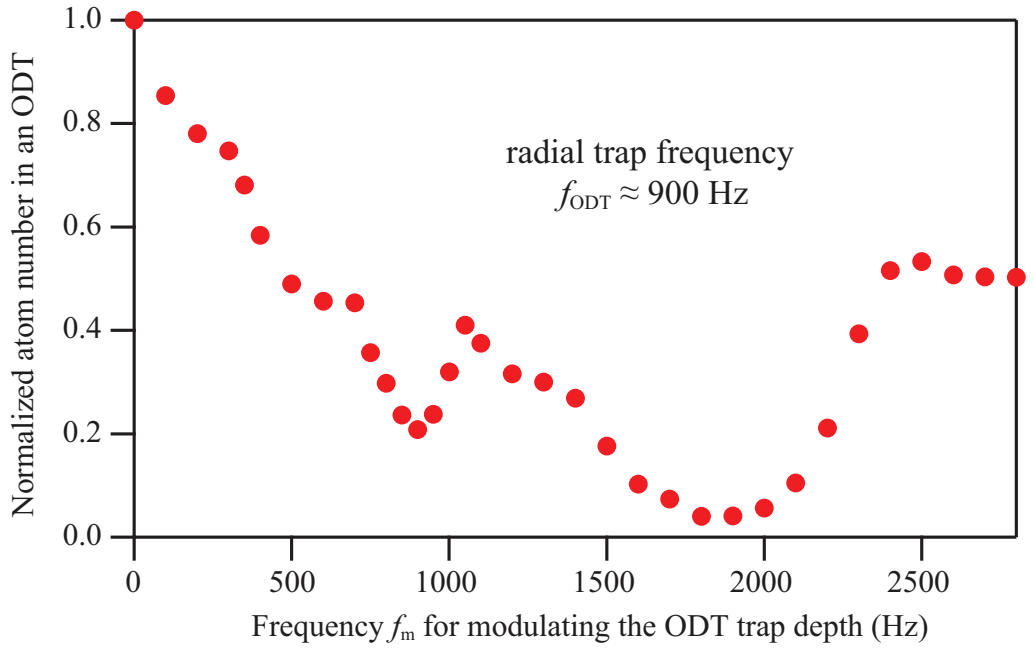

Figure 4.18: The normalized number of atoms in a single beam ODT as a function of f_{m} in the parametric heating method. Here the ODT beam power is 0.8W.

In the second method, we kick atoms in the single-beam ODT with a magnetic field gradient and then record the position of atoms after holding the atoms in the ODT for a variable length of time. It appears that atoms experienced a harmonic oscillation with a frequency equal to the ODT's axial frequency, as shown in Fig. 4.19. It turns out that the values of the ODT's beam waist provided by these two methods are very close to each other, which are 33 μm. (Note that we also applied the same methods to measure the beam waist for our second crossed ODT beam, and got a beam waist of 28 μm in our current system.) In addition, we implement high-resolution imaging with a resolution of 1-2 micron in three orthogonal directions. This ensures the two

ODT beams were well intersected at their focal points.

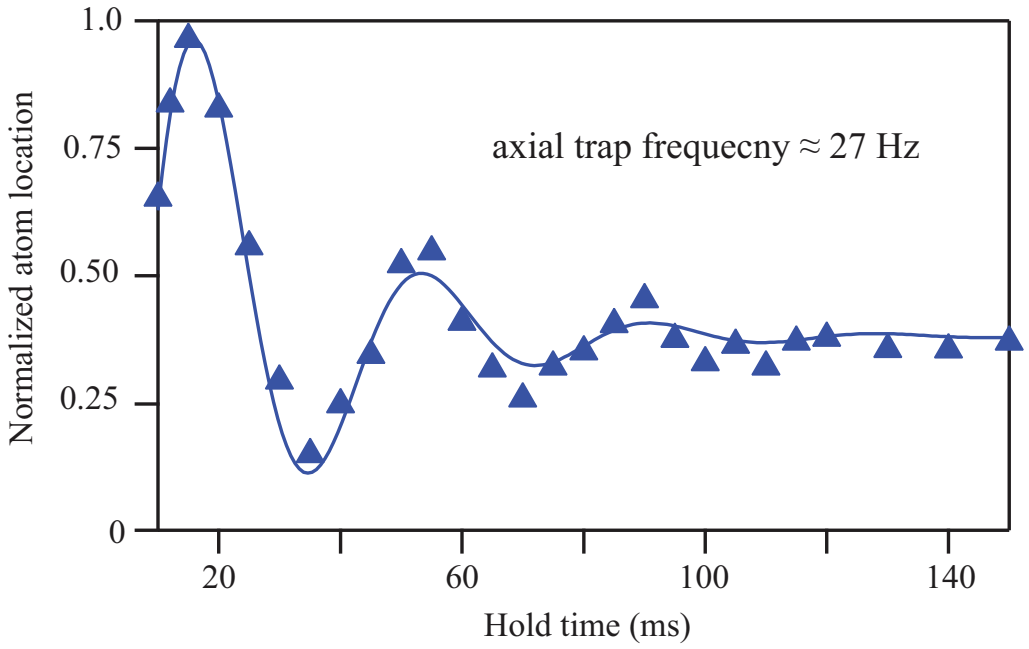

Figure 4.19: A harmonic oscillation which atoms experienced after being kicked by a magnetic field gradient in the second method, when the ODT beam power is 13W. The solid line is a fit with a damped sinusoid.

4.10 Computer control

A computer control program is essential for generating BECs in the experiment. It precisely controls timing sequences in the experiment as well as provides digital and analog signals for various devices, such as optical shutters, AOMs, and MOSFETs. In our system, we use a 24 channels Spincore PulseBlaster (PB24-100-64k) card to produce digital signals and three 16-Bit NI PCI-6733 DAQ cards for outputting analog signals. A NI shielded cable (SH68-68-EPA) and a connector block (SCB-68A) are used with each PCI card to provide robust and low-noise signal termination. The digital and analog cards are synchronized with a RTSI cable. By using the LabVIEW program, we can output all the necessary signals and easily modify them during an experiment sequence. In addition, we have built some buffer boxes to isolate and

amplify our output signals before sending them to different devices. Our design of various servo control circuits can be found in the dissertation of Lichao Zhao, one of my labmates.

CHAPTER 5

All-optical production of sodium spinor BECs

This chapter presents an all-optical production of a sodium spinor BEC and an experimental study on the spin-mixing dynamics in antiferromagnetic spinor BECs. Two papers related to these topics were published:

- J. Jiang, L. Zhao, M. Webb, N. Jiang, H. Yang, and Y. Liu, *Simple and efficient all-optical production of spinor condensates*, Phys. Rev. A **88**, 033620 (2013).
- L. Zhao, J. Jiang, T. Tang, M. Webb, and Y. Liu, Dynamics in spinor condensates tuned by a microwave dressing field, Phys. Rev. A **89**, 023608 (2014).

In the last two decades, many techniques have been developed to reliably generate a BEC of more than 10^4 atoms. Almost every one of these techniques requires evaporative cooling in a trapping potential, including a magnetic trap, an optical dipole trap (ODT), or a combined magnetic and optical potential [15, 16, 17, 103, 104]. Among these techniques, all-optical methods have been proven to be versatile and popularly applied in producing quantum degenerate gases of both bosonic [19, 52, 88, 105, 106, 107, 108, 109, 110] and fermionic [111] species. ODTs have tight confinement which allows for fast evaporation with a duty cycle of a few seconds [52]. Unlike magnetic potentials that only trap atoms in the weak-field seeking spin state, an ODT can confine all spin components. This is crucial for creating vector (spinor) BECs with a spin degree of freedom [112]. ODTs can also be applied to a wider variety of atomic species (e.g., Ytterbium, alkaline earth metals, and Cesium) which cannot be feasibly condensed in a magnetic trap [19, 109]. In addition, optical trap-

ping does not require magnetic coils around trapped atoms, which not only provides better optical access but also reduces residual magnetic fields. The simplicity and versatility of ODTs widen the accessibility of BEC research on many-body physics, precision measurements, and quantum information science [55].

We develop an optimal ODT ramp and evaporation sequence for an all-optical production of sodium BECs. With this optimal scheme, the number of atoms in a pure BEC is greatly boosted by a factor of 5 over some popular schemes and evaporation efficiency $\gamma = -d(\ln D)/d(\ln N)$ can be 3.5 in a crossed ODT. Here D is the phase space density and N is the number of atoms. We also show an upper limit for γ at a given truncation parameter $\eta = U/\mathrm{k_B T}$, and demonstrate that a constant η does not yield more efficient evaporative cooling. This optimal experimental scheme allows us to avoid technical challenges associated with some all-optical BEC approaches.

5.1 Efficiently loading laser-cooled atoms to an ODT

A couple of ODT ramp sequences were proposed to improve the ODT capture efficiency by finding a reasonable balance between two competing ODT-induced effects [52, 88, 105, 106, 108, 109, 110, 113, 114], as shown in Fig. 5.1. First, a larger U enables more atoms to be captured in the ODT if the ODT beams do not interact with the MOT. The number of atoms loaded in the ODT is $N_{\mathrm{rampA}} \sim \int_0^U \rho(\epsilon) f(\epsilon) d\epsilon$, where $\rho(\epsilon)$ and $f(\epsilon)$ are the density of states and occupation number at energy ϵ, respectively. This is confirmed by our data (blue triangles in Fig. 5.2) taken with the scheme-A, in which the ODT depth is linearly ramped in 5 ms from 0 to U_0 immediately after MOT beams are switched off. On the other hand, there are some advantages to turn on intense ODT beams in the presence of MOT beams. For example, this allows the ODT to capture a larger number of cold and dense atoms by using MOT beams to prevent the gas from expanding. However, atoms experience non-negligible AC Stark shifts in regions where the ODT beams and the MOT over-

lap. As a result, the MOT's cooling capability is impaired in the MOT and ODT overlapping regions, and the number of atoms loaded into the ODT decreases when the ODT becomes too deep. N is thus not a monotonic function of U.

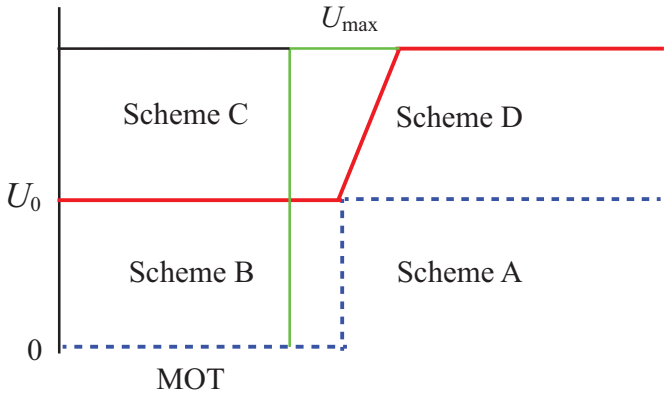

Figure 5.1: Different ODT ramping sequences of all-optical BEC production approaches.

The scheme-B (green squares in Fig. 5.2) is a popular scheme used to improve the ODT capture efficiency, in which ODT beams overlap with a MOT for a very short amount of time (20 $\sim$ 200 ms) before the MOT beams are switched off [108, 110, 113, 114]. The scheme-C (black crosses in Fig. 5.2) is another widely-applied scheme, which keeps the ODT beam at its maximum power during the entire MOT stage [52, 88, 106, 109]. Figure 5.2 clearly shows that there is an optimal scheme which can increase the number of atoms loaded into the crossed ODT by a factor of 2.5 over the above two popular schemes. This optimal scheme is the best scenario of our scheme-D. As shown in Fig. 5.1, the ODT in the scheme-D is kept at a small trap depth U_0 during the entire laser cooling process and then linearly ramped to $U_{\max}$ in $t_{\text{ramp}} = 5$ ms. $U_{\max} \approx \text{k}_\text{B} \times 800\ \mu\text{K}$ is the maximal trap depth used in this work and $0 \leq\ U_0 \leq U_{\max}$. The number of atoms loaded into the ODT in the scheme-D may be expressed as $N_{\text{rampD}} \sim A \cdot \xi(U_0) \int_0^{U_0} \rho(\epsilon) f(\epsilon) d\epsilon + \int_{U_0}^{U_{\max}} \rho(\epsilon) f(\epsilon) d\epsilon$. Here $\xi(U_0) = \exp(-(\delta_{\text{ODT}}(U_0))^2/\omega_0^2)$ is a correction factor due to the ODT-induced shift $\delta_{\text{ODT}}(U_0)$, while A and ω_0 are fitting parameters. Our data collected with the scheme-

D (red circles in Fig. 5.2) can be well fit by this model. The fit value of ω_0 is 1.2Γ, where $\Gamma/2\pi = 9.7$ MHz is the natural linewidth of sodium. The number of atoms in the ODT reaches its peak when the optimal ramp sequence with $U_0 \simeq U_{\max}/2$ is applied. Compared to the two popular schemes, the optimal scheme allows us to use ODT beams with smaller waists while loading the same amount of laser-cooled atoms to the ODT. The resulted high initial atom density and high collision rates from the optimal scheme enable very efficient evaporative cooling. This greatly boosts the number of atoms in a BEC by a factor of 5 over the two popular schemes for our apparatus, as shown in the inset of Fig. 5.2.

Our optimal scheme leads to a better ODT capture efficiency at every given frequency of the MOT beams within a wide range (i.e., -24 MHz $\leq \delta_{\text{cooling}} \leq -10$ MHz and -15 MHz $\leq \delta_{\text{repump}} \leq 6$ MHz), as shown in Fig. 5.3. Two important results can be found from Fig. 5.3: a) our optimal scheme (red circles in the figure) leads to a better ODT capture efficiency than the scheme-B at every given frequency of the MOT beams; b) this enhanced ODT capture efficiency cannot be achieved by only changing the frequency detuning of the MOT beams. One mechanism may explain this phenomenon: well-aligned crossed ODT beams have a much larger intensity in the intersection region than that in the "wing" (non-intersecting) region. In other words, the light shift induced by the ODT beams is not uniform, i.e., a big shift in the intersection region and a small shift in the "wing" region. These ODT induced non-uniform shifts cannot be mimicked by simply varying the frequencies of the MOT cooling and repumping beams. Because this mechanism does not depend on atomic species, our optimal scheme may thus be applicable to rubidium and other optical trappable atomic species.

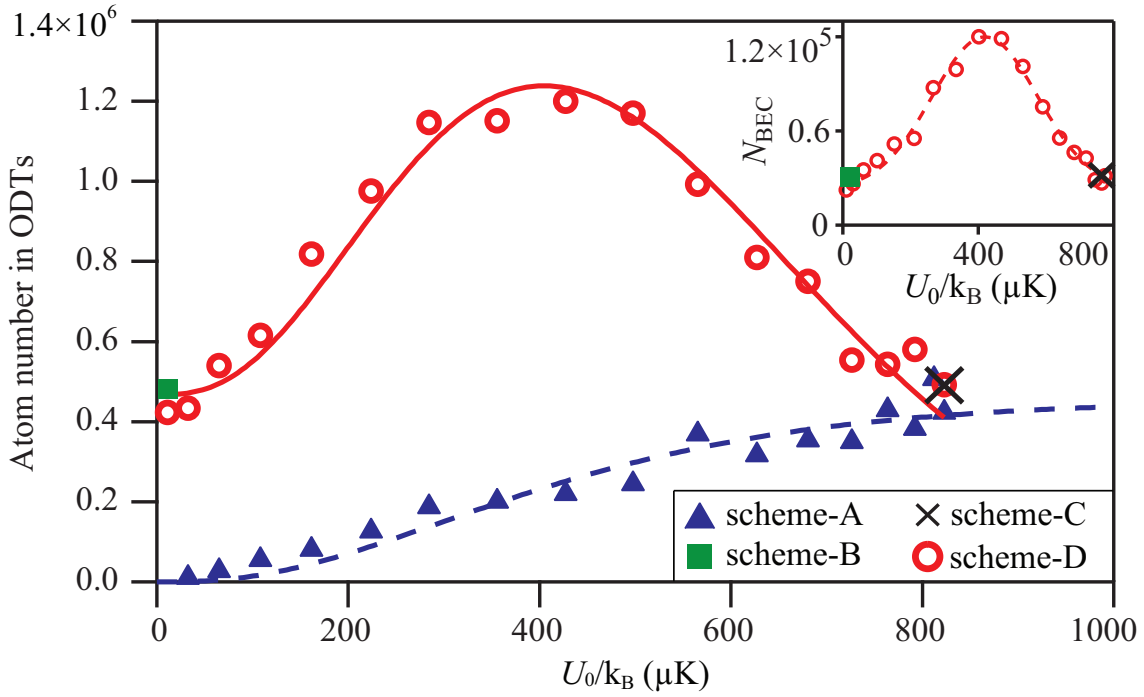

Figure 5.2: The number of atoms captured in the crossed ODT as a function of U_0 with the four ODT ramp sequences. Our optimal scheme is the best scenario of the scheme-D when $U_0 \simeq U_{\max}/2$. The dashed (blue) line and the solid (red) line are fits based on N_{rampA} and N_{rampD}, respectively (see text). Inset: the number of atoms in a BEC as a function of U_0, when one of the three schemes (i.e., schemes B-D) and a same evaporation curve are applied. The dashed (red) line is a Gaussian fit to the data.

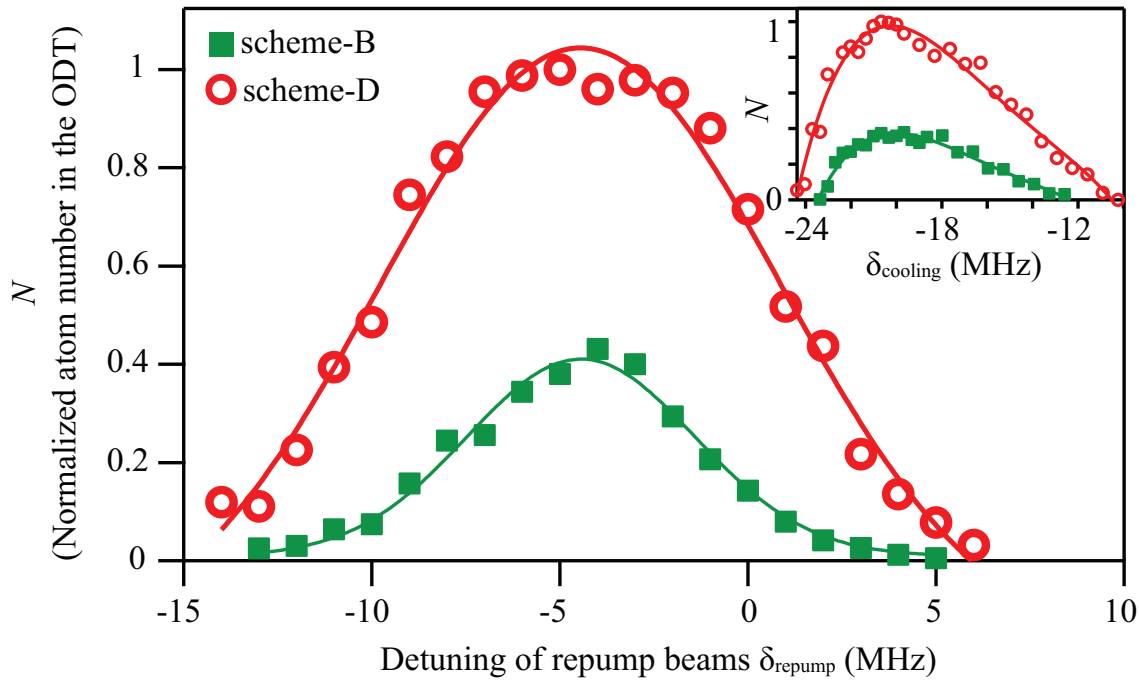

Figure 5.3: N (the normalized number of atoms in the crossed ODT) as a function of δ_{repump}. Red circles are data taken with our optimal scheme, while green squares are data taken with the scheme-B which was used in Ref. [113]. δ_{repump} is the frequency detuning of MOT repumping beams with respect to the $|\text{F} = 1\rangle$ to $|\text{F}' = 2\rangle$ transition. Lines are Gaussian fits to the data. Inset: N as a function of δ_{cooling} with our optimal scheme (red circles) and the scheme-B (green squares). δ_{cooling} is the frequency detuning of MOT cooling beams with respect to the cycling transition. Lines are polynomial fits to the data to guide the eye.

5.2 Optimizing the efficiency of an evaporative cooling in an ODT

Forced evaporation in an ODT can be performed by simply reducing its trap depth U (e.g., lowering the trapping laser power). In this process, collision rates decrease with U, which leads to slow rethermalization and eventually stagnation in evaporative cooling. Several methods have been reported to overcome this difficulty, including tilting an ODT with a magnetic field gradient [115], using a misaligned crossed ODT [108, 110], compressing an ODT with a mobile lens [107], or applying multiple ODTs for staged evaporation [19, 106]. However, we show that these methods may not be necessary for some atomic species, in particular, sodium atoms.

To optimize evaporation efficiency γ, we need to understand the time evolution of the system energy E and the atom number N during an evaporation process. Similar to Refs. [90, 110, 116, 117], we use $\kappa \mathrm{k_B} T \approx (\eta-5)/(\eta-4)\mathrm{k_B} T$ to represent the average kinetic energy taken by an atom when it is removed from the ODT. And we assume the mean kinetic energy and mean potential energy to be $E/2$ when η is large. By taking account of inelastic loss, the time evolution of E and N is thus given by

$$\begin{aligned} \dot{E} =& -\frac{2(\eta-4)\mathrm{e}^{-\eta}N}{\tau_2}(U+\kappa \mathrm{k_B} T) + \frac{\dot{U}}{U}\frac{E}{2} + \dot{E}|_{\mathrm{loss}} \ , \\ \dot{N} =& -2(\eta-4)\mathrm{e}^{-\eta}N/\tau_2 + \dot{N}|_{\mathrm{loss}} \ , \end{aligned} \tag{5.1}$$

where τ_2 is the time constant of the two-body elastic collision. In Eq. (5.1), $\dot{E}|_{\mathrm{loss}}$ and $\dot{N}|_{\mathrm{loss}}$ are due to various inelastic loss mechanisms and may be expressed as,

$$\begin{aligned} \dot{E}|_{\mathrm{loss}} =& k_{\mathrm{s}}N - k_1 N(3\mathrm{k_B} T) - k_3 n^2 N(2\mathrm{k_B} T) \ , \\ \dot{N}|_{\mathrm{loss}} =& -k_1 N - k_3 n^2 N \ , \end{aligned} \tag{5.2}$$

where k_1 and k_3 are one-body and three-body loss rates, respectively. k_{s} represents heating introduced by ODT beams via a number of different mechanisms, such as pointing fluctuations of the ODT beams, bad laser beam mode, and spontaneous light scattering. The term $2\mathrm{k_B} T$ in Eq. (5.2) accounts for the fact that atoms in

the ODT's center have higher density and thus are more affected by the three-body inelastic loss [108].

In our apparatus with the UHV pressure in the 10^{-12} Torr range, background collisions are negligible. Since the ODT beams are delivered via a single-mode polarization maintaining fiber, heating induced by the ODT beams is minimized. k_1 and k_s are thus very small. If we ignore k_1 and k_s, Eq. (5.1) can be simplified to

$$\dot{E} = \dot{N}\eta_{\text{eff}} k_B T + \frac{\dot{U}}{U}\frac{E}{2} , \tag{5.3}$$

where $\eta_{\text{eff}} = \eta+\kappa-R(\eta+\kappa-2)$. We define $R = (\dot{N}|_{\text{loss}})/\dot{N} = 1/(1+2(\eta-4)e^{-\eta}R_{\text{gTb}})$ to represent the portion of atom losses due to inelastic collisions, where R_{gTb} is the ratio of inelastic collision time constant to τ_2. From solving the above equations, γ may be expressed as,

$$\gamma = -d(\ln D)/d(\ln N) = \eta_{\text{eff}} - 4 = \eta + \kappa - R(\eta + \kappa - 2) - 4 , \tag{5.4}$$

The evaporation efficiency γ is an important parameter to quantify the efficiency of an evaporative cooling. The phase space density D must increase in every atom-loss step to ensure an effective evaporation, which leads to a positive γ. Figure 5.4 shows a typical relationship between D and N. Evaporation efficiency γ is extracted from a fit based on Eq. (5.4), as shown by the red line in Fig. 5.4.

The value of η in many publications on optical productions of BECs was held constant with $\Delta\eta = 0$ [52, 105, 107, 108, 110, 111, 115]. Our data in Fig. 5.5, however, shows that a constant η does not lead to better evaporation or a larger γ. The values of γ in this figure are extracted from 36 evaporation processes in which the forced evaporation speed and the hold time at $U_{\max}$ are changed independently, although they all start with the same initial number of cold atoms in the crossed ODT. $\Delta\eta = \eta_f - \eta_i$ is the change of η during forced evaporation, where η_i and η_f are the values of η at $U_{\max}$ (i.e., the beginning of forced evaporation), and at U_f, respectively. In order to avoid overestimating γ due to the Bosonic enhancement near the BEC

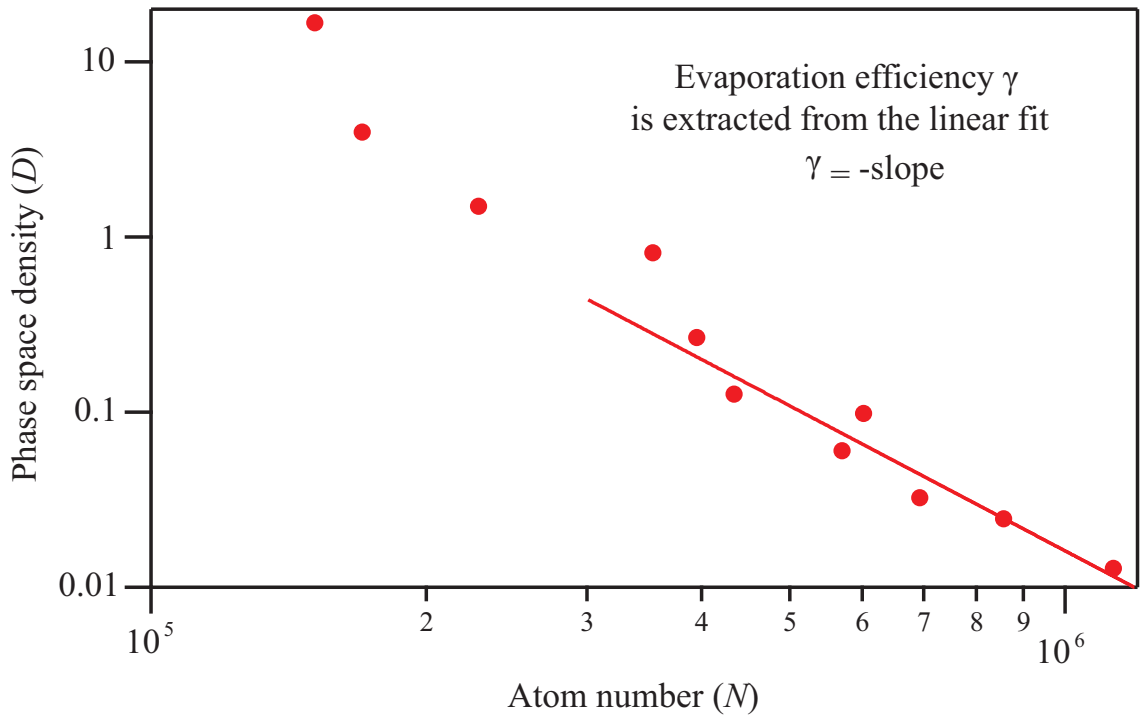

Figure 5.4: Phase space density D as a function of atom number N. Both axes are in logarithmic scale. Evaporation efficiency γ is extracted from a fit based on Eq. (5.4).

transition temperature, we choose $U_{\rm f} = {\rm k_B} \times 30\ \mu$K where no BEC appears. We find that $\Delta\eta$ tends to be a non-negative value when the forced evaporation time is longer than 1 s (solid black squares in Fig. 5.5), which is a good indication of sufficient rethermalization. We also find that γ is too small to yield a BEC when $\Delta\eta < -2.5$.

We compare the evaporation efficiency at different values of $\eta_{\rm i}$, as shown in the inset of Fig. 5.5. $\gamma_{\rm best}$ (the best achieved value of γ at a given η_i in our system) does not show a strong dependence on η_i if $8 < \eta_i < 10$, while $\gamma_{\rm best}$ sharply diminishes when η_i becomes too large or too small. In the inset of Fig. 5.5, the similar relationship between γ and η_i is also predicted by the solid (blue) line, which is a result based on Eq. (5.4) by ignoring k_1 and $k_{\rm s}$ and by applying a non-zero R (i.e. $R_{\rm gTb} = 4000$ [103]). All of our data lie below the solid line in this figure, which may indicate that k_1 and $k_{\rm s}$ are larger than 0 and cannot be ignored. Therefore, based on Fig. 5.5, we need to choose a value between 8 and 10 for η_i and keep $\Delta\eta$ larger than -0.5 in order to

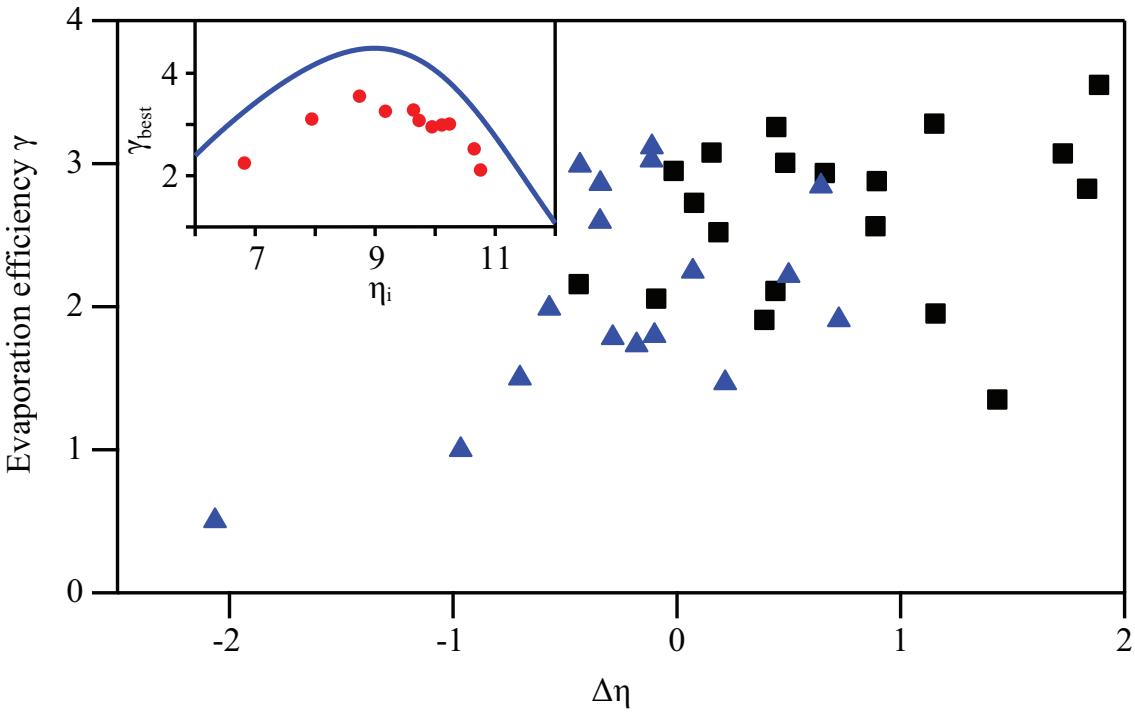

Figure 5.5: Evaporation efficiency γ in 36 different evaporation processes as a function of $\Delta\eta$. Solid black squares are data taken with the forced evaporation time longer than 1 s. Inset: γ_{best} as a function of η_{i} extracted from the main figure. The solid line sets an upper limit for γ based on Eq. (5.4) by assuming $k_1 = k_{\mathrm{s}} = 0$.

optimize evaporation efficiency γ.

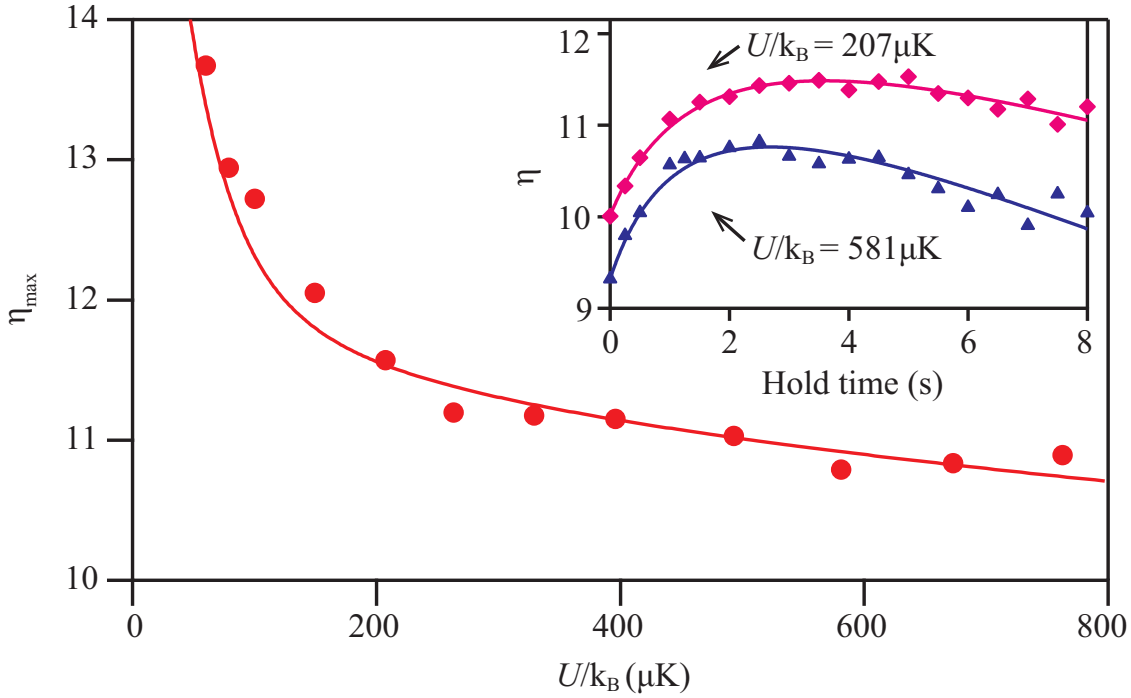

Figure 5.6: $\eta_{\max}$ as a function of the ODT depth U, when atoms are held at a fixed U for 8 s. The solid line is a fit based on Eqs. (5.1-5.2). Inset: the time evolution of η at two typical ODT depths. Solid lines are fits based on the same model applied in the main figure.

The maximum achievable value for $\eta_{\rm i}$ appears to be 10.8, as shown in the inset of Fig. 5.5. To understand this, we monitor the time evolution of η and find that η has a maximal value ($\eta_{\max}$) at a given ODT depth U. The value of $\eta_{\max}$ decreases exponentially with U and $\eta_{\max}$ at $U_{\max}$ is 10.8, which agrees well with our theoretical prediction (solid red line in Fig. 5.6). Therefore, if one wishes to keep η unchanged during forced evaporation, η must be limited to 10.8 even though $\eta_{\max}$ can be much higher at low ODT depths (e.g., $\eta_{\max} > 13$ for $U/k_B < 100$ μK). This may be one reason why a constant η does not yield more efficient evaporative cooling. We also find that the time evolution of η at every U discussed in this report can be well fit with our model. Two typical fitting curves are shown in the inset of Fig. 5.6.

5.3 An optimum scheme to generate sodium Bose-Einstein condensates

Figure 5.7 shows a typical experimental sequence for our all-optical BEC approach. A pure F=1 BEC of 1.2×10^5 sodium atoms at 50 nK is created from a 0.45 s free evaporation at $U_{\max}$ followed by a 5 s forced evaporation in which U is exponentially reduced. This evaporation curve provides two important parameters for efficient evaporative cooling: η_i is between 8 and 10, and the forced evaporation time is long enough for sufficient rethermalization but short enough to avoid excessive atom losses. A series of time-of-flight absorption images taken with a same evaporation curve is shown in Fig. 5.8(a). Three 10 ms time-of-flight absorption images in Fig. 5.8(b) show a typical change of the condensate fraction (CF) after interrupting the evaporation curve at various U. We also apply the above all-optical approach to evaporate atoms in a single-beam ODT. A similar result can also be achieved in the single-beam ODT as long as its beam waist is smaller than 16 μm to provide a high enough collision rate. The resulted number of condensed atoms in the single-beam ODT, however, is four times smaller than that in the crossed ODT.

5.4 Spin-mixing dynamics in a sodium spinor BEC

The interesting interactions in spinor BECs are interconversion among multiple spin states and magnetic field interactions characterized by the quadratic Zeeman effect. Such a system can be described with a simple two-dimensional phase space that we can manipulate to some degree by changing the magnetic field strength or the density of the BEC [55, 65]. We experimentally study spin-mixing dynamics in a F=1 sodium spinor condensate starting from a nonequilibrium initial state, as a result of antiferromagnetic spin-dependent interactions and the quadratic Zeeman energy induced by magnetic fields. When a F=1 spinor BEC is taken out of equilibrium at a non-zero magnetic field, we observe spin population oscillations resulted from coherent

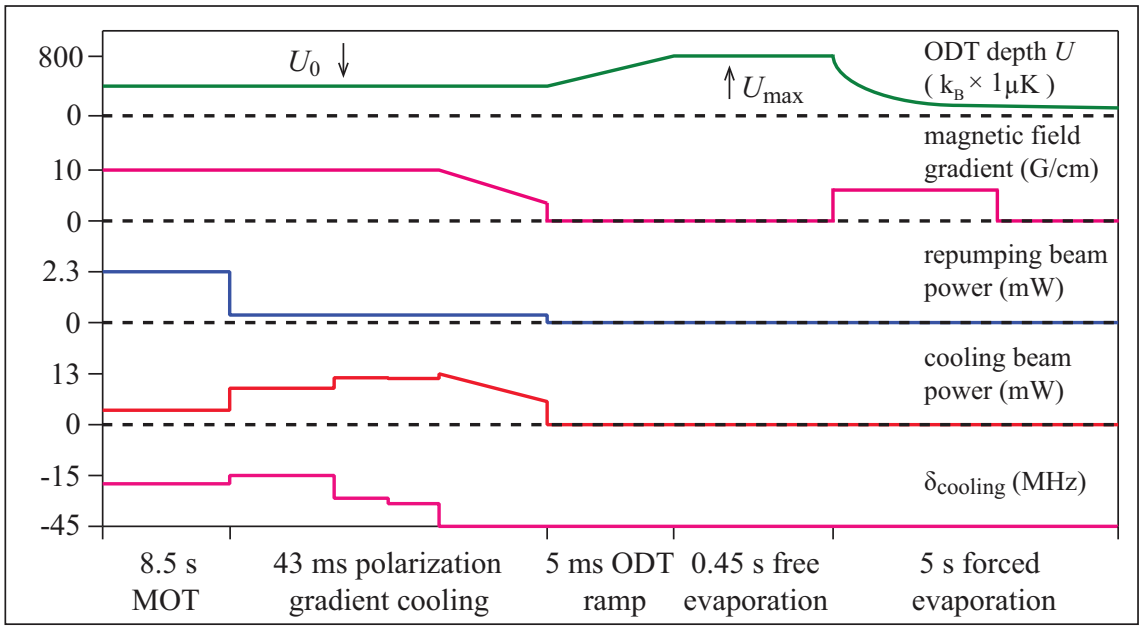

Figure 5.7: Experimental sequence of creating sodium BECs with the all-optical approach. Each MOT cooling beam is detuned by $\delta_{cooling}$ from the cycling transition. All axes are not to scale.

collisional interconversion among two $|F=1, m_F=0\rangle$ atoms, one $|F=1, m_F=+1\rangle$ atom, and one $|F=1, m_F=-1\rangle$ atom, as shown in Fig. 5.9(b).

Similar to Ref. [55, 118], we take into account the conservation of m and the total atom number. The SMA (single spatial-mode approximation) assumes all spin states share the same spatial wavefunction, which has been a successful model to understand spinor microcondensates [58, 64, 65, 66, 67, 68, 118, 119, 120]. The fractional population ρ_{m_F} and the phase θ_{m_F} of each m_F state are thus independent of position in SMA, and $m = \rho_{+1} - \rho_{-1}$. Spin-mixing dynamics in a F=1 spinor BEC can thus be described with a two-dimensional (ρ_0 vs θ) phase space. The BEC energy E and the time evolution of ρ_0 and θ may be expressed as [55, 118]

$$E = q_B(1-\rho_0) + c\rho_0[(1-\rho_0) + \sqrt{(1-\rho_0)^2 - m^2}\cos\theta],$$
$$\dot{\rho_0} = -(2/\hbar)\partial E/\partial\theta, \quad \dot{\theta} = (2/\hbar)\partial E/\partial\rho_0 \ . \tag{5.5}$$

Here q_B is the quadratic Zeeman energy shift, $\theta = \theta_{+1} + \theta_{-1} - 2\theta_0$ is the relative phase

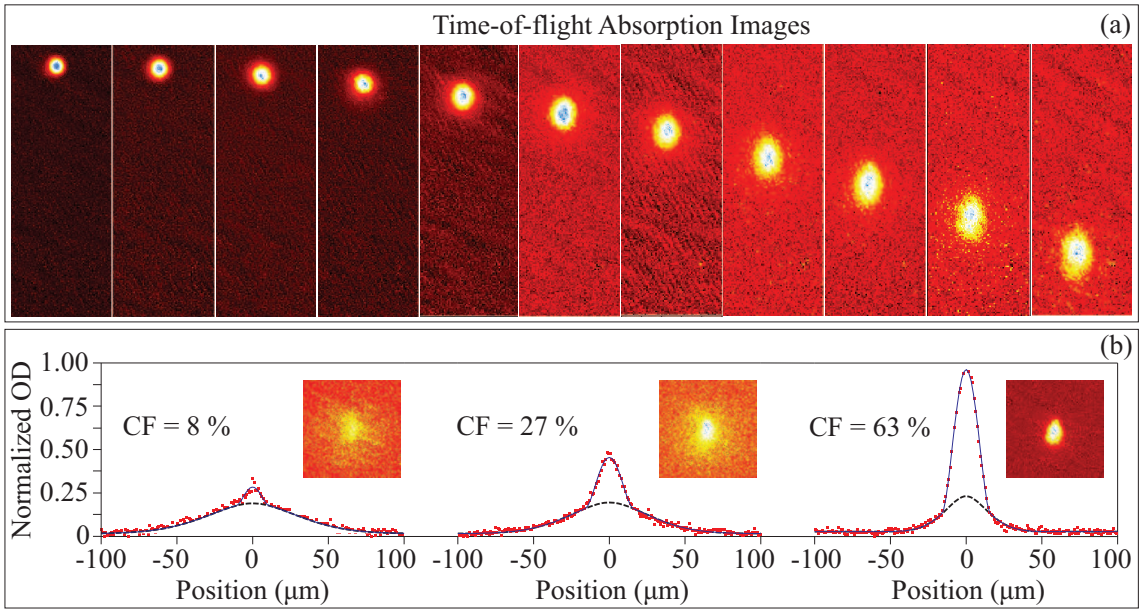

Figure 5.8: (a) Absorption images taken after a same evaporation curve and various lengths of TOF, 0 to 10 ms with a 1 ms step from the leftmost panel to the rightmost panel. (b) Absorption images taken after interrupting an optimized evaporation curve at various U followed by a 10 ms time-of-flight. OD stands for the optical density. Dashed black lines and solid blue lines are fits to the column densities based on a Gaussian distribution and a bimodal distribution, respectively. $\mathrm{CF} = \widetilde{\mathrm{n}}_{\mathrm{c}}/(\widetilde{\mathrm{n}}_{\mathrm{th}} + \widetilde{\mathrm{n}}_{\mathrm{c}})$, where $\widetilde{\mathrm{n}}_{\mathrm{th}}$ and $\widetilde{\mathrm{n}}_{\mathrm{c}}$ are column densities for the thermal cloud and the condensate, respectively.

among the three $m_{\rm F}$ spin states, and $\hbar$ is the reduced Planck constant. The induced linear Zeeman shift remains the same during the collisional spin interconversion and is thus ignored. The spin-dependent interaction energy is $c = c_2\langle n\rangle$, where $\langle n\rangle$ is the mean BEC density and c_2 is the spin dependent interaction coefficient. The total magnetization is $m = \rho_{+1} - \rho_{-1}$. It is well known that $q_B \propto B^2 > 0$, and $c_2 > 0$ (or $c_2 < 0$) in F=1 ^{23}Na (or ^{87}Rb) spinor BECs. Spin-dynamics in F=1 antiferromagnetic and ferromagnetic spinor BECs have been studied in magnetic fields where $q_{\rm B} > 0$ with ^{23}Na and ^{87}Rb atoms, respectively [55].

To fully polarize atoms in a F=1 BEC to the $|F = 1, m_F = 1\rangle$ state, a weak magnetic field gradient is applied during forced evaporation, as shown in Fig. 5.7. We then ramp up a magnetic bias field with its strength B between 100 mG and 700 mG after turning off the field gradient. We can prepare an initial state with any desired combination of three m_F states by altering the amplitude and duration of a resonant rf-pulse and/or a resonant microwave pulse at the end of the forced evaporation. A Stern-Gerlach separation followed by absorption imaging is used to measure the populations of different spin states, as shown Fig. 5.9(a).

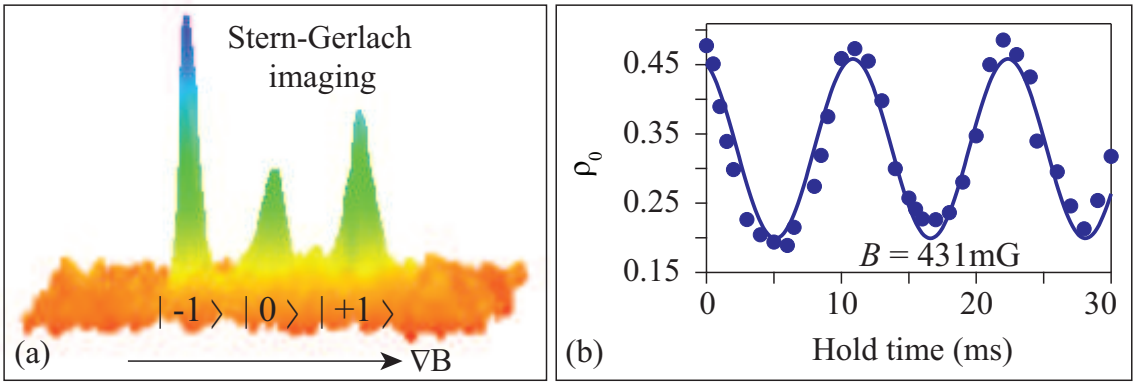

Figure 5.9: (a) Three spin components of a F=1 spinor BEC are spatially separated in a 3D Stern-Gerlach absorption image. (b) A typical time evolution of ρ_0 at B = 431 mG, $m = 0$, and $\theta = 0$ when the spinor BEC is held in the crossed ODT. The solid blue line is a sinusoidal fit to the data.

The time evolution of ρ_0 is fit by a sinusoid to extract the spin oscillation period T and amplitude A at a given B. The value of T as a function of B is plotted in Fig. 5.10 for $m = 0$. The spin oscillation is harmonic except near the critical values (i.e., $B = 370$ mG) where the period diverges. The energy contour $E_{\rm sep}$ where the oscillation becomes anharmonic is defined as a separatrix in phase space, as shown in the inset of Fig. 5.10. A point on the separatrix satisfies the equation $\dot{\rho_0} = \dot{\theta} = 0$ according to the mean-field SMA theory. In fact for our sodium system with $c > 0$, $E_{\rm sep} = q_{\rm B}$. The period T decreases rapidly with increasing B when B is large, which corresponds to the "Zeeman regime" with running phase solutions. In the opposite limit, the period only weakly depends on B, which represents the "interaction regime" with oscillatory phase solutions. The value of θ is (or is not) restricted in the regions with oscillatory (or running) phase solutions. The data can be well fit by a prediction derived from Eq. (5.5) (solid black line in Fig. 5.10) [55] with only one fitting parameter (i.e., the mean BEC density). Figure 5.10 may thus be a good way to measure the mean BEC density and to check the values of the crossed ODT's trap frequency and trap depth.

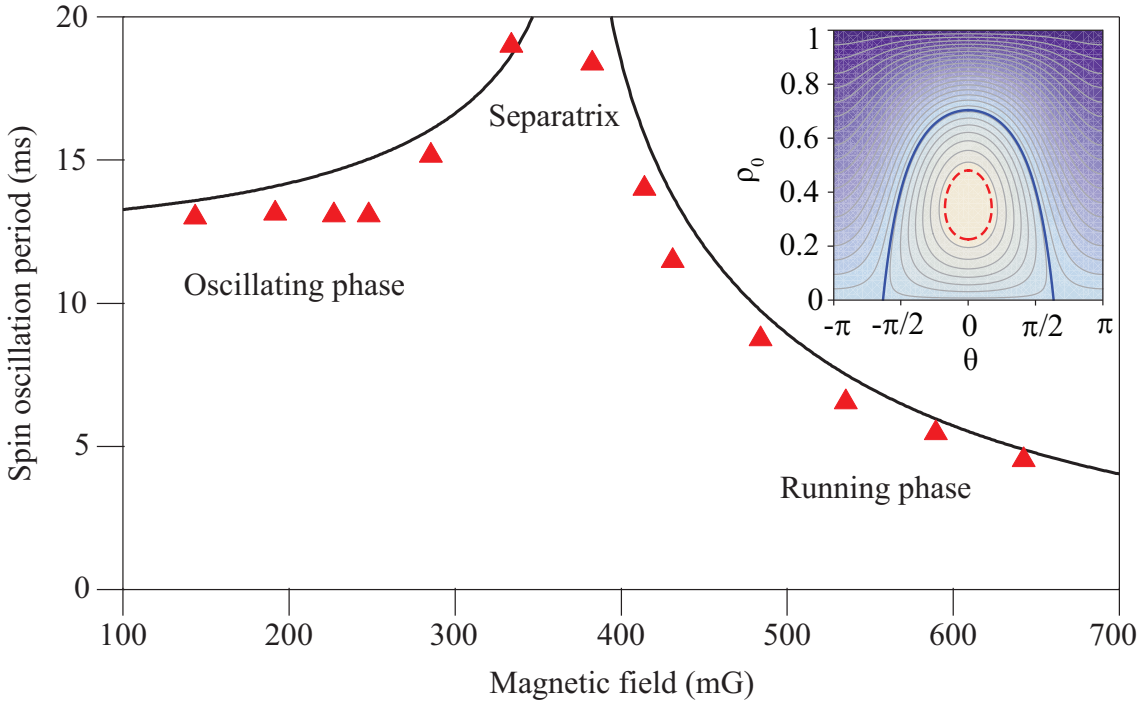

Figure 5.10: The period of spin population oscillations as a function of B at $m = 0$. The solid black line is a fit based on Eq. (5.5) with $m = 0$, $\rho_0|_{t=0} = 0.48$, $\theta|_{t=0} = 0$, and $c/h = 38$ Hz. Inset: Equal-energy contour plots generated from Eq. (5.5) at $B = 285$ mG when $m = 0$ and $c/h = 38$ Hz. Dashed red line represents the energy of atoms with $\rho_0|_{t=0} = 0.48$ and $\theta|_{t=0} = 0$. Heavy blue line represents the energy of the separatrix (E_{sep}) between oscillating and running phase solutions. Darker colors represent lower energies.

CHAPTER 6

Mapping the phase diagram of spinor condensates via adiabatic quantum phase transitions

This chapter presents our experimental results on the phase diagram of $F=1$ sodium antiferromagnetic spinor condensates. We developed a novel technique which enabled us to map the phase diagram by adiabatically tuning a microwave field across one of the quantum phase transitions observed in our system. Two papers related to these topics were published:

- J. Jiang, L. Zhao, M. Webb, and Y. Liu, *Mapping the phase diagram of spinor condensates via adiabatic quantum phase transitions*, Phys. Rev. A **90**, 023610 (2014).

- L. Zhao, J. Jiang, T. Tang, M. Webb, and Y. Liu, *Dynamics in spinor condensates tuned by a microwave dressing field*, Phys. Rev. A **89**, 023608 (2014).

Several groups demonstrated the mean-field (MF) ground states of spinor BECs by holding BECs in a fixed magnetic field and letting spin population oscillations damp out over a few seconds [64, 65, 66, 67]. The required damping time, determined by energy dissipation, may in some cases exceed the BEC lifetime. The exact mechanism involved in energy dissipation requires further study, although it has been shown that energy dissipates much faster in high magnetic fields [66]. For F=1 BECs, a magnetic field introduces only a positive net quadratic Zeeman energy $q_{\rm net}$, while a microwave field has a distinct advantage since it can induce both positive and negative $q_{\rm net}$ [55, 57, 58, 63, 121]. As shown in Ref. [58], the same physics model explains spin-

mixing dynamics observed in both microwave fields and magnetic fields. One would assume that, if given a long enough exposure to a microwave field, a spinor BEC could also reach its MF ground states. However, experimental studies on ground states of spinor BECs in microwave fields have proven to be very difficult, since these fields are created by near-resonant microwave pulses. Two major experimental challenges associated with microwave fields are atom losses and variations in magnetization m. A different inelastic collision rate in each hyperfine state may be one of possible reasons to account for these challenges. Microwave-induced changes in both m and the atom number N can be detrimental, especially when a spinor BEC is exposed to a large microwave field for a prolonged time [58, 63]. As a result, the phase diagram of F=1 BECs has not been well explored in the $q_{\rm net} \leq 0$ region, where applying microwave fields may be necessary.

In this chapter, I demonstrate a new method to overcome the aforementioned experimental challenges and report the observation of two types of quantum phase transitions in a spinor BEC [122]. In this method, we quickly prepare an initial equilibrium state at a very high magnetic field to minimize the damping time for spin population oscillations and prevent unnecessary exposure to microwave pulses. Equilibrium states at a desired $q_{\rm net}$ are then created by adiabatically sweeping an additional microwave field. Using this method, we are able to investigate many previously unexplored regions in the phase diagram of antiferromagnetic spinor BECs and observe three distinct quantum phases.

6.1 The mean-field ground states of spinor BECs

Similarly to Ref. [55, 56, 67], we define three phases in the MF ground states based on ρ_0, the fractional population of the $|F = 1, m_F = 0\rangle$ state: $\rho_0 = 1$, $\rho_0 = 0$, and $0 < \rho_0 < 1$ respectively represent a longitudinal polar phase, an antiferromagnetic (AFM) phase, and a broken-axisymmetry (BA) phase.

After taking into account that N and m are independent of time t and neglecting all constant terms in the Hamiltonian of spinor BECs, we use the SMA to express the BEC energy E and the time evolution of ρ_0 and θ as [55, 118, 119]

$$E(t) = c\rho_0(t)\{[1-\rho_0(t)] + \sqrt{[1-\rho_0(t)]^2 - m^2}\cos[\theta(t)]\} + q_{\rm net}(t)[1-\rho_0(t)] \; ; \tag{6.1}$$

$$\dot{\rho_0} = -\frac{4\pi}{h}\frac{\partial E(t)}{\partial\theta(t)}, \quad \dot{\theta} = \frac{4\pi}{h}\frac{\partial E(t)}{\partial\rho_0(t)} \; . \tag{6.2}$$

Here $q_{\rm net} = q_M + q_B$ is the net quadratic Zeeman energy with q_B (or q_M) being induced by magnetic (or microwave dressing) fields.

By minimizing Eq. (6.1), we find ρ_0 in a MF ground state of F=1 spinor BECs is zero if $q_{\rm net} < {\rm c}(1 \pm \sqrt{1-{\rm m}^2})$; or equals to one if $m = 0$ and $q_{\rm net} > -c(1 \pm 1)$; or is the root of the following equation at all other $q_{\rm net}$ and m,

$$c[1 - 2\rho_0 \pm \frac{(1-2\rho_0)(1-\rho_0) - m^2}{\sqrt{(1-\rho_0)^2 - m^2}}] - q_{\rm net} = 0 \; , \tag{6.3}$$

where the + (or −) sign applies to ferromagnetic (or antiferromagnetic) spinor BECs.

6.2 Two experimental sequences to generate equilibrium states in spinor BECs

The experimental setup is similar to that elaborated in previous chapters and our recent publications [58, 62]. A F=1 BEC of 5×10^4 atoms is created by a forced evaporation in a crossed optical dipole trap. To fully polarize atoms into the $|F = 1, m_F = -1\rangle$ state, we turn on a weak magnetic field gradient and a low magnetic bias field in the forced evaporative cooling process. A resonant rf-pulse of a proper amplitude and duration is applied to prepare an initial state with any desired combination of the three m_F states. This moment is defined as the starting point ($t = 0$) of our experimental sequences, as shown in Fig. 6.2. Every sequence ends at $t = t_f$. Populations of multiple spin states are then measured by a standard Stern-Gerlach absorption imaging.

6.2.1 An old and widely-used method to generate equilibrium states

We use two different methods to generate equilibrium states. The Method-O is an old and widely-used method, which creates equilibrium states simply by holding a BEC at a fixed $q_{\rm net}$ for a sufficiently long time. We find that the required hold time is longer than 2 s for all positive $q_{\rm net}$ studied in this paper. This old method fails for our system in low magnetic fields (i.e, the small positive $q_{\rm net}$ region), because energy dissipates very slowly and the required hold time is longer than the BEC lifetime ($\sim$ 10 s) in this region. This old method is more problematic in the negative $q_{\rm net}$ region, because it leads to significant atom losses and detrimental changes in m. The BEC lifetime decreases with the absolute value of q_M, the quadratic Zeeman energy induced by a microwave field. Figure 6.1 shows a numerical example: the measured BEC lifetime in our system reduces from 9 s to 2.2 s when $|q_M|/h$ increases from 1 Hz to 25 Hz. Here h is the Planck constant. Changes in m and N become detrimental when a BEC is exposed to a big $|q_M|$ for a prolonged time. This experimental challenge is one main reason why the phase diagram in the negative $q_{\rm net}$ region had remained to be largely unexplored, since the old method requires holding a BEC at a fixed $q_{\rm net}$ for a few seconds.

6.2.2 Our new method to generate equilibrium states

In order to overcome these experimental challenges associated with the old method, we have developed a new method, Method-N. A typical experimental sequence of the new method is listed in Fig. 6.2. We first hold a spinor BEC in the optical trap for 5 s at a very high magnetic field with $q_B/h = 900$ Hz. This step ensures the BEC reaches its ground states, since we and Ref. [66] find that the energy dissipation rate quickly increases with q_B. Second, we adiabatically ramp the magnetic field down to $q_B/h = 20$ Hz in 0.1 s, keep q_B at this value for 0.3 s, and then turn on a far off-resonant microwave pulse in 0.1 s. Third, we tune only the frequency of this pulse

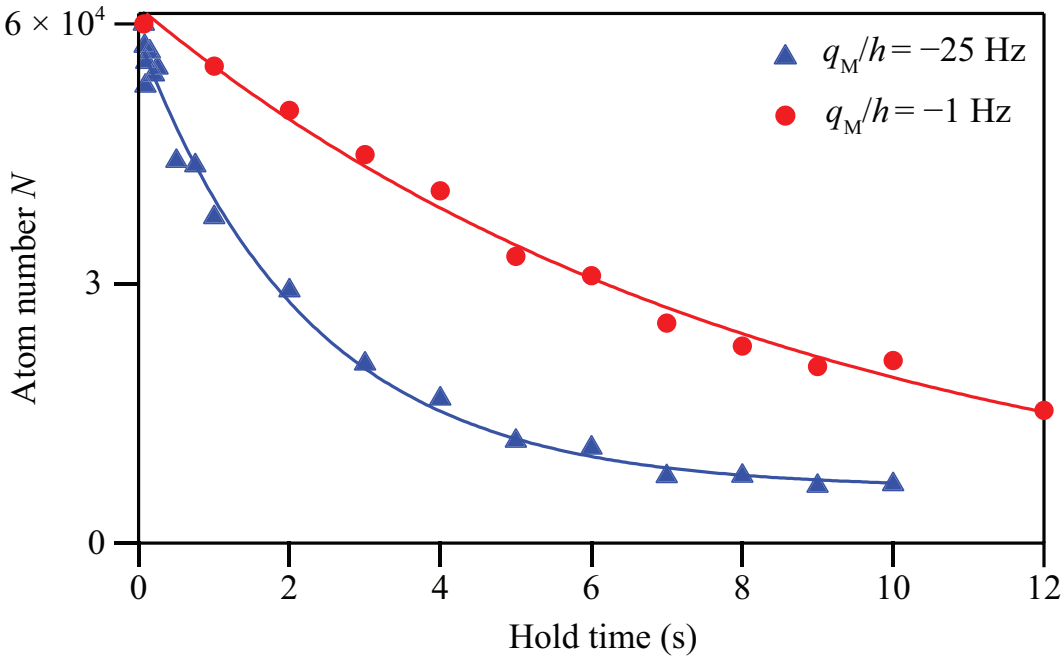

Figure 6.1: Time evolution of N at two different q_M. Solid lines are exponential fits to yield the BEC lifetime (i.e., 2.2 s at $q_M/h = -25$ Hz and 9 s at $q_M/h = -1$ Hz).

slowly within 0.5 s, in order to adiabatically sweep its corresponding microwave field to a desired $q_{\rm net}$. Our approach to characterize microwave dressing fields and the frequency tuning curve for adiabatically sweeping $q_{\rm net}$ within the range of $-\infty$ to $+\infty$ are as same as those illustrated in our previous work [58].

6.2.3 Comparisons between the old and new methods

A comparison of these two methods starting from the same initial state is shown in Fig. 6.3, which highlights the advantage of our new method. Note that m and N may not be conserved using the old method, when a microwave field induced by a near-resonant microwave pulse is applied. This is due to the fact that the microwave pulse unavoidably excites some atoms in a F=1 spinor BEC to the F=2 manifold, and more atoms are excited when the microwave pulse has a higher power or a smaller frequency detuning with respect to the $|F = 1\rangle \leftrightarrow |F = 2\rangle$ transitions.

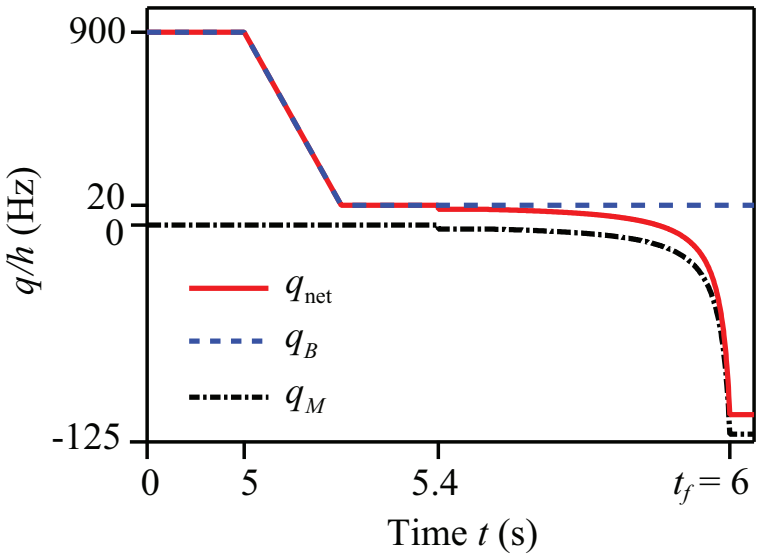

Figure 6.2: A typical experimental sequence of Method-N, which is our new method to create equilibrium states via adiabatically sweeping a microwave field. In this paper -150 Hz $\leq q_{\rm net}(t = t_f)/h \leq 150$ Hz. All axes are not to scale.

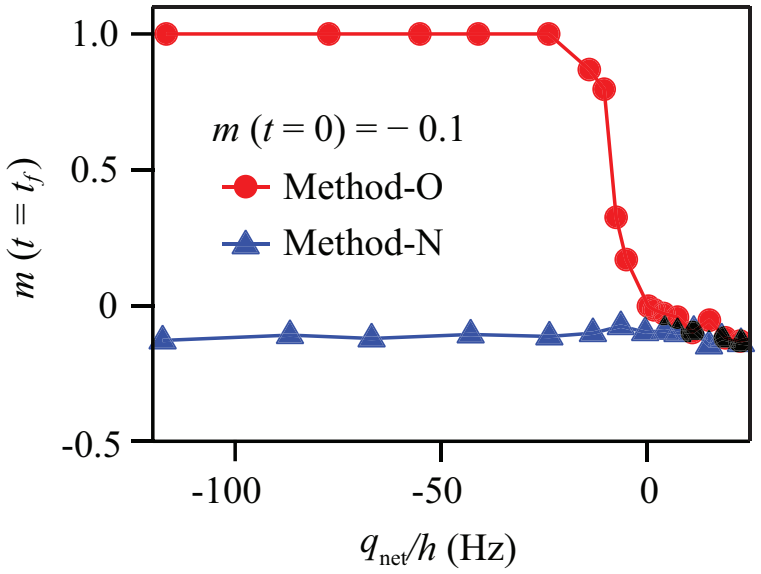

Figure 6.3: m as a function of $q_{\rm net}$ at $t = t_f$ in the two methods starting from the same initial state, i.e., $m(t = 0) = -0.1$. Note that t_f for Method-O in this panel is only 1 s, which is much shorter than the typical hold time for creating equilibrium states.

6.3 Adiabaticity check of our new method

In theory, once a BEC is prepared into its ground state, the BEC may stay in its ground state at each $q_{\rm net}$ when a microwave field is adiabatically ramped [59]. We can thus initially check whether the new method is applicable by comparing equilibrium states created by both new and old methods in a region, $q_{\rm net} \gg 0$, where the old method has been proven to generate the MF ground states [64, 65, 66, 67]. Figure 6.4 shows such comparisons made at $q_{\rm net}(t = t_f)/h = 100$ Hz for various magnetization m. The equilibrium states created by the two methods appear to be quite similar, and they stay very close to the same black solid line which represents the MF ground states in Fig. 6.4. This suggests that our new method is adiabatic enough to replace the old method in studies related to the BEC phase diagrams. We also find that a spinor BEC returns to its original state when we ramp a microwave field from $q_M = 0$ to a fixed nonzero q_M and then back to $q_M = 0$ with this new method, although this observation may not be sufficient to prove the process is adiabatic.

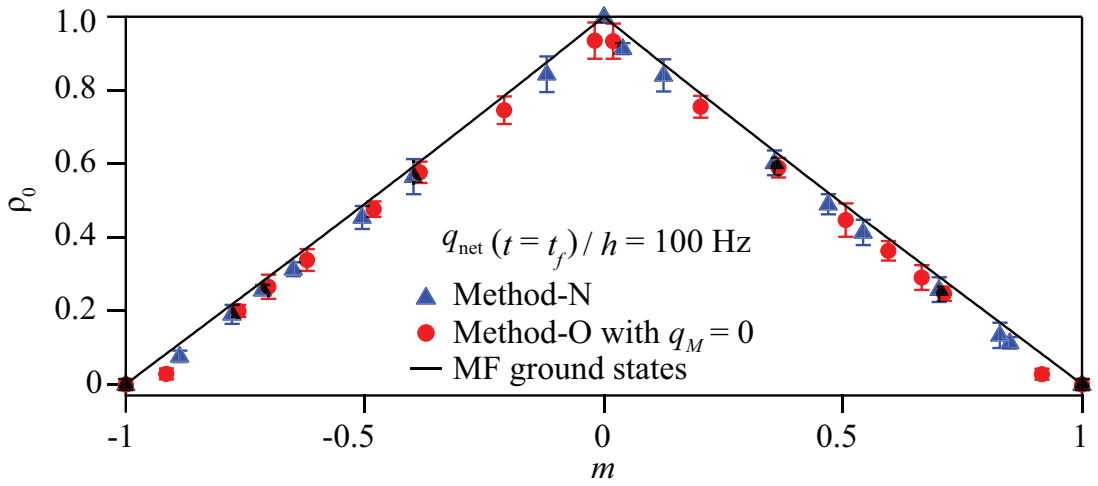

Figure 6.4: ρ_0 as a function of m at $q_{\rm net}(t = t_f)/h = 100$ Hz in equilibrium states created by the two methods. In this panel, Method-O prepares equilibrium states by holding BECs for 8 s in a high magnetic field where $q_M = 0$ and $q_B/h = 100$ Hz. The solid black line represents the MF ground states.

6.4 Mapping the phase diagram of spinor condensates

We then apply our new method to a much wider range of $q_{\rm net}$ and m, especially in the negative and small positive $q_{\rm net}$ regions which cannot be easily explored by the old method, as shown in Fig. 6.5. We find two interesting results from this figure. First, our data in Fig. 6.5(a) show a quantum phase transition between a BA phase and an AFM phase at each m. This BA-AFM phase transition appears to occur at a larger $q_{\rm net}$ when $|m|$ gets bigger, which can be well explained by the MF theory (i.e., dashed lines in the inset in Fig. 6.5(a)). Another interesting result is that this new method does allow us to access many previously unexplored regions in the phase diagram, although there is a visible discrepancy between the MF ground states and our data at a small m in the negative $q_{\rm net}$ region, as shown in Fig. 6.5(b). To understand this phenomenon, we simulate the experimental processes based on Eq. (6.2) by taking a proper formula to account for the time evolution of $q_{\rm net}$ during an adiabatic ramping of microwave fields. Figure 6.5 shows that the simulation results can well resemble the experimental data, while the differences between our simulation results and the MF ground states are emphasized by a shaded area at each m in the two insets in Fig. 6.5. These shaded areas appear to slowly increase in the negative $q_{\rm net}$ region when $|m|$ approaches zero. In other words, the discrepancy between our data and the MF ground states only becomes noticeable at a small $|m|$ in the negative $q_{\rm net}$ region. Due to this discrepancy, we find that the predicted quantum phase transition between an AFM phase and a longitudinal polar phase at $m = 0$ and $q_{\rm net} = 0$ is replaced by a transition between a BA phase and a longitudinal polar phase. Since our experimental resolution for ρ_0 is around 0.02, Fig. 6.5 implies that our new method is sufficient to map out the BEC phase diagram in the positive $q_{\rm net}$ region at each m, and in the negative $q_{\rm net}$ as long as $|m| \geq 0.4$.

Figure 6.6 clearly summarizes the improvement provided by this new method, after comparing the theoretical MF phase diagram to an experimental phase diagram

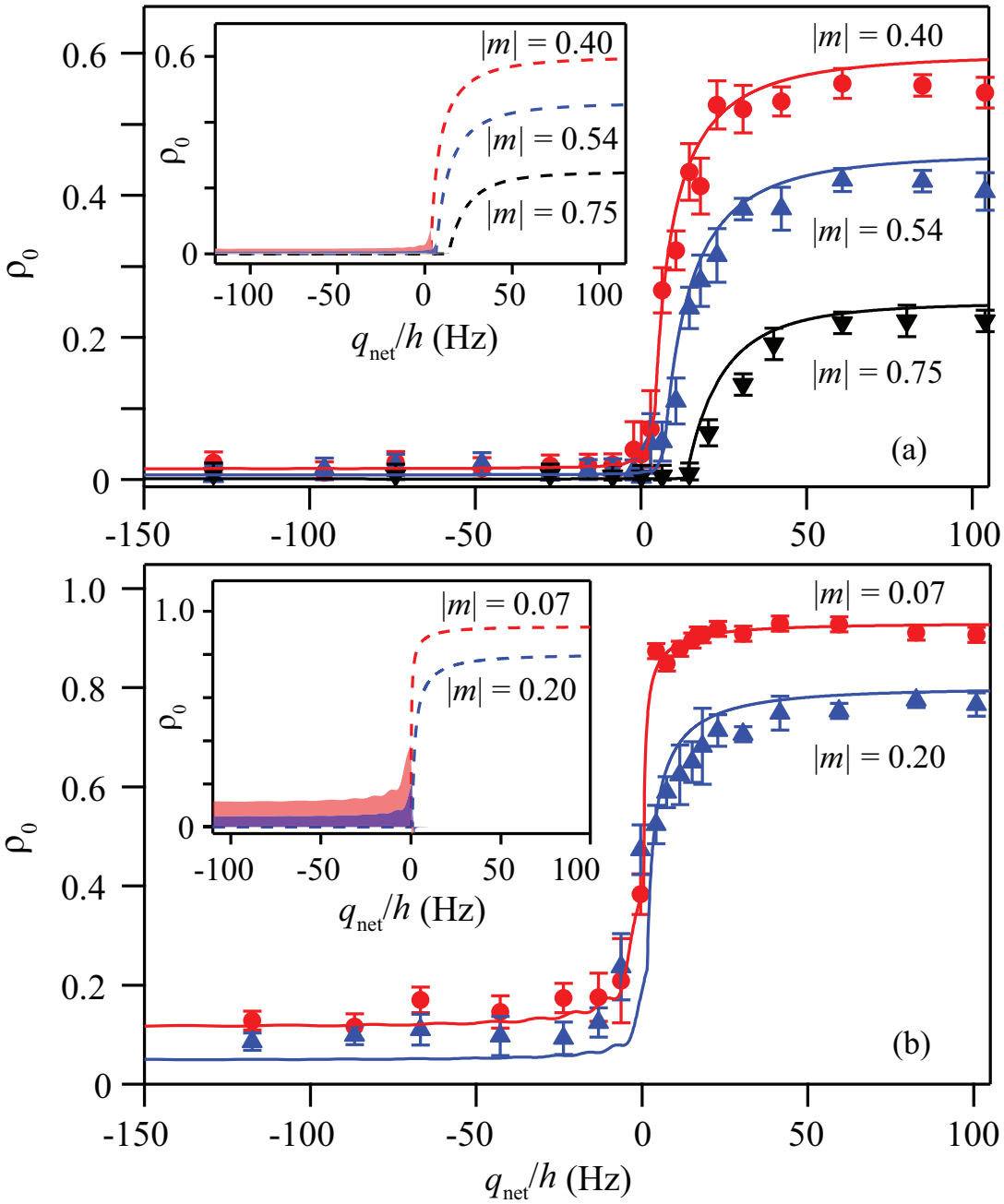

Figure 6.5: ρ_0 as a function of $q_{\rm net}$ at $t = t_f$ for three large $|m|$ in Panel (a) and for two small $|m|$ in Panel (b) in equilibrium states created by our new method. Solid lines are simulation results for the experimental processes based on Eq. (6.2). Insets: dashed lines are the MF ground states. Shaded areas represent the differences between our simulation results and the MF theory at various m. The black, blue, and red colors in Panel (a) respectively correspond to results at $|m| = 0.75$, 0.54, and 0.40. The blue and red colors in Panel (b) represent results at $|m| = 0.20$ and 0.07.

consisting of our data taken at 153 different $q_{\rm net}$ and m. All three predicted phases (i.e., an AFM, a polar, and a BA phases), an AFM-BA phase transition at a fixed m, and a transition between a longitudinal polar phase and a BA phase at a certain positive $q_{\rm net}$ are shown in the experimental phase diagram. Good agreements between our data and the MF ground states can be found everywhere in the two phase diagrams except in the region where $|m| < 0.4$ and $q_{\rm net} < 0$. This problematic region has been marked by red solid lines in Fig. 6.6. Ramping microwave fields at a slower rate should help to diminish this problematic region, however, a slower rate requires holding a BEC in microwave fields for a longer time and thus inevitably leads to more atom losses and a bigger change in m. In fact, we tried quite a few different microwave ramping rates, but none of them enabled a spinor BEC to reach its MF ground states when m is very small and $q_{\rm net} < 0$. The same problem also exists in simulation results: our simulation program cannot suggest a reasonable ramping rate to ensure an adiabatic sweep of $q_{\rm net}$ across a phase transition for a small m.

6.5 Feasibility of our new method

To understand the feasibility of Method-N, we need to find the exact value of ΔE, the energy gap between the ground state and the first excited state in spinor BECs. Similarly to Ref. [59], we can describe a spinor BEC in the Fock space. The spin-dependent part of the Hamiltonian in a F=1 spinor BEC can be expressed as [59, 118, 123]

$$H = \sum_{i,j,k,l=-1}^{1} \left[q_{\rm net} k^2 a_k^\dagger a_k + \frac{c}{2} \sum_\gamma a_k^\dagger a_i^\dagger (F_\gamma)_{ij} (F_\gamma)_{kl} a_j a_l \right], \tag{6.4}$$

since m is conserved and there are only a finite number of atoms in a typical equilibrium state studied in this paper. Here a_k ($a_k^\dagger$) is the annihilation (creation) operator of the $|F = 1, m_F = k\rangle$ state, and $F_{\gamma=x,y,z}$ are the spin-1 matrices. By diagonalizing the Hamiltonian in Eq. (6.4) and performing an exact numerical many-body calculation, we can find the energy gaps. Figure 6.7 shows numerical examples of ΔE

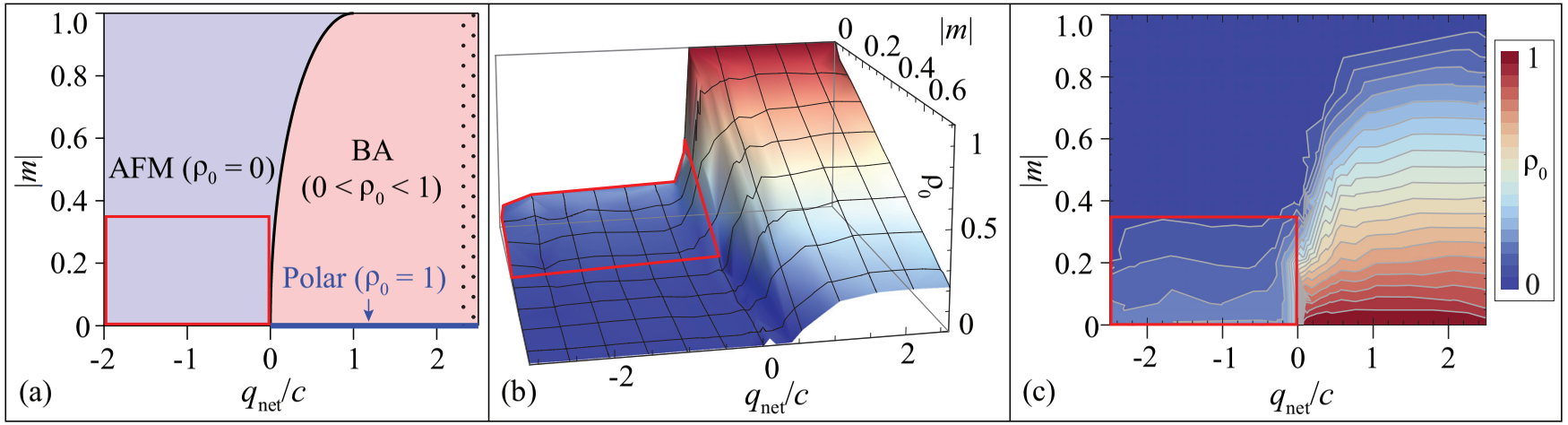

Figure 6.6: (a). The MF phase diagram of spin-1 antiferromagnetic spinor BECs based on Eqs. (6.1-6.3). Our new method works everywhere except in the area marked by red solid lines, while Method-O only applies to the area filled with dots at large $q_{\rm net}$. Panel (b) (or (c)) is a 3D (or a contour) plot of the experimental phase diagram consisting of data taken by our new method at 153 different $q_{\rm net}$ and m. Red solid lines in Panels (b)-(c) mark the region where our data are different from the MF ground states.

at three typical $|m|$. It appears that ΔE drastically drops by more than three orders of magnitude when $|m|$ and $q_{\rm net}$ approach zero, as shown in the inset in Fig. 6.7. Therefore, it is not surprising that adiabatically sweeping $q_{\rm net}$ across a quantum phase transition point is not feasible at a very small m, especially at $m = 0$. We can also calculate ΔE_e, the energy gap between the highest eigenstate and the second highest eigenstate of Eq. (6.4). The minimal value of ΔE_e at $m = 0$ appears to be larger than that of ΔE (the energy gap associated with the ground state) at $m = 0.75$. In other words, adiabatically sweeping $q_{\rm net}$ across a quantum phase transition demonstrated in this paper may be useful for confirming other important predictions, for instance, realizing massive entanglement in the highest eigenstate of antiferromagnetic spinor BECs [59]. In addition, this method can be applied to other atomic species and may be helpful to discover interesting quantum phase transitions in other systems, for example, revealing a BA-AFM quantum phase transition in F=1 ^{87}Rb spinor BECs at a negative $q_{\rm net}$.

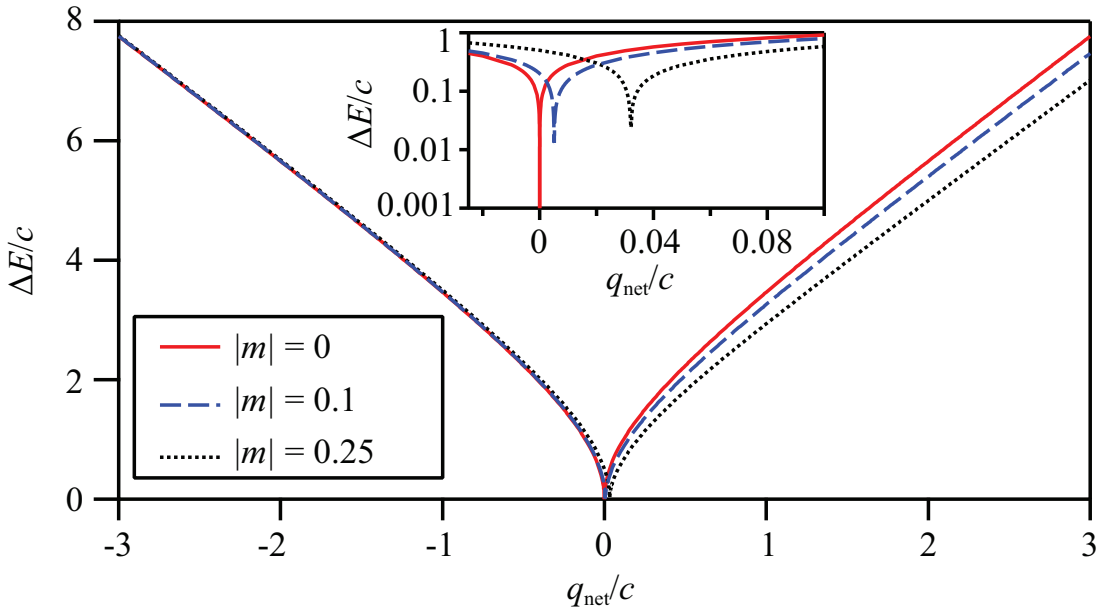

Figure 6.7: ρ_0 as a function of $q_{\rm net}$ at $t = t_f$ for three large $|m|$ in Panel (a) and for two small $|m|$ in Panel (b) in equilibrium states created by our new method. Solid lines are simulation results for the experimental processes based on Eq. (6.2). Insets: dashed lines are the MF ground states. Shaded areas represent the differences between our simulation results and the MF theory at various m. The black, blue, and red colors in Panel (a) respectively correspond to results at $|m| = 0.75$, 0.54, and 0.40. The blue and red colors in Panel (b) represent results at $|m| = 0.20$ and 0.07, respectively.

CHAPTER 7

CONCLUSIONS

7.1 Final remarks

This is the last chapter of my thesis and also indicates the endpoint of my PhD study. At this point, many unforgettable moments during the past six years came into my mind and they have became precious parts of my memory. I still remember the first time I walked into the lab and there was just two empty optical tables and I was curious at that time what a working system should look like. I also remember our first sodium MOT, which was a very tiny yellow dot. I was staring at the atomic cloud and even did not believe it with my eyes. After our 3-year hard work, we finally achieved our sodium spinor BECs in 2013. Our robust experimental system can routinely provide us a BEC of $\sim 10^5$ sodium atoms in our daily experiments.

The major parts of this thesis are the all-optical production of a sodium spinor BEC, and our experimental studies on the spin-mixing dynamics in spinor BECs. Various important apparatuses and technologies for generating a sodium spinor condensate have been described in details in this thesis. A simple and optimal experimental scheme that can greatly boost the atom number of a BEC was also demonstrated. We also discussed an upper limit for the evaporative cooling efficiency in all-optical BEC approaches. Spin population oscillations have been observed in sodium spinor BECs, which have been well explained by the SMA theory. In addition, we have introduced a new experimental method to map out the phase diagram of sodium spinor condensates via adiabatically tuning a microwave field across one of the quantum phase transitions observed in our system. Compared to one widely used method that

requires holding BECs in an ODT for a long time, our method overcame two major experimental challenges. As a result, many previously unexplored regions in the phase diagram of F=1 antiferromagnetic spinor condensates have been investigated by our new method, and our experimental phase diagrams agree well with the mean-field theory.

7.2 Future direction

Spinor BECs in optical lattices can systematically study, verify and optimize condensed matter models. For example, they provide a quantum simulator to study the nature of entanglement of many-body wavefunctions, e.g., the Laughlin-type wavefunctions appearing in the fractional quantum Hall systems. A better understanding of these models may directly lead to engineering revolutionary materials, which could enable development of new generations of devices for high speed precision electronics and telecommunications equipment. Dynamics of lattice-trapped spinor BECs have been recently studied in both ^{87}Rb [124, 125, 126, 127] and ^{23}Na [128] spinor gases.

The Bose-Hubbard model which includes spin-dependent interactions will be applied to understand our system: sodium spinor BECs confined in 3D optical lattices. We define U_0 as the spin-independent on-site atom-atom interaction energy, J as the tunneling energy, and U_2 as the spin-dependent atom-atom interaction energy. U_2 is proportional to c_2, so it is positive (or negative) in F=1 Na (or Rb) BECs. Atoms held in a shallow optical lattice can tunnel freely from site to site and form a superfluid phase. As the lattice is made deeper, the atomic interaction is increased while the tunneling rate between lattice sites is exponentially suppressed. A scalar BEC system then undergoes a second-order transition from the superfluid (SF) phase to the Mott-insulator (MI) phase [55]. Each lattice site contains n_L (a definite fixed number) atoms in the MI phase. The critical point for the SF-MI phase transition is determined by $U_0/J = z[2n_L+1+2\sqrt{n_L(n_L+1)}]$, according to the mean-field theory

for homogenous systems of atoms in the lowest band of an optical lattice [129, 130]. Here z is the number of nearest neighbors in the lattice (e.g., z=6 for a 3D/cubic lattice). The SF-MI phase transition should also appear in lattice-trapped spinor BECs. However, the mean-field theory predicts that the transition is remarkably different in antiferromagnetic spinor BECs: the transition may be first order around the tip of each Mott lobe for an even occupation number n_L, while it is second order for an odd n_L [55]. 3D optical lattices formed by three optical standing waves, two in the horizontal plane and one in the vertical plane, have been constructed in our lab recently. We will perform a few studies related to quantum-phase-revival spectroscopy, the mean-field phase diagram, and the first-order superfluid to Mott-insulator transitions in the near future.

REFERENCES

[1] Pyotr Kapitsa. Viscosity of liquid helium below the λ-point. *Nature*, 141:74, 1938.

[2] John F. Allen and Don Misener. Flow phenomena in liquid helium ii. *Nature*, 142:643, 1938.

[3] F. London. The λ phenomenon of liquid helium and the bose-einstein degeneracy. *Nature*, 141:643, 1938.

[4] L. Tisza. Transport phenomenena in helium ii. *Nature*, 141:913, 1938.

[5] D. D. Osheroff, R. C. Richardson, and D. M. Lee. Evidence for a new phase of solid he^3. *Phys. Rev. Lett.*, 28:885–888, Apr 1972.

[6] D. D. Osheroff, W. J. Gully, R. C. Richardson, and D. M. Lee. New magnetic phenomena in liquid he^3 below 3 mk. *Phys. Rev. Lett.*, 29:920–923, Oct 1972.

[7] D. J. Wineland and H. Dehmelt. Proposed 10^{14} $\delta\nu < \nu$ laser fluorescence spectroscopy on Tl^+ mono-ion oscillator III. *Bull. Am. Phys. Soc.*, 20:637, 1975.

[8] T. W. Hänsch and A. L. Schawlow. Cooling of gases by laser radiation. *Optics Communications*, 13(1):68 – 69, 1975.

[9] D. J. Wineland, R. E. Drullinger, and F. L. Walls. Radiation-pressure cooling of bound resonant absorbers. *Phys. Rev. Lett.*, 40:1639–1642, Jun 1978.

[10] William D. Phillips and Harold Metcalf. Laser deceleration of an atomic beam. *Phys. Rev. Lett.*, 48:596–599, Mar 1982.

[11] Steven Chu, L. Hollberg, J. E. Bjorkholm, Alex Cable, and A. Ashkin. Three-dimensional viscous confinement and cooling of atoms by resonance radiation pressure. *Phys. Rev. Lett.*, 55:48–51, Jul 1985.

[12] E. L. Raab, M. Prentiss, Alex Cable, Steven Chu, and D. E. Pritchard. Trapping of neutral sodium atoms with radiation pressure. *Phys. Rev. Lett.*, 59:2631–2634, Dec 1987.

[13] J. Dalibard and C. Cohen-Tannoudji. Laser cooling below the doppler limit by polarization gradients: simple theoretical models. *J. Opt. Soc. Am. B*, 6(11):2023–2045, Nov 1989.

[14] P. J. Ungar, D. S. Weiss, E. Riis, and Steven Chu. Optical molasses and multilevel atoms: theory. *J. Opt. Soc. Am. B*, 6(11):2058–2071, Nov 1989.

[15] M. H. Anderson, J. R. Ensher, M. R. Matthews, C. E. Wieman, and E. A. Cornell. Observation of bose-einstein condensation in a dilute atomic vapor. *Science*, 269(5221):198–201, 1995.

[16] K. B. Davis, M. O. Mewes, M. R. Andrews, N. J. van Druten, D. S. Durfee, D. M. Kurn, and W. Ketterle. Bose-einstein condensation in a gas of sodium atoms. *Phys. Rev. Lett.*, 75:3969–3973, Nov 1995.

[17] C. C. Bradley, C. A. Sackett, J. J. Tollett, and R. G. Hulet. Evidence of bose-einstein condensation in an atomic gas with attractive interactions. *Phys. Rev. Lett.*, 75:1687–1690, Aug 1995.

[18] G. Modugno, G. Ferrari, G. Roati, R. J. Brecha, A. Simoni, and M. Inguscio. Bose-einstein condensation of potassium atoms by sympathetic cooling. *Science*, 294(5545):1320–1322, 2001.

[19] Tino Weber, Jens Herbig, Michael Mark, Hanns-Christoph Nägerl, and Rudolf Grimm. Bose-einstein condensation of cesium. *Science*, 299(5604):232–235, 2003.

[20] Yosuke Takasu, Kenichi Maki, Kaduki Komori, Tetsushi Takano, Kazuhito Honda, Mitsutaka Kumakura, Tsutomu Yabuzaki, and Yoshiro Takahashi. Spin-singlet bose-einstein condensation of two-electron atoms. *Phys. Rev. Lett.*, 91:040404, Jul 2003.

[21] Sebastian Kraft, Felix Vogt, Oliver Appel, Fritz Riehle, and Uwe Sterr. Bose-einstein condensation of alkaline earth atoms: ^{40}Ca. *Phys. Rev. Lett.*, 103:130401, Sep 2009.

[22] Simon Stellmer, Meng Khoon Tey, Bo Huang, Rudolf Grimm, and Florian Schreck. Bose-einstein condensation of strontium. *Phys. Rev. Lett.*, 103:200401, Nov 2009.

[23] Y. N. Martinez de Escobar, P. G. Mickelson, M. Yan, B. J. DeSalvo, S. B. Nagel, and T. C. Killian. Bose-einstein condensation of ^{84}Sr. *Phys. Rev. Lett.*, 103:200402, Nov 2009.

[24] B. DeMarco and D. S. Jin. Onset of fermi degeneracy in a trapped atomic gas. *Science*, 285(5434):1703–1706, 1999.

[25] M. W. Zwierlein, C. A. Stan, C. H. Schunck, S. M. F. Raupach, S. Gupta, Z. Hadzibabic, and W. Ketterle. Observation of bose-einstein condensation of molecules. *Phys. Rev. Lett.*, 91:250401, Dec 2003.

[26] S. Jochim, M. Bartenstein, A. Altmeyer, G. Hendl, S. Riedl, C. Chin, J. Hecker Denschlag, and R. Grimm. Bose-einstein condensation of molecules. *Science*, 302(5653):2101–2103, 2003.

[27] Markus Greiner, Cindy A. Regal, and Deborah S. Jin. Emergence of a molecular boseeinstein condensate from a fermi gas. *Nature*, 426:537–540, 2003.

[28] M. R. Matthews, B. P. Anderson, P. C. Haljan, D. S. Hall, C. E. Wieman, and E. A. Cornell. Vortices in a bose-einstein condensate. *Phys. Rev. Lett.*, 83:2498–2501, Sep 1999.

[29] J. R. Abo-Shaeer, C. Raman, J. M. Vogels, and W. Ketterle. Observation of vortex lattices in bose-einstein condensates. *Science*, 292(5516):476–479, 2001.

[30] Chad N. Weiler, Tyler W. Neely, David R. Scherer, Ashton S. Bradley, Matthew J. Davis, and Brian P. Anderson. Spontaneous vortices in the formation of bose-einstein condensatess. *Nature*, 455:948–951, 2008.

[31] S. Inouye, M. R. Andrews, J. Stenger, H.-J. Miesner, D. M. Stamper-Kurn, and W. Ketterle. Observation of feshbach resonances in a bose-einstein condensate. *Nature*, 392:151–154, 1998.

[32] Cheng Chin, Rudolf Grimm, Paul Julienne, and Eite Tiesinga. Feshbach resonances in ultracold gases. *Rev. Mod. Phys.*, 82:1225–1286, Apr 2010.

[33] M.-O. Mewes, M. R. Andrews, D. M. Kurn, D. S. Durfee, C. G. Townsend, and W. Ketterle. Output coupler for bose-einstein condensed atoms. *Phys. Rev. Lett.*, 78:582–585, Jan 1997.

[34] Simon Stellmer, Benjamin Pasquiou, Rudolf Grimm, and Florian Schreck. Laser cooling to quantum degeneracy. *Phys. Rev. Lett.*, 110:263003, Jun 2013.

[35] V. Bolpasi, N. K. Efremidis, M. J. Morrissey, P. C. Condylis, D. Sahagun, M. Baker, and W. V. Klitzing. An ultra-bright atom laser. *New Journal of Physics*, 16(3):033036, 2014.

[36] Nicholas P. Robins, Cristina Figl, Matthew Jeppesen, Graham R. Dennis, and John D. Close. A pumped atom laser. *Nature Physics*, 4:731–736, 2008.

[37] G. Rosi, F. Sorrentino, L. Cacciapuoti, M. Prevedelli, and G. M. Tino. Precision measurement of the newtonian gravitational constant using cold atoms. *Nature*, 510:518–521, 2014.

[38] Immanuel Bloch. Ultracold quantum gases in optical lattices. *Nature Physics*, 1:23–30, 2005.

[39] C. Becker, P. Soltan-Panahi, J. Kronjäger, S. Dörscher, K. Bongs, and K. Sengstock. Ultracold quantum gases in triangular optical lattices. *New Journal of Physics*, 12(6):065025, 2010.

[40] P. Soltan-Panahi, J. Struck, P. Hauke, A. Bick, W. Plenkers, G. Meineke, C. Becker, P. Windpassinger, M. Lewenstein, and K. Sengstock. Multi-component quantum gases in spin-dependent hexagonal lattices. *Nature Physics*, 7:434–440, 2011.

[41] Gyu-Boong Jo, Jennie Guzman, Claire K. Thomas, Pavan Hosur, Ashvin Vishwanath, and Dan M. Stamper-Kurn. Ultracold atoms in a tunable optical kagome lattice. *Phys. Rev. Lett.*, 108:045305, Jan 2012.

[42] Markus Greiner, Olaf Mandel, Tilman Esslinger, Theodor W. Hänsch, and Immanuel Bloch. Quantum phase transition from a superfluid to a mott insulator in a gas of ultracold atoms. *Nature*, 415:39–44, 2002.

[43] Toshiya Kinoshita, Trevor Wenger, and David S. Weiss. Observation of a one-dimensional tonks-girardeau gas. *Science*, 305(5687):1125–1128, 2004.

[44] B. Paredes, A. Widera, V. Murg, O. Mandel, S. Fölling, I. Cirac, G. V. Shlyapnikov, T. W. Hänsch, and I. Bloch. Tonks-girardeau gas of ultracold atoms in an optical lattice. *Nature*, 429:277–281, 2004.

[45] W. S. Bakr, A. Peng, M. E. Tai, R. Ma, J. Simon, J. I. Gillen, S. Föling, L. Pollet, and M. Greiner. Probing the superfluid-to-mott insulator transition at the single-atom level. *Science*, 329(5991):547–550, 2010.

[46] Peter Würtz, Tim Langen, Tatjana Gericke, Andreas Koglbauer, and Herwig Ott. Experimental demonstration of single-site addressability in a two-dimensional optical lattice. *Phys. Rev. Lett.*, 103:080404, Aug 2009.

[47] C. Weitenberg, M. Endres, J. F. Sherson, M. Cheneau, P. Schauß, T. Fukuhara, I. Bloch, and S. Kuhr. Single-spin addressing in an atomic mott insulator. *Nature*, 471:319–324, 2011.

[48] Yang Wang, Xianli Zhang, Theodore A. Corcovilos, Aishwarya Kumar, and David S. Weiss. Coherent addressing of individual neutral atoms in a 3d optical lattice. *Phys. Rev. Lett.*, 115:043003, Jul 2015.

[49] Masao Takamoto, Feng-Lei Hong, Ryoichi Higashi, and Hidetoshi Katori. An optical lattice clock. *Nature*, 435:321–324, 2005.

[50] B. J. Bloom, T. L. Nicholson, J. R. Williams, S. L. Campbell, M. Bishof, X. Zhang, W. Zhang, S. L. Bromley, and J. Ye. An optical lattice clock with accuracy and stability at the 10^{-18} level. *Nature*, 506:71–75, 2014.

[51] D. M. Stamper-Kurn, M. R. Andrews, A. P. Chikkatur, S. Inouye, H.-J. Miesner, J. Stenger, and W. Ketterle. Optical confinement of a bose-einstein condensate. *Phys. Rev. Lett.*, 80:2027–2030, Mar 1998.

[52] M. D. Barrett, J. A. Sauer, and M. S. Chapman. All-optical formation of an atomic bose-einstein condensate. *Phys. Rev. Lett.*, 87:010404, Jun 2001.

[53] Tin-Lun Ho. Spinor bose condensates in optical traps. *Phys. Rev. Lett.*, 81:742–745, Jul 1998.

[54] Tetsuo Ohmi and Kazushige Machida. Bose-einstein condensation with internal degrees of freedom in alkali atom gases. *Journal of the Physical Society of Japan*, 67(6):1822–1825, 1998.

[55] Dan M. Stamper-Kurn and Masahito Ueda. Spinor bose gases: Symmetries, magnetism, and quantum dynamics. *Rev. Mod. Phys.*, 85:1191–1244, Jul 2013.

[56] Yuki Kawaguchi and Masahito Ueda. Spinor bose-einstein condensates. *Physics Reports*, 520(5):253 – 381, 2012. Spinor Bose–Einstein condensates.

[57] Fabrice Gerbier, Artur Widera, Simon Fölling, Olaf Mandel, and Immanuel Bloch. Resonant control of spin dynamics in ultracold quantum gases by microwave dressing. *Phys. Rev. A*, 73:041602, Apr 2006.

[58] L. Zhao, J. Jiang, T. Tang, M. Webb, and Y. Liu. Dynamics in spinor condensates tuned by a microwave dressing field. *Phys. Rev. A*, 89:023608, Feb 2014.

[59] Z. Zhang and L.-M. Duan. Generation of massive entanglement through an adiabatic quantum phase transition in a spinor condensate. *Phys. Rev. Lett.*, 111:180401, Oct 2013.

[60] T. M. Hoang, C. S. Gerving, B. J. Land, M. Anquez, C. D. Hamley, and M. S. Chapman. Dynamic stabilization of a quantum many-body spin system. *Phys. Rev. Lett.*, 111:090403, Aug 2013.

[61] C. D. Hamley, C. S. Gerving, T. M. Hoang, E. M. Bookjans, and M. S. Chapman. Spin-nematic squeezed vacuum in a quantum gas. *Nature Physics*, 8:305, 2012.

[62] J. Jiang, L. Zhao, M. Webb, N. Jiang, H. Yang, and Y. Liu. Simple and efficient all-optical production of spinor condensates. *Phys. Rev. A*, 88:033620, Sep 2013.

[63] E. M. Bookjans, A. Vinit, and C. Raman. Quantum phase transition in an antiferromagnetic spinor bose-einstein condensate. *Phys. Rev. Lett.*, 107:195306, Nov 2011.

[64] A. T. Black, E. Gomez, L. D. Turner, S. Jung, and P. D. Lett. Spinor dynamics in an antiferromagnetic spin-1 condensate. *Phys. Rev. Lett.*, 99:070403, Aug 2007.

[65] Y. Liu, S. Jung, S. E. Maxwell, L. D. Turner, E. Tiesinga, and P. D. Lett. Quantum phase transitions and continuous observation of spinor dynamics in an antiferromagnetic condensate. *Phys. Rev. Lett.*, 102:125301, Mar 2009.

[66] Y. Liu, E. Gomez, S. E. Maxwell, L. D. Turner, E. Tiesinga, and P. D. Lett. Number fluctuations and energy dissipation in sodium spinor condensates. *Phys. Rev. Lett.*, 102:225301, Jun 2009.

[67] David Jacob, Lingxuan Shao, Vincent Corre, Tilman Zibold, Luigi De Sarlo, Emmanuel Mimoun, Jean Dalibard, and Fabrice Gerbier. Phase diagram of spin-1 antiferromagnetic bose-einstein condensates. *Phys. Rev. A*, 86:061601, Dec 2012.

[68] M.-S. Chang, Q. Qin, W. Zhang, L. You, and M. S. Chapman. Coherent spinor dynamics in a spin-1 bose condensate. *Nature Physics*, 1:111, 2005.

[69] A. Widera, F. Gerbier, S. Fölling, T. Gericke, O. Mandel, and I. Bloch. Precision measurement of spin-dependent interaction strengths for spin-1 and spin-2 87 rb atoms. *New Journal of Physics*, 8(8):152, 2006.

[70] H. Schmaljohann, M. Erhard, J. Kronjäger, M. Kottke, S. van Staa, L. Cacciapuoti, J. J. Arlt, K. Bongs, and K. Sengstock. Dynamics of $f = 2$ spinor bose-einstein condensates. *Phys. Rev. Lett.*, 92:040402, Jan 2004.

[71] J. Kronjäger, C. Becker, P. Navez, K. Bongs, and K. Sengstock. Magnetically tuned spin dynamics resonance. *Phys. Rev. Lett.*, 97:110404, Sep 2006.

[72] T. Kuwamoto, K. Araki, T. Eno, and T. Hirano. Magnetic field dependence of the dynamics of ^{87}Rb spin-2 bose-einstein condensates. *Phys. Rev. A*, 69:063604, Jun 2004.

[73] D. A. Steck. Sodium d line data. *available online at http://steck.us/alkalidata (revision 2.1.4, 23 December 2010).*

[74] H. J. Metcalf and P. V. Straten. *Laser Cooling and Trapping.* Springer, Verlag, New York, 1999.

[75] Paul D. Lett, Richard N. Watts, Christoph I. Westbrook, William D. Phillips, Phillip L. Gould, and Harold J. Metcalf. Observation of atoms laser cooled below the doppler limit. *Phys. Rev. Lett.*, 61:169–172, Jul 1988.

[76] K. I. Lee, J. A. Kim, H. R. Noh, and W. Jhe. Single-beam atom trap in a pyramidal and conical hollow mirror. *Opt. Lett.*, 21(15):1177–1179, Aug 1996.

[77] M. Vangeleyn, P. F. Griffin, E. Riis, and A. S. Arnold. Single-laser, one beam, tetrahedral magneto-optical trap. *Opt. Express*, 17(16):13601–13608, Aug 2009.

[78] J. Schoser, A. Batär, R. Löw, V. Schweikhard, A. Grabowski, Yu. B. Ovchinnikov, and T. Pfau. Intense source of cold rb atoms from a pure two-dimensional magneto-optical trap. *Phys. Rev. A*, 66:023410, Aug 2002.

[79] K. Dieckmann, R. J. C. Spreeuw, M. Weidemüller, and J. T. M. Walraven. Two-dimensional magneto-optical trap as a source of slow atoms. *Phys. Rev. A*, 58:3891–3895, Nov 1998.

[80] Matthew T. Hummon, Mark Yeo, Benjamin K. Stuhl, Alejandra L. Collopy, Yong Xia, and Jun Ye. 2d magneto-optical trapping of diatomic molecules. *Phys. Rev. Lett.*, 110:143001, Apr 2013.

[81] J. Reichel, W. Hänsel, and T. W. Hänsch. Atomic micromanipulation with magnetic surface traps. *Phys. Rev. Lett.*, 83:3398–3401, Oct 1999.

[82] C. C. Nshii, M. Vangeleyn, J. P. Cotter, P. F. Griffin, E. A. Hinds, C. N. Ironside, P. See, A. G. Sinclair, E. Riis, and A. S. Arnold. A surface-patterned chip as a strong source of ultracold atoms for quantum technologies. *Nature Nanotechnology*, 8:321–324, Apr 2013.

[83] Rudolf Grimm, Matthias Weidemüller, and Yurii B. Ovchinnikov. Optical dipole traps for neutral atoms. *Advances In Atomic, Molecular, and Optical Physics*, 42:95–170, 2000.

[84] L. Allen and J. H. Eberly. *Optical Resonance and Two-Level Atoms*. Dover Publications, New York, 1987.

[85] H. F. Hess. *Bull. Am. Phys. Soc.*, 30:854, 1985.

[86] Harald F. Hess. Evaporative cooling of magnetically trapped and compressed spin-polarized hydrogen. *Phys. Rev. B*, 34:3476–3479, Sep 1986.

[87] Harald F. Hess, Greg P. Kochanski, John M. Doyle, Naoto Masuhara, Daniel Kleppner, and Thomas J. Greytak. Magnetic trapping of spin-polarized atomic hydrogen. *Phys. Rev. Lett.*, 59:672–675, Aug 1987.

[88] C. S. Adams, H. J. Lee, N. Davidson, M. Kasevich, and S. Chu. Evaporative cooling in a crossed dipole trap. *Phys. Rev. Lett.*, 74:3577–3580, May 1995.

[89] K. B. Davis, M.-O. Mewes, and W. Ketterle. An analytical model for evaporative cooling of atoms. *Applied Physics B*, 60(2-3):155–159, 1995.

[90] K. M. O'Hara, M. E. Gehm, S. R. Granade, and J. E. Thomas. Scaling laws for evaporative cooling in time-dependent optical traps. *Phys. Rev. A*, 64:051403, Oct 2001.

[91] E. A. Donley, T. P. Heavner, F. Levi, M. O. Tataw, and S. R. Jefferts. Double-pass acousto-optic modulator system. *Review of Scientific Instruments*, 76(6):063112, 2005.

[92] Arthur L. Schawlow. Spectroscopy in a new light. *Rev. Mod. Phys.*, 54:697–707, Jul 1982.

[93] Dallin Durfee. *Dynamic Properties of Dilute Bose-Einsterin Condensates*. PhD thesis, Massachusetts Institute of Technology, 1999.

[94] G. Edward Marti, Ryan Olf, Enrico Vogt, Anton Öttl, and Dan M. Stamper-Kurn. Two-element zeeman slower for rubidium and lithium. *Phys. Rev. A*, 81:043424, Apr 2010.

[95] P. Cheiney, O. Carraz, D. Bartoszek-Bober, S. Faure, F. Vermersch, C. M. Fabre, G. L. Gattobigio, T. Lahaye, D. Gury-Odelin, and R. Mathevet. A zeeman slower design with permanent magnets in a halbach configuration. *Review of Scientific Instruments*, 82(6):063115, 2011.

[96] S. C. Bell, M. Junker, M. Jasperse, L. D. Turner, Y.-J. Lin, I. B. Spielman, and R. E. Scholten. A slow atom source using a collimated effusive oven and a single-layer variable pitch coil zeeman slower. *Review of Scientific Instruments*, 81(1):013105, 2010.

[97] D. S. Naik. *Bose-Einstein Condensation: Building the Testbeds to Study Superfluidity*. PhD thesis, Georgia Institute of Technology, December 2006.

[98] H. Wallis and W. Ertmer. Fokker-planck analysis of atomic beam cooling by frequency chirp methods. *Journal of Physics B: Atomic, Molecular and Optical Physics*, 21(17):2999, 1988.

[99] M. Zhu, C. W. Oates, and J. L. Hall. Continuous high-flux monovelocity atomic beam based on a broadband laser-cooling technique. *Phys. Rev. Lett.*, 67:46–49, Jul 1991.

[100] Kurt E. Gibble, Steven Kasapi, and Steven Chu. Improved magneto-optic trapping in a vapor cell. *Opt. Lett.*, 17(7):526–528, Apr 1992.

[101] L. Zhao, J. Jiang, and Y. Liu. Optimizing a spin-flip zeeman slower. *arXiv:1401.7181 [cond-mat.quant-gas]*, 2014.

[102] S. Friebel, C. D'Andrea, J. Walz, M. Weitz, and T. W. Hänsch. co_2-laser optical lattice with cold rubidium atoms. *Phys. Rev. A*, 57:R20–R23, Jan 1998.

[103] Wolfgang Ketterle and N.J. Van Druten. Evaporative cooling of trapped atoms. 37:181–236, 1996.

[104] Y.-J. Lin, A. R. Perry, R. L. Compton, I. B. Spielman, and J. V. Porto. Rapid production of ^{87}Rb bose-einstein condensates in a combined magnetic and optical potential. *Phys. Rev. A*, 79:063631, Jun 2009.

[105] R. Dumke, M. Johanning, E. Gomez, J. D. Weinstein, K. M. Jones, and P. D. Lett. All-optical generation and photoassociative probing of sodium bose-einstein condensates. *New Journal of Physics*, 8(5):64, 2006.

[106] K. J. Arnold and M. D. Barrett. All-optical bose-einstein condensation in a 1.06μm dipole trap. *Optics Communications*, 284(13):3288 – 3291, 2011.

[107] T. Kinoshita, T. Wenger, and D. S. Weiss. All-optical bose-einstein condensation using a compressible crossed dipole trap. *Phys. Rev. A*, 71:011602, Jan 2005.

[108] J.-F. Clément, J.-P. Brantut, M. Robert-de Saint-Vincent, R. A. Nyman, A. Aspect, T. Bourdel, and P. Bouyer. All-optical runaway evaporation to bose-einstein condensation. *Phys. Rev. A*, 79:061406, Jun 2009.

[109] Y. Takasu, K. Maki, K. Komori, T. Takano, K. Honda, M. Kumakura, T. Yabuzaki, and Y. Takahashi. Spin-singlet bose-einstein condensation of two-electron atoms. *Phys. Rev. Lett.*, 91:040404, Jul 2003.

[110] Abraham J. Olson, Robert J. Niffenegger, and Yong P. Chen. Optimizing the efficiency of evaporative cooling in optical dipole traps. *Phys. Rev. A*, 87:053613, May 2013.

[111] S. R. Granade, M. E. Gehm, K. M. O'Hara, and J. E. Thomas. All-optical production of a degenerate fermi gas. *Phys. Rev. Lett.*, 88:120405, Mar 2002.

[112] J. Stenger, S. Inouye, D. M. Stamper-Kurn, H.-J. Miesner, A. P. Chikkatur, and W. Ketterle. Spin domains in ground-state bose-einstein condensates. *Nature*, 396:345–348, 1998.

[113] S. J. M. Kuppens, K. L. Corwin, K. W. Miller, T. E. Chupp, and C. E. Wieman. Loading an optical dipole trap. *Phys. Rev. A*, 62:013406, Jun 2000.

[114] T. Takekoshi and R. J. Knize. Co2 laser trap for cesium atoms. *Opt. Lett.*, 21(1):77–79, Jan 1996.

[115] Chen-Lung Hung, Xibo Zhang, Nathan Gemelke, and Cheng Chin. Accelerating evaporative cooling of atoms into bose-einstein condensation in optical traps. *Phys. Rev. A*, 78:011604, Jul 2008.

[116] O. J. Luiten, M. W. Reynolds, and J. T. M. Walraven. Kinetic theory of the evaporative cooling of a trapped gas. *Phys. Rev. A*, 53:381–389, Jan 1996.

[117] M. Yan, R. Chakraborty, A. Mazurenko, P. G. Mickelson, Y. N. Martinez de Escobar, B. J. DeSalvo, and T. C. Killian. Numerical modeling of collisional dynamics of sr in an optical dipole trap. *Phys. Rev. A*, 83:032705, Mar 2011.

[118] W. Zhang, D. L. Zhou, M.-S. Chang, M. S. Chapman, and L. You. Coherent spin mixing dynamics in a spin-1 atomic condensate. *Phys. Rev. A*, 72:013602, Jul 2005.

[119] Yuki Kawaguchi, Hiroki Saito, Kazue Kudo, and Masahito Ueda. Spontaneous magnetic ordering in a ferromagnetic spinor dipolar bose-einstein condensate. *Phys. Rev. A*, 82:043627, Oct 2010.

[120] Austen Lamacraft. Spin-1 microcondensate in a magnetic field. *Phys. Rev. A*, 83:033605, Mar 2011.

[121] S. R. Leslie, J. Guzman, M. Vengalattore, Jay D. Sau, Marvin L. Cohen, and D. M. Stamper-Kurn. Amplification of fluctuations in a spinor bose-einstein condensate. *Phys. Rev. A*, 79:043631, Apr 2009.

[122] J. Jiang, L. Zhao, M. Webb, and Y. Liu. Mapping the phase diagram of spinor condensates via adiabatic quantum phase transitions. *Phys. Rev. A*, 90:023610, Aug 2014.

[123] Wenxian Zhang, Su Yi, and Li You. Mean field ground state of a spin-1 condensate in a magnetic field. *New Journal of Physics*, 5(1):77, 2003.

[124] C. Becker, P. Soltan-Panahi, J. Kronjäer, S. Döscher, K. Bongs, and K. Sengstock. Ultracold quantum gases in triangular optical lattices. *New Journal of Physics*, 12(6):065025, 2010.

[125] A. Widera, F. Gerbier, S. Fölling, T. Gericke, O. Mandel, and I. Bloch. Coherent collisional spin dynamics in optical lattices. *Phys. Rev. Lett.*, 95:190405, Nov 2005.

[126] P. L. Pedersen, M. Gajdacz, F. Deuretzbacher, L. Santos, C. Klempt, J. F. Sherson, A. J. Hilliard, and J. J. Arlt. Spin dynamics in a two-dimensional quantum gas. *Phys. Rev. A*, 89:051603, May 2014.

[127] A. Widera, F. Gerbier, S. Föling, T. Gericke, O. Mandel, and I. Bloch. Precision measurement of spin-dependent interaction strengths for spin-1 and spin-2 87 rb atoms. *New Journal of Physics*, 8(8):152, 2006.

[128] L. Zhao, J. Jiang, T. Tang, M. Webb, and Y. Liu. Antiferromagnetic spinor condensates in a two-dimensional optical lattice. *Phys. Rev. Lett.*, 114:225302, Jun 2015.

[129] K. Xu, Y. Liu, J. R. Abo-Shaeer, T. Mukaiyama, J. K. Chin, D. E. Miller, W. Ketterle, Kevin M. Jones, and Eite Tiesinga. Sodium bose-einstein condensates in an optical lattice. *Phys. Rev. A*, 72:043604, Oct 2005.

[130] K. Xu, Y. Liu, D. E. Miller, J. K. Chin, W. Setiawan, and W. Ketterle. Observation of strong quantum depletion in a gaseous bose-einstein condensate. *Phys. Rev. Lett.*, 96:180405, May 2006.

APPENDIX A

Simple and efficient all-optical production of spinor condensates

This appendix includes a reprint of Ref. [62]: J. Jiang, L. Zhao, M. Webb, N. Jiang, H. Yang, and Y. Liu, Simple and efficient all-optical production of spinor condensates, Physical Review A **88**, 033620 (2013).

Simple and efficient all-optical production of spinor condensates

J. Jiang,[1] L. Zhao,[1] M. Webb,[1] N. Jiang,[2] H. Yang,[2] and Y. Liu[1,*]
[1]*Department of Physics, Oklahoma State University, Stillwater, Oklahoma 74078, USA*
[2]*Center for Quantum Information, IIIS, Tsinghua University, Beijing, China*
(Received 4 June 2013; revised manuscript received 13 August 2013; published 17 September 2013)

We present a simple and optimal experimental scheme for an all-optical production of a sodium spinor Bose-Einstein condensate (BEC). With this scheme, we demonstrate that the number of atoms in a pure BEC can be greatly boosted by a factor of 5 over some widely used schemes in a simple single-beam or crossed-beam optical trap. Our scheme avoids technical challenges associated with some all-optical BEC methods and may be applicable to other optically trappable atomic species. In addition, we discuss an upper limit for evaporative cooling efficiency in all-optical BEC approaches and a good agreement between our theoretical model and experimental data.

DOI: 10.1103/PhysRevA.88.033620 PACS number(s): 67.85.Hj, 64.70.fm, 37.10.Jk, 32.60.+i

I. INTRODUCTION

In the last two decades, many techniques have been developed to reliably generate a Bose-Einstein condensate (BEC) of more than 10^4 atoms. Almost every one of these techniques requires evaporative cooling in a trapping potential, including a magnetic trap, an optical dipole trap (ODT), or a combined magnetic and optical potential [1–5]. Among these techniques, all-optical methods have been proven to be versatile and popularly applied in producing quantum-degenerate gases of both bosonic [6–14] and fermionic [15] species. ODTs have tight confinement, which allows for fast evaporation with a duty cycle of a few seconds [6]. Unlike magnetic potentials that only trap atoms in the weak-field-seeking spin state, an ODT can confine all spin components. This is crucial for creating vector (spinor) BECs with a spin degree of freedom [16]. ODTs can also be applied to a wider variety of atomic species (e.g., ytterbium, alkaline-earth metals, and cesium) which cannot be feasibly condensed in a magnetic trap [8,13]. In addition, optical trapping does not require magnetic coils around trapped atoms, which not only provides better optical access but also reduces residual magnetic fields. The simplicity and versatility of ODTs widens the accessibility of BEC research on many-body physics, precision measurements, and quantum information science [17].

Forced evaporation in an ODT can be performed by simply reducing its trap depth U (e.g., lowering the trapping laser power). In this process, collision rates decrease with U, which leads to slow rethermalization and eventually stagnation in evaporative cooling. Several methods have been reported to overcome this difficulty, including tilting an ODT with a magnetic-field gradient [18], using a misaligned crossed ODT [12,14], compressing an ODT with a mobile lens [11], and applying multiple ODTs for staged evaporation [8,10]. In this paper, however, we show that these methods may not be necessary for some atomic species, in particular, sodium atoms. Good agreements between our model and experimental data enable us to develop an optimal ODT ramp and evaporation sequence for an all-optical production of sodium BECs. With this optimal scheme, we find that the number of atoms in a pure BEC is greatly boosted by a factor of 5 over some popular schemes and evaporation efficiency $\gamma = -d(\ln D)/d(\ln N)$ can be 3.5 in a crossed ODT. Here D is the phase space density, and N is the number of atoms. We also show an upper limit for γ at a given truncation parameter $\eta = U/k_BT$ and demonstrate that a constant η does not yield more efficient evaporative cooling. Here T is the atom temperature and k_B is the Boltzmann constant. This optimal experimental scheme allows us to avoid technical challenges associated with some all-optical BEC approaches.

II. EXPERIMENTAL SETUP

Our apparatus is divided by differential pumping tubes into an atomic oven chamber, an intermediate chamber, and a main chamber where a magneto-optical trap (MOT) is located [19], as shown in Fig. 1(a). Hot atoms are slowed down by a spin-flip Zeeman slower [21] and then collected in the MOT, which is constructed with six cooling beams and a pair of 24-turn anti-Helmholtz coils. Each MOT cooling beam is detuned by $\delta_{\text{cooling}} = -20$ MHz from the cycling transition, has a power of 6 mW, and combines with one 3.5-mW MOT repumping beam in a single-mode fiber. Every MOT repumping beam is detuned by $\delta_{\text{repump}} = -5$ MHz from the $|F = 1\rangle$ to $|F' = 2\rangle$ transition. After 8.5 s of MOT loading, a three-step polarization gradient cooling process efficiently cools 3×10^8 atoms to 40 μK [19]. To depump atoms into the $F = 1$ hyperfine states, the repumping beams are extinguished 1 ms before cooling beams and MOT coils are turned off. Figure 1(b) lists a typical experimental sequence for our all-optical BEC approach.

A crossed ODT consists of two far-detuned beams which originate from an IR laser with a maximum power of 13 W at 1064 nm and have a waist of 33 μm [22] at their intersection point, as shown in Fig. 1(a). A single-mode polarization-maintaining fiber is used to polish the beam mode and to minimize pointing fluctuations due to imperfections of the IR laser and thermal contractions of an acoustic-optical modulator. As a result, atoms which are transferred from the MOT into the tightly focused crossed ODT demonstrate a long lifetime of 8 s and a large collision rate. These are essential for all-optical BEC approaches.

A couple of ODT ramp sequences were proposed to improve the ODT capture efficiency by finding a reasonable balance between two competing ODT-induced effects [6,7,9,10,12–14,23,24]. First, a larger U enables more atoms to

*yingmei.liu@okstate.edu

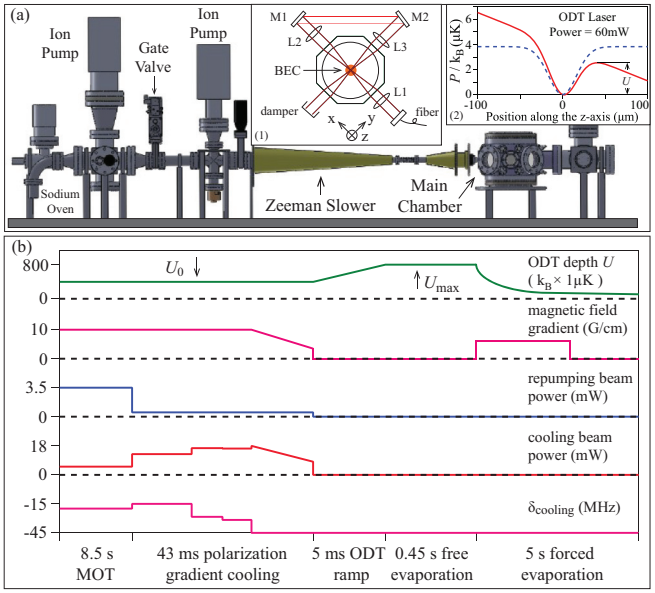

FIG. 1. (Color online) (a) Schematic of our apparatus. Inset 1: schematic of the crossed ODT setup around the main chamber. The positive z axis represents the direction of gravity. L_1, L_2, and L_3 are convex lenses. M_1 and M_2 are mirrors. Inset 2: the definition of the ODT trap depth U. The solid red line and dashed blue line represent the crossed ODT's trap potential energy P as a function of position along the z axis with and without taking into account the influence of gravity, respectively [20]. Here $x = y = 0$ and the ODT laser power is 60 mW. (b). Experimental sequence of creating sodium BECs with the all-optical approach (see text). Each MOT cooling beam is detuned by δ_{cooling} from the cycling transition. All axes are not to scale.

be captured in the ODT if the ODT beams do not interact with the MOT. The number of atoms loaded in the ODT is $N_{\text{rampA}} \sim \int_0^U \rho(\epsilon) f(\epsilon) d\epsilon$, where $\rho(\epsilon)$ and $f(\epsilon)$ are the density of states and occupation number at energy ϵ, respectively. This is confirmed by our data (blue triangles in Fig. 2) taken with

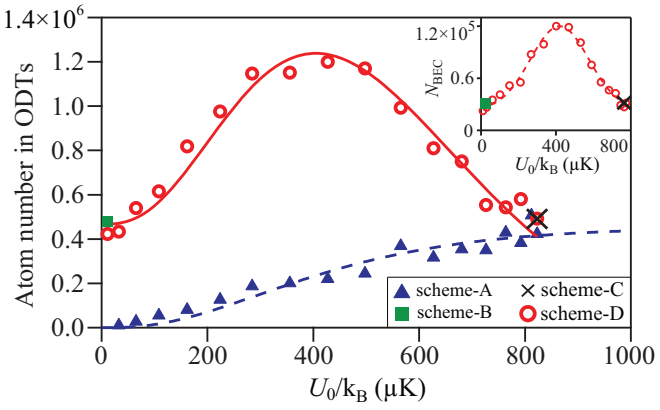

FIG. 2. (Color online) The number of atoms captured in the crossed ODT as a function of U_0 with the four ODT ramp sequences (see text). Our optimal scheme is the best scenario of scheme D when $U_0 \simeq U_{\text{max}}/2$. The dashed blue line and the solid red line are fits based on N_{rampA} and N_{rampD}, respectively (see text). Inset: the number of atoms in a BEC as a function of U_0 when one of the three schemes (i.e., schemes B–D) and the same evaporation curve are applied. The dashed red line is a Gaussian fit to the data.

scheme A, in which the ODT depth is linearly ramped in 5 ms from zero to U_0 immediately after MOT beams are switched off. On the other hand, there are some advantages to turning on intense ODT beams in the presence of MOT beams. For example, this allows the ODT to capture a larger number of cold and dense atoms by using MOT beams to prevent the gas from expanding. However, atoms experience non-negligible ac Stark shifts in regions where the ODT beams and the MOT overlap. As a result, the MOT's cooling capability is impaired in the MOT and ODT overlapping regions, and the number of atoms loaded into the ODT decreases when the ODT becomes too deep. N is thus not a monotonic function of U.

Scheme B (green squares in Fig. 2) is a popular scheme used to improve the ODT capture efficiency, in which ODT beams overlap with a MOT for a very short amount of time (20–200 ms) before the MOT beams are switched off [12,14,23,24]. Scheme C (black crosses in Fig. 2) is another widely applied scheme, which keeps the ODT beam at its maximum power during the entire MOT stage [6,9,10,13]. Figure 2 clearly shows that there is an optimal scheme which can increase the number of atoms loaded into the crossed ODT by a factor of 2.5 over the above two popular schemes. This optimal scheme is the best-case scenario for our scheme D. As shown in Fig. 1(b), the ODT in scheme D is kept at a small trap depth U_0 during the entire laser cooling process and is then linearly ramped to U_{max} in $t_{\text{ramp}} = 5$ ms. $U_{\text{max}} \approx k_B \times 800\ \mu$K is the maximal trap depth used in this work, and $0 \leqslant U_0 \leqslant U_{\text{max}}$. The number of atoms loaded into the ODT in scheme D may be expressed as $N_{\text{rampD}} \sim A\xi(U_0) \int_0^{U_0} \rho(\epsilon) f(\epsilon) d\epsilon + \int_{U_0}^{U_{\text{max}}} \rho(\epsilon) f(\epsilon) d\epsilon$. Here $\xi(U_0) = \exp\{-[\delta_{\text{ODT}}(U_0)]^2/\omega_0^2\}$ is a correction factor due to the ODT-induced shift $\delta_{\text{ODT}}(U_0)$, while A and ω_0 are fitting parameters. Our data collected with scheme D (red circles in Fig. 2) can be well fitted by this model. The fit value of ω_0 is 1.2Γ, where $\Gamma/2\pi = 9.7$ MHz is the natural linewidth of sodium. The number of atoms in the ODT reaches its peak when the optimal ramp sequence with $U_0 \simeq U_{\text{max}}/2$ is applied. Compared to the two popular schemes, the optimal scheme allows us to use ODT beams with smaller waists while loading the same amount of laser-cooled atoms to the ODT. The resulting high initial atom density and high collision rates from the optimal scheme enable very efficient evaporative cooling. This greatly boosts the number of atoms in a BEC by a factor of 5 over the two popular schemes for our apparatus, as shown in the inset in Fig. 2.

We find that our optimal scheme leads to a better ODT capture efficiency over the two popular schemes at every given frequency of the MOT beams within a wide range (i.e., -24 MHz $\leqslant \delta_{\text{cooling}} \leqslant -10$ MHz and -15 MHz $\leqslant \delta_{\text{repump}} \leqslant 6$ MHz). One mechanism may explain this phenomenon: well-aligned crossed ODT beams have a much larger intensity in the intersection region than that in the "wing" (nonintersecting) region. In other words, the light shift induced by the ODT beams is not uniform, i.e., a big shift in the intersection region and a small shift in the "wing" region. These ODT-induced nonuniform shifts cannot be mimicked by simply varying the frequencies of the MOT cooling and repumping beams. Because this mechanism does not depend on atomic species, our optimal scheme may thus be applicable to rubidium and other optical trappable atomic species.

III. EVAPORATIVE COOLING

To optimize γ, it is necessary to understand the time evolution of the system energy E and the atom number N during an evaporation process. Similar to Refs. [14,25–27], we use $\kappa k_B T \approx (\eta - 5)/(\eta - 4)k_B T$ to represent the average kinetic energy taken by an atom when it is removed from the ODT, and we assume the mean kinetic energy and mean potential energy to be $E/2$ when η is large. The time evolution of E and N is thus given by

$$\begin{aligned} \dot{E} &= -\frac{2(\eta-4)e^{-\eta}N}{\tau_2}(U+\kappa k_B T) + \frac{\dot{U}}{U}\frac{E}{2} + \dot{E}|_{\text{loss}}, \\ \dot{N} &= -2(\eta-4)e^{-\eta}N/\tau_2 + \dot{N}|_{\text{loss}}, \end{aligned} \tag{1}$$

where τ_2 is the time constant of the two-body elastic collision. In Eq. (1), $\dot{E}|_{\text{loss}}$ and $\dot{N}|_{\text{loss}}$ are due to various inelastic loss mechanisms and may be expressed as

$$\begin{aligned} \dot{E}|_{\text{loss}} &= k_s N - k_1 N(3k_B T) - k_3 n^2 N(2k_B T), \\ \dot{N}|_{\text{loss}} &= -k_1 N - k_3 n^2 N, \end{aligned} \tag{2}$$

where k_1 and k_3 are one-body and three-body loss rates, respectively. k_s represents heating introduced by ODT beams via a number of different mechanisms, such as pointing fluctuations of the ODT beams, a bad laser beam mode, and spontaneous light scattering. The term $2k_B T$ in Eq. (2) accounts for the fact that atoms in the ODT's center have higher density and thus are more affected by the three-body inelastic loss [12].

In our apparatus with the UHV pressure in the 10^{-12} Torr range, background collisions are negligible. Since the ODT beams are delivered via a single-mode polarization-maintaining fiber, heating induced by the ODT beams is minimized. k_1 and k_s are thus very small. If we ignore k_1 and k_s, Eq. (1) can be simplified to

$$\dot{E} = \dot{N}\eta_{\text{eff}} k_B T + \frac{\dot{U}}{U}\frac{E}{2}, \tag{3}$$

where $\eta_{\text{eff}} = \eta + \kappa - R(\eta + \kappa - 2)$. We define $R = (\dot{N}|_{\text{loss}})/\dot{N} = 1/[1 + 2(\eta - 4)e^{-\eta} R_{\text{gTb}}]$ to represent the portion of atom losses due to inelastic collisions, where R_{gTb} is the ratio of the inelastic collision time constant to τ_2. From solving the above equations, γ may be expressed as

$$\gamma = \eta_{\text{eff}} - 4 = \eta + \kappa - R(\eta + \kappa - 2) - 4. \tag{4}$$

The value of η in many publications on optical productions of BECs was held constant with $\Delta\eta = 0$ [6,7,11,12,14,15,18]. Our data in Fig. 3, however, show that a constant η does not lead to better evaporation or a larger γ. The values of γ in Fig. 3 are extracted from 36 evaporation processes in which the forced evaporation speed and the hold time at $U_{\max}$ are changed independently, although they all start with the same initial number of cold atoms in the crossed ODT. $\Delta\eta = \eta_f - \eta_i$ is the change of η during forced evaporation, where η_i and η_f are the values of η at $U_{\max}$ (i.e., the beginning of forced evaporation) and at U_f, respectively. In order to avoid overestimating γ due to the bosonic enhancement near the BEC transition temperature, we choose $U_f = k_B \times 30\mu$K, where no BEC appears. We find that $\Delta\eta$ tends to be a non-negative value when the forced evaporation time is longer than 1 s (solid black squares in Fig. 3), which is a good indication of sufficient rethermalization. We also find that γ is too small to yield a BEC when $\Delta\eta < -2.5$.

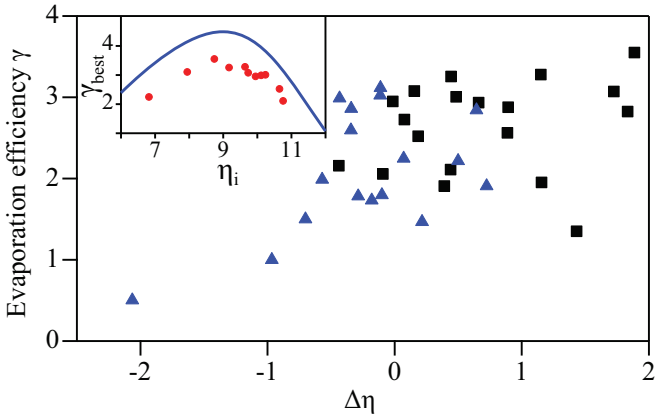

FIG. 3. (Color online) Evaporation efficiency γ in 36 different evaporation processes as a function of $\Delta\eta$. Solid black squares are data taken with the forced evaporation time longer than 1 s. Inset: γ_{best} as a function of η_i extracted from the main figure. The solid line sets an upper limit for γ based on Eq. (4) by assuming $k_1 = k_s = 0$ (see text).

We compare the evaporation efficiency at different values of η_i, as shown in the inset of Fig. 3. γ_{best} (the best achieved value of γ at a given η_i in our system) does not show a strong dependence on η_i if $8 < \eta_i < 10$, while γ_{best} sharply diminishes when η_i becomes too large or too small. In the inset of Fig. 3, a similar relationship between γ and η_i is also predicted by the solid blue line, which is a result based on Eq. (4) by ignoring k_1 and k_s and by applying a nonzero R (i.e., $R_{\text{gTb}} = 4000$ [4]). All of our data lie below the solid line in the inset, which may indicate that k_1 and k_s are larger than zero and cannot be ignored. Therefore, based on Fig. 3, we need to choose a value between 8 and 10 for η_i and keep $\Delta\eta$ larger than -0.5 in order to optimize evaporation efficiency γ.

The maximum achievable value for η_i appears to be 10.8, as shown in the inset of Fig. 3. To understand this, we monitor the time evolution of η and find that η has a maximal value $\eta_{\max}$ at a given ODT depth U. The value of $\eta_{\max}$ decreases exponentially with U, and $\eta_{\max}$ at $U_{\max}$ is 10.8, which agrees well with our theoretical prediction (solid red line in Fig. 4). Therefore, if one wishes to keep η unchanged during forced evaporation, η must be limited to 10.8 even though $\eta_{\max}$ can be much higher at low ODT depths (e.g., $\eta_{\max} > 13$ for $U/k_B < 100\mu$K). This may be one reason why a constant η does not yield more efficient evaporative cooling. We also find that the time evolution of η at every U discussed in this paper can be well fitted with our model. Two typical fitting curves are shown in the inset of Fig. 4.

A pure $F = 1$ BEC of 1.2×10^5 sodium atoms at 50 nK is created from a 0.45-s free evaporation at $U_{\max}$ followed by a 5-s forced evaporation in which U is exponentially reduced. This evaporation curve provides two important parameters for efficient evaporative cooling: η_i is between 8 and 10, and the forced evaporation time is long enough for sufficient rethermalization but short enough to avoid excessive atom losses. Two time-of-flight absorption images in Fig. 5(a) show a typical change in the condensate fraction (CF) after

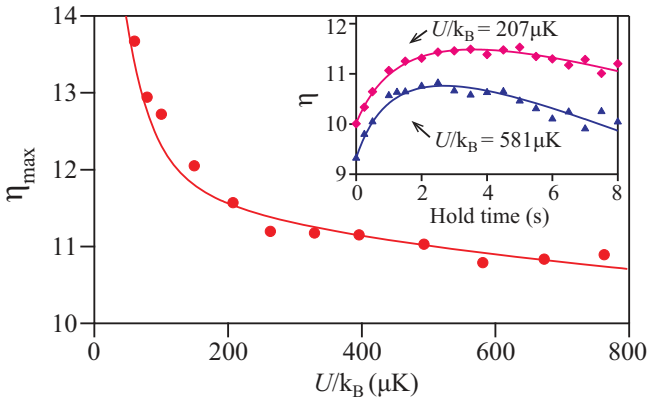

FIG. 4. (Color online) $\eta_{\max}$ as a function of the ODT depth U when atoms are held at a fixed U for 8 s. The solid line is a fit based on Eqs. (1) and (2) (see text). Inset: the time evolution of η at two typical ODT depths. Solid lines are fits based on the same model applied in the main figure (see text).

interrupting the evaporation curve at various U. We also apply the above all-optical approach to evaporate atoms in a single-beam ODT. A similar result can also be achieved in

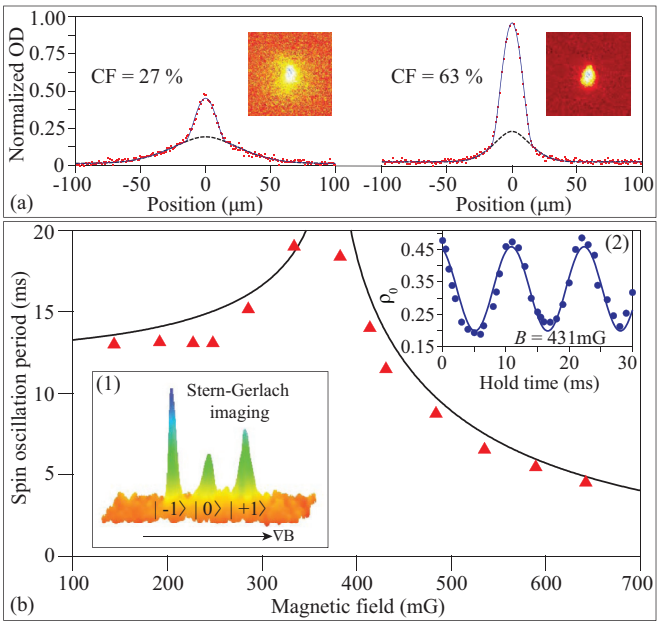

FIG. 5. (Color online) (a) Absorption images taken after interrupting an optimized evaporation curve at various U followed by a 10-ms time of flight (see text). OD stands for the optical density. Dashed black lines and solid blue lines are fits to the column densities based on a Gaussian distribution and a bimodal distribution, respectively. $\mathrm{CF} = \widetilde{n}_c/(\widetilde{n}_{th} + \widetilde{n}_c)$, where $\widetilde{n}_{th}$ and $\widetilde{n}_c$ are column densities for the thermal cloud and the condensate, respectively. (b) The period of spin population oscillations as a function of B at $m = \rho_{+1} - \rho_{-1} = 0$. Here ρ_{m_F} is the fractional population of the m_F state. The solid black line is a fit based on the mean-field theory (see text). Inset 1: Three spin components of a $F = 1$ spinor BEC are spatially separated in a 3D Stern-Gerlach absorption image. Inset 2: A typical time evolution of ρ_0 at $B = 431$ mG and $m = 0$ when the spinor BEC is held in the crossed ODT. The solid blue line is a sinusoidal fit to the data.

the single-beam ODT as long as its beam waist is smaller than 16 μm so that it can provide a high enough collision rate. The resulting number of condensed atoms in the single-beam ODT, however, is four times smaller than that in the crossed ODT.

To fully polarize atoms in a $F = 1$ BEC to the $|F = 1, m_F = 1\rangle$ state, a weak-magnetic-field gradient is applied during forced evaporation, as shown in Fig. 1(b). We then ramp up a magnetic bias field with its strength B between 100 and 700 mG while turning off the field gradient. We can prepare an initial state with any desired combination of three m_F states by altering the amplitude and duration of a resonant rf pulse and/or a resonant microwave pulse. A Stern-Gerlach separation followed by absorption imaging is used to measure the populations of different spin states, as shown in inset 1 in Fig. 5(b).

The interesting interactions in spinor BECs are interconversion among multiple spin states and magnetic-field interactions characterized by the quadratic Zeeman effect. Such a system can be described with a simple two-dimensional phase space that we can manipulate to some degree by changing the magnetic-field strength or the density of the BEC [17,28]. When a $F = 1$ spinor BEC is taken out of equilibrium at a nonzero magnetic field, spin population oscillations can be observed, as shown in inset (2) in Fig. 5(b). The population oscillations are nearly harmonic except near $B = 370$ mG, a separatrix in phase space where the period diverges. The data can be well fitted by a prediction from the mean-field theory [solid line in Fig. 5(b)] [17] with only one fitting parameter (i.e., the mean BEC density). Figure 5(b) may thus be a good way to measure the mean BEC density and to check the values of the crossed ODT's trap frequency and trap depth [22].

IV. CONCLUSION

In conclusion, we have presented an optimal experimental scheme for an all-optical production of sodium spinor BECs. For our apparatus, we have found that the number of atoms in a pure BEC with this scheme is greatly boosted by a factor of 5 over two popular schemes in a crossed ODT. Our scheme avoids technical challenges associated with some all-optical BEC approaches and may be applicable to other optically trappable atomic species and molecules [29]. We have showed an upper limit for γ at a given η, demonstrated that a constant η could not yield a larger γ, and discussed good agreements between our model and experimental data. We may be able to further improve evaporation efficiency to reach its upper limit and thus to increase the number of atoms in a BEC by combining our scheme with one of the clever ideas shown in [8,12,14,18].

ACKNOWLEDGMENTS

We thank the Army Research Office, Oklahoma Center for the Advancement of Science and Technology, and Oak Ridge Associated Universities for financial support. M.W. thanks the Niblack Research Scholar program. N.J. and H.Y. thank the National Basic Research Program of China.

[1] K. B. Davis, M.-O. Mewes, M. R. Andrews, N. J. van Druten, D. S. Durfee, D. M. Kurn, and W. Ketterle, Phys. Rev. Lett. **75**, 3969 (1995).

[2] M. H. Anderson, J. R. Ensher, M. R. Matthews, C. E. Wieman, and E. A. Cornell, Science **269**, 198 (1995).

[3] C. C. Bradley, C. A. Sackett, J. J. Tollett, and R. G. Hulet, Phys. Rev. Lett. **75**, 1687 (1995).

[4] W. Ketterle and N. J. van Druten, Adv. At. Mol. Opt. Phys. **37**, 181 (1996).

[5] Y.-J. Lin, A. R. Perry, R. L. Compton, I. B. Spielman, and J. V. Porto, Phys. Rev. A **79**, 063631 (2009).

[6] M. D. Barrett, J. A. Sauer, and M. S. Chapman, Phys. Rev. Lett. **87**, 010404 (2001).

[7] R. Dumke, M. Johanning, E. Gomez, J. D. Weinstein, K. M. Jones, and P. D. Lett, New J. Phys. **8**, 64 (2006).

[8] T. Weber, J. Herbig, M. Mark, H.-C. Nägerl, and R. Grimm, Science **299**, 232 (2003).

[9] C. S. Adams, H. J. Lee, N. Davidson, M. Kasevich, and S. Chu, Phys. Rev. Lett. **74**, 3577 (1995).

[10] K. J. Arnold and M. D. Barrett, Opt. Commun. **284**, 3288 (2011).

[11] T. Kinoshita, T. Wenger, and D. S. Weiss, Phys. Rev. A **71**, 011602 (2005).

[12] J.-F. Clément, J.-P. Brantut, M. Robert-de-Saint-Vincent, R. A. Nyman, A. Aspect, T. Bourdel, and P. Bouyer, Phys. Rev. A **79**, 061406 (2009).

[13] Y. Takasu, K. Maki, K. Komori, T. Takano, K. Honda, M. Kumakura, T. Yabuzaki, and Y. Takahashi, Phys. Rev. Lett. **91**, 040404 (2003).

[14] A. J. Olson, R. J. Niffenegger, and Y. P. Chen, Phys. Rev. A **87**, 053613 (2013).

[15] S. R. Granade, M. E. Gehm, K. M. O'Hara, and J. E. Thomas, Phys. Rev. Lett. **88**, 120405 (2002).

[16] J. Stenger, S. Inouye, D. M. Stamper-Kurn, H.-J. Miesner, A. P. Chikkatur, and W. Ketterle, Nature (London) **396**, 345 (1998).

[17] D. M. Stamper-Kurn and M. Ueda, Rev. Mod. Phys. **85**, 1191 (2013).

[18] C.-L. Hung, X. Zhang, N. Gemelke, and C. Chin, Phys. Rev. A **78**, 011604 (2008).

[19] The intermediate chamber allows us to refill alkali metals and get UHV pressures back to the 10^{-12} Torr range within 24 h. The first polarization gradient cooling step compresses the MOT for 20 ms by increasing the power of each cooling beam to 12 mW while changing δ_{cooling} to -15 MHz. In this step, the power of each MOT repumping beam is also drastically reduced to 45 μW. Then during a 5-ms premolasses step, every cooling beam is further red detuned in addition to its power being increased to 16 mW. This is followed by a 18-ms optical molasses, in which a cooling beam is detuned to $\delta_{\text{cooling}} = -45$ MHz and its power linearly drops to 8 mW. The magnetic-field gradient is also reduced to 3 G/cm over the 18 ms.

[20] The crossed ODT trap potential energy is $P = P_1 + P_2 + P_g$, where P_1 and P_2 are trap potentials of the two single-beam ODTs and P_g is due to the influence of gravity.

[21] L. Zhao, J. Jiang, J. Austin, M. Webb, Y. Pu, and Y. Liu (unpublished).

[22] We determined the value of the ODT's beam waist by measuring its trap frequency with two methods. First, we recorded the number of atoms in the ODT after sinusoidally modulating U at various modulation frequencies f_{m}. The number of atoms exhibits parametric resonances at $f_{\text{m}} = l f_{\text{ODT}}$, where f_{ODT} is the ODT's radial frequency and l is a positive integer number. In the second method, we kicked atoms in the single-beam ODT with a magnetic-field gradient and then recorded the position of atoms after holding the atoms in the ODT for a variable length of time. It appeared that atoms experienced a harmonic oscillation with a frequency equal to the ODT's axial frequency. We ensured the two ODT beams were well intersected at their focal points with high-resolution imaging in three orthogonal directions. The values of the ODT's beam waist and its trap depth provided by these two methods are very close to each other and also agree with those derived from Fig. 5(b). In this paper, the uncertainty of η is found to be $\sim$4% based on the measurements with the above three methods.

[23] S. J. M. Kuppens, K. L. Corwin, K. W. Miller, T. E. Chupp, and C. E. Wieman, Phys. Rev. A **62**, 013406 (2000).

[24] T. Takekoshi and R. J. Knize, Opt. Lett. **21**, 77 (1996).

[25] K. M. O'Hara, M. E. Gehm, S. R. Granade, and J. E. Thomas, Phys. Rev. A **64**, 051403 (2001).

[26] O. J. Luiten, M. W. Reynolds, and J. T. M. Walraven, Phys. Rev. A **53**, 381 (1996).

[27] M. Yan, R. Chakraborty, A. Mazurenko, P. G. Mickelson, Y. N. Martinez de Escobar, B. J. DeSalvo, and T. C. Killian, Phys. Rev. A **83**, 032705 (2011).

[28] Y. Liu, S. Jung, S. E. Maxwell, L. D. Turner, E. Tiesinga, and P. D. Lett, Phys. Rev. Lett. **102**, 125301 (2009).

[29] Upon completion of this work, we recently become aware of Ref. [30] and its ODT ramp sequence, which linearly ramps ODTs from $U_{\text{max}}/3$ to U_{max} in $t_{\text{ramp}} = 2$ s. We find that the number of atoms in a pure BEC exponentially decreases with t_{ramp} when $t_{\text{ramp}} > 0.01$ s in our system. The optimal sequence explained in our paper yields a pure BEC of at least twice the number of atoms as that from a sequence with $t_{\text{ramp}} = 2$ s for our apparatus.

[30] D. Jacob, E. Mimoun, L. D. Sarlo, M. Weitz, J. Dalibard, and F. Gerbier, New J. Phys. **13**, 065022 (2011).

APPENDIX B

Dynamics in spinor condensates tuned by a microwave dressing field

This appendix includes a reprint of Ref. [58]: L. Zhao, J. Jiang, T. Tang, M. Webb, and Y. Liu, Dynamics in spinor condensates tuned by a microwave dressing field, Physical Review A **89**, 023608 (2014).

Dynamics in spinor condensates tuned by a microwave dressing field

L. Zhao, J. Jiang, T. Tang, M. Webb, and Y. Liu*
Department of Physics, Oklahoma State University, Stillwater, Oklahoma 74078, USA
(Received 24 October 2013; revised manuscript received 16 December 2013; published 10 February 2014)

We experimentally study spin dynamics in a sodium antiferromagnetic spinor condensate as a result of spin-dependent interactions c and microwave dressing field interactions characterized by the net quadratic Zeeman effect $q_{\rm net}$. In contrast to magnetic fields, microwave dressing fields enable us to access both negative and positive values of $q_{\rm net}$. We find an experimental signature to determine the sign of $q_{\rm net}$ and observe harmonic spin population oscillations at every $q_{\rm net}$ except near each separatrix in phase space where spin oscillation period diverges. No spin domains and spatial modes are observed in our system. Our data in the negative $q_{\rm net}$ region exactly resembles what is predicted to occur in a ferromagnetic spinor condensate in the positive $q_{\rm net}$ region. This observation agrees with an important prediction derived from the mean-field theory: spin dynamics in spin-1 condensates substantially depends on the sign of $q_{\rm net}/c$. This work uses only one atomic species to reveal mean-field spin dynamics, especially the remarkably different relationship between each separatrix and the magnetization, of spin-1 antiferromagnetic and ferromagnetic spinor condensates.

DOI: 10.1103/PhysRevA.89.023608 PACS number(s): 67.85.Hj, 32.60.+i, 03.75.Kk, 03.75.Mn

I. INTRODUCTION

An atomic Bose-Einstein condensate (BEC) is a state where all atoms have a single collective wave function for their spatial degrees of freedom. The key benefit of spinor BECs is the additional spin degree of freedom. Together with Feshbach resonances and optical lattices which tune the interatomic interactions, spinor BECs constitute a fascinating collective quantum system offering an unprecedented degree of control over such parameters as spin, temperature, and the dimensionality of the system [1,2]. Spinor BECs have become one of the fastest-moving research frontiers in the past 15 years. A number of atomic species have proven to be perfect candidates in the study of spinor BECs, such as $F = 1$ and $F = 2$ hyperfine spin states of ^{87}Rb atoms [1–7] and $F = 1$ hyperfine spin manifolds of ^{23}Na atoms [8–12]. Many interesting phenomena due to the interconversion among multiple spin states and magnetic field interactions have been experimentally demonstrated in spinor BECs, such as spin population dynamics [1–9], quantum number fluctuation [10,13], various quantum phase transitions [1,9,11,12], and quantum spin-nematic squeezing [14]. Spinor BEC systems have been successfully described with a classical two-dimensional phase space [1,2,15–17], a rotor model [18], or a quantum model [13,17].

In this paper, we experimentally study spin-mixing dynamics in a $F = 1$ sodium spinor condensate starting from a nonequilibrium initial state, driven by the net quadratic Zeeman energy $q_{\rm net} = q_M + q_B$ and antiferromagnetic spin-dependent interactions c. Here q_B and q_M are the quadratic Zeeman shifts induced by magnetic fields and microwave dressing fields, respectively. The spin-dependent interaction energy c is proportional to the mean BEC density and the difference in the $f = 0$ and $f = 2$ s-wave scattering lengths, where f is the summed spin angular momentum in a collision. It is well known that $c > 0$ (or $c < 0$) in $F = 1$ antiferromagnetic ^{23}Na (or ferromagnetic ^{87}Rb) spinor BECs. In contrast to a magnetic field, a microwave dressing field enables us to access both negative and positive values of $q_{\rm net}$. A method to characterize microwave dressing fields and an approach to adiabatically sweep $q_{\rm net}$ from $-\infty$ to $+\infty$ are also explained. In both negative and positive $q_{\rm net}$ regions, we observe spin population oscillations resulting from coherent collisional interconversion among two $|F = 1, m_F = 0\rangle$ atoms, one $|F = 1, m_F = +1\rangle$ atom, and one $|F = 1, m_F = -1\rangle$ atom. In every spin oscillation studied in this paper, our data show that the population of the $m_F = 0$ state averaged over time is always larger (or smaller) than its initial value as long as $q_{\rm net} < 0$ (or $q_{\rm net} > 0$). This observation provides a clear experimental signature to determine the sign of $q_{\rm net}$. We also find a remarkably different relationship between the total magnetization m and a separatrix in phase space where spin oscillation period diverges: The position of the separatrix moves slightly with m in the positive $q_{\rm net}$ region, while the separatrix quickly disappears when m is away from zero in the negative $q_{\rm net}$ region. Our data agree with an important prediction derived by Ref. [17]: The spin-mixing dynamics in $F = 1$ spinor condensates substantially depends on the sign of $R = q_{\rm net}/c$. This work uses only one atomic species to reveal mean-field spin dynamics, especially the relationship between each separatrix and the magnetization, which are predicted to appear differently in $F = 1$ antiferromagnetic and ferromagnetic spinor condensates.

Because no spin domains and spatial modes are observed in our system, the single spatial mode approximation (SMA), in which all spin states have the same spatial wave function, appears to be a proper theoretical model to understand our data. Similarly to Refs. [1,16], we take into account the conservation of the total atom number and the total magnetization m. Spin-mixing dynamics in a $F = 1$ spinor BEC can thus be described with a two-dimensional (ρ_0 versus θ) phase space, where the fractional population ρ_{m_F} and the phase θ_{m_F} of each m_F state are independent of position. The BEC energy E and the time evolution of ρ_0 and θ may be expressed as [1,16]

$$\begin{aligned} E &= q_{\rm net}(1-\rho_0) \\ &\quad + c\rho_0[(1-\rho_0) + \sqrt{(1-\rho_0)^2 - m^2}\cos\theta], \\ \dot{\rho_0} &= -(2/\hbar)\partial E/\partial\theta, \dot{\theta} = (2/\hbar)\partial E/\partial\rho_0. \end{aligned} \quad (1)$$

*yingmei.liu@okstate.edu

Here $\theta = \theta_{+1} + \theta_{-1} - 2\theta_0$ is the relative phase among the three m_F spin states and $\hbar$ is the reduced Planck constant. The induced linear Zeeman shift remains the same during the collisional spin interconversion and is thus ignored. The total magnetization is $m = \rho_{+1} - \rho_{-1}$. Spin dynamics in $F = 1$ antiferromagnetic and ferromagnetic spinor BECs have been studied in magnetic fields where $q_{\rm net} = q_B \propto B^2 > 0$ with ^{23}Na and ^{87}Rb atoms, respectively [1]. A few methods have been explored for generating a negative quadratic Zeeman shift, such as via a microwave dressing field [1,11,19–21] or through a linearly polarized off-resonant laser beam [22]. In this paper, we choose the first method.

II. EXPERIMENTAL SETUP

The experimental setup is similar to that illustrated in our previous work [23]. Hot ^{23}Na atoms are slowed by a spin-flip Zeeman slower, captured in a standard magneto-optical trap, cooled through a polarization gradient cooling process to 40 μK, and loaded into a crossed optical dipole trap originating from a linearly polarized high-power infrared laser at 1064 nm. After an optimized 6-s forced evaporative cooling process, a pure $F = 1$ BEC of 1.0×10^5 sodium atoms is created. The spin healing length and the Thomas-Fermi radii of a typical condensate studied in this paper are 13 μm and (6.1, 6.1, 4.3) μm, respectively. We can polarize atoms in the $F = 1$ BEC fully to the $|F = 1, m_F = -1\rangle$ state by applying a weak magnetic field gradient during the first half of the forced evaporation (or fully to the $|F = 1, m_F = 0\rangle$ state by adding a very strong magnetic bias field during the entire 6-s forced evaporation). We then ramp up a small magnetic bias field with its strength B being 271.5(4) mG, while turning off the field gradient. An rf-pulse resonant with the linear Zeeman splitting is applied to prepare an initial state with any desired combination of the three m_F states, which is followed by abruptly switching on an off-resonant microwave pulse to generate a proper microwave dressing field. To create sufficiently large $q_{\rm net}$, a microwave antenna designed for a frequency near the $|F = 1\rangle \leftrightarrow |F = 2\rangle$ transition is placed a few inches above the center of the magneto-optical trap and connected to a function generator outputting a maximum power of 10 W. The actual power used in this paper is ~8 W. After various hold times t in the optical dipole trap, the microwave dressing fields are quickly turned off. Populations of the multiple spin states are then measured via the standard absorption imaging preceded by a 3-ms Stern-Gerlach separation and a 7-ms time of flight.

The exact value of $q_{\rm net}$ is carefully calibrated from a few experimental parameters, such as the polarization and frequency of a microwave pulse. Similarly to Refs. [19,21], we express the value of $q_{\rm net}$ as

$$\begin{aligned} q_{\rm net} &= q_{\rm B} + q_{\rm M} \\ &= aB^2 h + \frac{\delta E|_{m_F=1} + \delta E|_{m_F=-1} - 2\delta E|_{m_F=0}}{2}, \\ \delta E|_{m_F} &= \frac{h}{4} \sum_{k=0,\pm1} \frac{\Omega^2_{m_F,m_F+k}}{\Delta_{m_F,m_F+k}} \\ &= \frac{h}{4} \sum_{k=0,\pm1} \frac{\Omega^2_{m_F,m_F+k}}{\Delta - [(m_F+k)/2 - (-m_F/2)]\mu_B B}, \end{aligned} \quad (2)$$

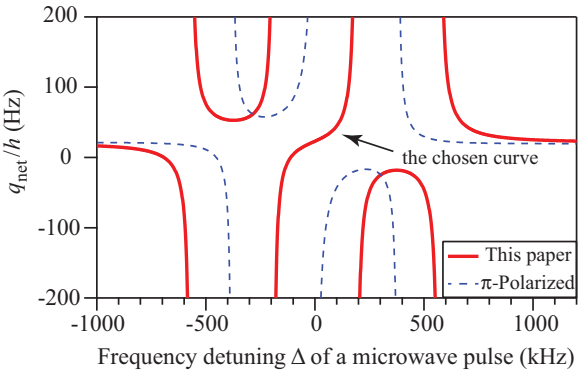

FIG. 1. (Color online) $q_{\rm net}$ as a function of Δ. The residual magnetic field is $B = 271.5(4)$ mG. Dashed blue lines represent the predictions derived from Eq. (2) when the microwave pulse is purely π polarized and its corresponding on-resonance Rabi frequencies are $\Omega_{-1,-2} = \Omega_{0,-1} = \Omega_{1,0} = \Omega_{-1,0} = \Omega_{0,1} = \Omega_{1,2} = 0$, $\Omega_{-1,-1} = \Omega_{1,1} = 4.2$ kHz, and $\Omega_{0,0} = 4.9$ kHz. Solid red lines represent the predictions from Eq. (2) for a typical microwave pulse used in this paper. The specially chosen polarization of this pulse yields nine on-resonance Rabi frequencies as follows: $\Omega_{-1,-2} = 5.1$ kHz, $\Omega_{0,-1} = 3.6$ kHz, and $\Omega_{1,0} = 2.1$ kHz are from the σ^--polarized component of the pulse; $\Omega_{-1,-1} = \Omega_{0,0} = \Omega_{1,1} = 0$ are from the π-polarized component of the pulse; and $\Omega_{-1,0} = 2.3$ kHz, $\Omega_{0,1} = 3.9$ kHz, and $\Omega_{1,2} = 5.5$ kHz are from the σ^+-polarized component of the pulse (see text). In this paper, Δ is tuned within the range of -190 kHz to 190 kHz from the $|F = 1, m_F = 0\rangle \leftrightarrow |F = 2, m_F = 0\rangle$ transition.

where $a \approx 277$ Hz/G^2 (or $a \approx 71$ Hz/G^2) for $F = 1$ ^{23}Na (or ^{87}Rb) atoms, the microwave pulse is detuned by Δ from the $|F = 1, m_F = 0\rangle \leftrightarrow |F = 2, m_F = 0\rangle$ transition, and h is the Planck constant. We define k as 0 or ±1 for a π- or a $\sigma^\pm$-polarized microwave pulse, respectively. For a given polarization k, the allowed transition is $|F = 1, m_F\rangle \leftrightarrow |F = 2, m_F + k\rangle$ and its on-resonance Rabi frequency is $\Omega_{m_F,m_F+k} \propto \sqrt{I_k} C_{m_F,m_F+k}$, where C_{m_F,m_F+k} is the Clebsch-Gordan coefficient of the transition and I_k is the intensity of this purely polarized microwave pulse. We also define $\Delta_{m_F,m_F+k} = \Delta - [(m_F + k)/2 - (-m_F/2)]\mu_B B$ as the frequency detuning of the microwave pulse with respect to the $|F = 1, m_F\rangle \rightarrow |F = 2, m_F + k\rangle$ transition, where μ_B is the Bohr magneton.

A purely π-polarized microwave pulse has been a popular choice in some publications [1,20,21]. However, we apply microwave pulses of a specially chosen polarization, in order to continuously scan $q_{\rm net}$ from large negative values to big positive values at a moderate microwave power. Figure 1 compares microwave dressing fields induced by a typical microwave pulse used in this paper and a purely π-polarized microwave pulse. This comparison clearly shows that it is possible to continuously or adiabatically sweep $q_{\rm net}$ from $-\infty$ to $+\infty$ simply by continuously tuning Δ from -190 kHz to 190 kHz with our specially chosen microwave pulses at a power of 8 W. Another advantage of choosing such microwave pulses is to conveniently place the microwave antenna on our apparatus without blocking optical components. To ensure an accurate calibration of $q_{\rm net}$ based on Eq. (2), we measure the nine on-resonance Rabi frequencies Ω daily through monitoring the number of atoms excited by a resonant microwave pulse

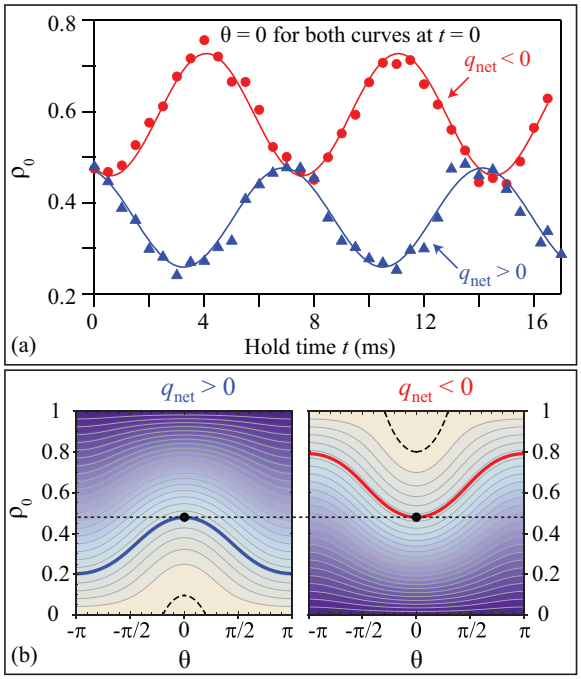

FIG. 2. (Color online) (a) Time evolutions of ρ_0 at $q_{net}/h = +93\text{Hz} > 0$ (solid blue triangles) and $q_{net}/h = -83\text{ Hz} < 0$ (solid red circles) with $m = 0$ and $c/h = 52(1)$ Hz. It is important to note that the two curves start from the same initial state with $\theta|_{t=0} = 0$. Solid lines are sinusoidal fits to the data. (b) Equal-energy contour plots based on Eq. (1) for the two experimental conditions shown in Fig. 2(a), i.e., $q_{net} > 0$ (left) and $q_{net} < 0$ (right). The heavy solid blue and red lines represent the energy of the above two experimental conditions, respectively. The dotted black horizontal line is to emphasize the fact that the above two experiments start with the same initial state which is marked by the solid black circles. Dashed black lines represent the energy of the separatrix between the running and oscillatory phase solutions. Darker colors correspond to lower energies.

to the $F = 2$ state as a function of the pulse duration. A typical example of the Rabi frequency measurement is shown in Fig. 3(a). We find that uncertainties of Ω and q_{net} are $\sim$2% and $\sim$5%, respectively.

III. DYNAMICS OF SPINOR CONDENSATES IN MICROWAVE DRESSING FIELDS

We observe spin oscillations at every given value of q_{net} within a wide range, i.e., $-240\text{ Hz} \leqslant q_{net}/h \leqslant 240\text{ Hz}$. Typical time evolutions of ρ_0 starting with the same nonequilibrium initial state at a negative and a positive q_{net} are shown in Fig. 2(a). We find that these evolutions can be well fit by sinusoidal functions of the similar oscillation period T and amplitude A. Note that the hold time t is kept between zero and $2T < 100$ ms, in order to ensure accurate measurements of spin dynamics and avoid significant atom losses due to the presence of off-resonant microwave pulses. On the other hand, our data in Fig. 2(a) show that the value of $\langle\rho_0\rangle$ drastically differs in the two spin oscillations: $\langle\rho_0\rangle > \rho_0|_{t=0}$ as long as $q_{net} < 0$, while $\langle\rho_0\rangle < \rho_0|_{t=0}$ if $q_{net} > 0$. Here $\langle\rho_0\rangle$ is the average value of ρ_0 over time in a spin oscillation and $\rho_0|_{t=0}$ is the initial value of ρ_0. This phenomenon is observed at every value of q_{net} when spin oscillations start with the same initial state, although the period T and amplitude A change with q_{net}. The above observations agree well with predictions from the mean-field SMA theory [i.e., Eq. (1)] as shown by the heavy solid lines in Fig. 2(b): ρ_0 is limited between $(\rho_0|_{t=0} - 2A)$ and $\rho_0|_{t=0}$ at $q_{net} > 0$, while it is restricted between $\rho_0|_{t=0}$ and $(\rho_0|_{t=0} + 2A)$ at $q_{net} < 0$. We can thus use the phenomenon to conveniently determine the sign of q_{net}, i.e., by comparing the value of $\langle\rho_0\rangle$ of a spin oscillation to the value of $\rho_0|_{t=0}$.

The value of T as a function of q_{net} is then plotted in Fig. 3 for $m = 0$ and $m = 0.2$, which demonstrates two interesting results. First, when $m = 0$, the spin oscillation is harmonic except near the critical values (i.e., $q_{net}/h = \pm 52$ Hz) where the period diverges. This agrees with the predictions derived from Eq. (1), as shown by the dotted red line in Fig. 3. The energy contour E_{sep} where the oscillation becomes anharmonic is defined as a separatrix in phase space. A point on the separatrix satisfies the equation $\dot{\rho}_0 = \dot{\theta} = 0$ according to the mean-field SMA theory. In fact, for our sodium system with $c > 0$, $E_{sep} = q_{net}$ for $q_{net} > 0$, while $E_{sep} = 0$ at $m = 0$ for $q_{net} < 0$. Figure 3 shows that the T versus q_{net} curve is symmetric with respect to the $q_{net} = 0$ axis at $m = 0$. The period T decreases rapidly with increasing $|q_{net}|$ when $|q_{net}|$ is large, which corresponds to the "Zeeman regime" with running phase solutions. In the opposite limit, the period only weakly depends on $|q_{net}|$, which represents the "interaction regime" with oscillatory phase solutions. Here $|q_{net}|$ is the absolute value of q_{net}. The value of θ is (or is not) restricted in the regions with oscillatory (or running) phase solutions. References [8,9] reported observations of the similar phenomena for $q_{net} > 0$ with a $F = 1$ antiferromagnetic spinor condensate; however, they did not access the negative q_{net} region.

Figure 3 also demonstrates a remarkably different relationship between the total magnetization m and the separatrix in phase space: the position of the separatrix moves slightly with m in the positive q_{net} region, while the separatrix quickly disappears when m is away from zero in the negative q_{net} region. Good agreements between our data and the mean-field SMA theory are shown in the inset [Fig. 3(b)] and the main figure in Fig. 3. Interestingly, we find that the spin dynamics which appear in our antiferromagnetic sodium system in the negative q_{net} region exactly resembles what is predicted to occur in a ferromagnetic spinor condensate in the positive q_{net} region [16,17]. Note that $R = q_{net}/c$ is negative in both of these two cases. This observation agrees with an important prediction made by Ref. [17]: The spin-mixing dynamics in $F = 1$ spinor condensates substantially depends on the sign of R. As a matter of fact, our results in the negative q_{net} region are similar to those reported with a $F = 1$ ferromagnetic ^{87}Rb spinor condensate in magnetic fields where $q_{net} > 0$ [1,3]. It is worth noting that our data in Fig. 3 may also be extrapolated to understand the relationship between the separatrix and m in the ferromagnetic Rb system, although this relationship has not been experimentally explored yet. This paper may thus be the first to use only one atomic species to reveal mean-field spin dynamics, especially the different relationship between each separatrix and the magnetization of $F = 1$ antiferromagnetic and ferromagnetic spinor condensates.

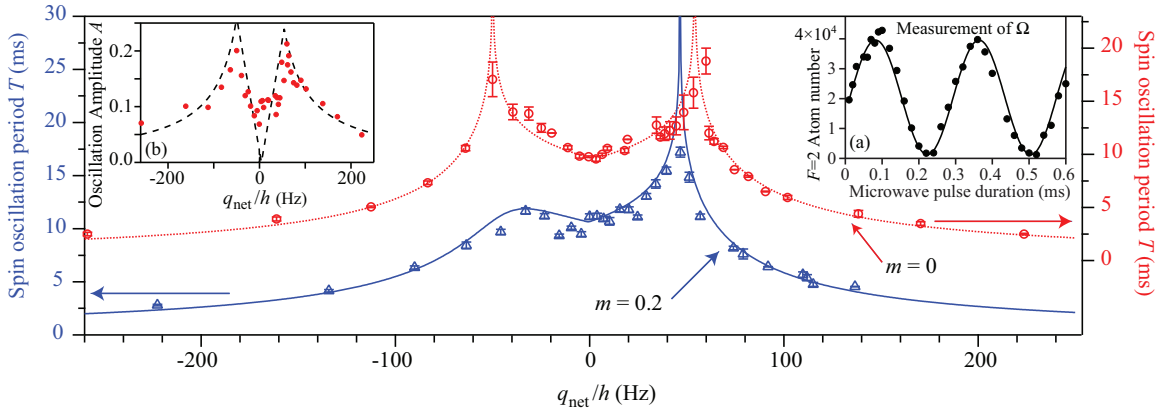

FIG. 3. (Color online) The spin oscillation period as a function of q_{net} for $m = 0$ (open red circles) and $m = 0.2$ (open blue triangles). The lines are fits based on Eq. (1), which yield the following fit parameters: $\rho_0|_{t=0} = 0.48$, $\theta|_{t=0} = 0$, and $c/h = 52(1)$ Hz for $m = 0$ and $\rho_0|_{t=0} = 0.48$, $\theta|_{t=0} = 0$, and $c/h = 47(1)$ Hz for $m = 0.2$. The fit parameters are within the 5% uncertainty of our measurements. Note the different scales of the left and right vertical axes. Inset (a): The number of $F = 2$ atoms excited by a resonant microwave pulse as a function of the pulse duration. The solid line is a sinusoidal fit to extract the on-resonance Rabi frequency Ω of the pulse. Inset (b): Amplitudes A of spin oscillations shown in the main figure as a function of q_{net} at $m = 0$. The dashed black line is a fit based on Eq. (1) with the same set of fit parameters as that applied in the main figure.

IV. CONCLUSION

In conclusion, we have experimentally studied spin dynamics of a sodium spinor condensate in a microwave dressing field. In both negative and positive q_{net} regions, we have observed harmonic spin oscillations and found that the sign of q_{net} can be determined by comparing $\langle\rho_0\rangle$ to $\rho_0|_{t=0}$. Our data also demonstrate that the position of the separatrix in phase space moves slightly with m in the positive q_{net} region, while the separatrix quickly disappears when m is away from zero in the negative q_{net} region. Our data can be well fit by the mean-field theory and agree with one of its important predictions: The spin-mixing dynamics in $F = 1$ spinor condensates substantially depends on the sign of $R = q_{net}/c$. This work uses only one atomic species to reveal mean-field spin dynamics and the different dependence of each separatrix on m in $F = 1$ antiferromagnetic and ferromagnetic spinor condensates. In addition, microwave pulses used in this paper can be applied to cancel out stray magnetic fields and adiabatically sweep q_{net} from $-\infty$ to $+\infty$. This allows studies on interesting but unexplored phenomena at $q_{net} = 0$, for example, realizing a maximally entangled Dicke state with antiferromagnetic spinor condensates through quantum phase transitions [24].

ACKNOWLEDGMENTS

We thank the Army Research Office, Oklahoma Center for the Advancement of Science and Technology, and Oak Ridge Associated Universities for financial support. M.W. thanks the Niblack Research Scholar program.

[1] D. M. Stamper-Kurn and M. Ueda, Rev. Mod. Phys. **85**, 1191 (2013).
[2] Y. Kawaguchi and M. Ueda, Phys. Rep. **520**, 253 (2012).
[3] M.-S. Chang, Q. Qin, W. Zhang, L. You, and M. S. Chapman, Nat. Phys. **1**, 111 (2005).
[4] A. Widera, F. Gerbier, S. Fölling, T. Gericke, O. Mandel, and I. Bloch, New J. Phys. **8**, 152 (2006).
[5] J. Kronjäger, C. Becker, P. Navez, K. Bongs, and K. Sengstock, Phys. Rev. Lett. **97**, 110404 (2006).
[6] H. Schmaljohann, M. Erhard, J. Kronjäger, M. Kottke, S. van Staa, L. Cacciapuoti, J. J. Arlt, K. Bongs, and K. Sengstock, Phys. Rev. Lett. **92**, 040402 (2004).
[7] T. Kuwamoto, K. Araki, T. Eno, and T. Hirano, Phys. Rev. A **69**, 063604 (2004).
[8] A. T. Black, E. Gomez, L. D. Turner, S. Jung, and P. D. Lett, Phys. Rev. Lett. **99**, 070403 (2007).
[9] Y. Liu, S. Jung, S. E. Maxwell, L. D. Turner, E. Tiesinga, and P. D. Lett, Phys. Rev. Lett. **102**, 125301 (2009).
[10] Y. Liu, E. Gomez, S. E. Maxwell, L. D. Turner, E. Tiesinga, and P. D. Lett, Phys. Rev. Lett. **102**, 225301 (2009).
[11] E. M. Bookjans, A. Vinit, and C. Raman, Phys. Rev. Lett. **107**, 195306 (2011).
[12] D. Jacob, L. Shao, V. Corre, T. Zibold, L. De Sarlo, E. Mimoun, J. Dalibard, and F. Gerbier, Phys. Rev. A **86**, 061601 (2012).
[13] L. Chang, Q. Zhai, R. Lu, and L. You, Phys. Rev. Lett. **99**, 080402 (2007).
[14] C. D. Hamley, C. S. Gerving, T. M. Hoang, E. M. Bookjans, and M. S. Chapman, Nature Physics **8**, 305 (2012).
[15] W. Zhang, S. Yi, and L. You, New J. Phys. **5**, 77 (2003).
[16] W. Zhang, D. L. Zhou, M.-S. Chang, M. S. Chapman, and L. You, Phys. Rev. A **72**, 013602 (2005).
[17] A. Lamacraft, Phys. Rev. A **83**, 033605 (2011).
[18] R. Barnett, J. D. Sau, and S. Das Sarma, Phys. Rev. A **82**, 031602 (2010).

[19] F. Gerbier, A. Widera, S. Fölling, O. Mandel, and I. Bloch, Phys. Rev. A **73**, 041602(R) (2006).
[20] S. R. Leslie, J. Guzman, M. Vengalattore, J. D. Sau, M. L. Cohen, and D. M. Stamper-Kurn, Phys. Rev. A **79**, 043631 (2009).
[21] Sabrina R. A. Leslie, Ph.D. thesis, University of California, Berkeley, 2008.
[22] L. Santos, M. Fattori, J. Stuhler, and T. Pfau, Phys. Rev. A **75**, 053606 (2007).
[23] J. Jiang, L. Zhao, M. Webb, N. Jiang, H. Yang, and Y. Liu, Phys. Rev. A **88**, 033620 (2013).
[24] Z. Zhang and L.-M. Duan, Phys. Rev. Lett. **111**, 180401 (2013).

APPENDIX C

Mapping the phase diagram of spinor condensates via adiabatic quantum phase transitions

This appendix includes a reprint of Ref. [122]: J. Jiang, L. Zhao, M. Webb, and Y. Liu, Mapping the phase diagram of spinor condensates via adiabatic quantum phase transitions, Physical Review A **90**, 023610 (2014).

Mapping the phase diagram of spinor condensates via adiabatic quantum phase transitions

J. Jiang, L. Zhao, M. Webb, and Y. Liu*
Department of Physics, Oklahoma State University, Stillwater, Oklahoma 74078, USA
(Received 28 April 2014; published 7 August 2014)

We experimentally study two quantum phase transitions in a sodium spinor condensate immersed in a microwave dressing field. We also demonstrate that many previously unexplored regions in the phase diagram of spinor condensates can be investigated by adiabatically tuning the microwave field across one of the two quantum phase transitions. This method overcomes two major experimental challenges associated with some widely used methods, and is applicable to other atomic species. Agreements between our data and the mean-field theory for spinor Bose gases are also discussed.

DOI: 10.1103/PhysRevA.90.023610 PACS number(s): 67.85.Fg, 03.75.Kk, 03.75.Mn, 05.30.Rt

I. INTRODUCTION

A spinor Bose-Einstein condensate (BEC) is a multicomponent BEC with an additional spin degree of freedom, which has provided exciting opportunities to study quantum magnetism, superfluidity, strong correlations, spin squeezing, and massive entanglement [1–5]. The interesting interactions in spinor BECs are interconversions among multiple spin states and magnetic-field interactions (or microwave dressing field interactions) characterized by $q_{\rm net}$, the net quadratic Zeeman energy. The interplay of these interactions leads to oscillations among multiple spin populations, which has been experimentally confirmed in $F = 1$ ^{23}Na spinor BECs [6–12], and in both $F = 1$ and $F = 2$ ^{87}Rb spinor condensates [13–17].

Several groups demonstrated the mean-field (MF) ground states of spinor BECs by holding BECs in a fixed magnetic field and letting spin population oscillations damp out over a few seconds [8–11]. The required damping time, determined by energy dissipation, may in some cases exceed the BEC lifetime. The exact mechanism involved in energy dissipation requires further study, although it has been shown that energy dissipates much faster in high magnetic fields [10]. For $F = 1$ BECs, a magnetic field introduces only a positive $q_{\rm net}$, while a microwave field has a distinct advantage since it can induce both positive and negative $q_{\rm net}$ [1,7,12,18,19]. As shown in Ref. [12], the same physics model explains spin-mixing dynamics observed in both microwave fields and magnetic fields. One would assume that, if given a long enough exposure to a microwave field, a spinor BEC could also reach its MF ground states. However, experimental studies on ground states of spinor BECs in microwave fields have proven to be very difficult, since these fields are created by near-resonant microwave pulses. Two major experimental challenges associated with microwave fields are atom losses and variations in magnetization m. A different inelastic collision rate in each hyperfine state may be one of the possible reasons to account for these challenges. Microwave-induced changes in both m and the atom number N can be detrimental, especially when a spinor BEC is exposed to a large microwave field for a prolonged time [7,12]. As a result, the phase diagram of $F = 1$ BECs has not been well explored in the $q_{\rm net} \leqslant 0$ region, where applying microwave fields may be necessary.

In this paper, we demonstrate another method to overcome the aforementioned experimental challenges and report the observation of two quantum phase transitions in a spinor BEC. In this method, we quickly prepare an initial equilibrium state at a very high magnetic field to minimize the damping time for spin population oscillations and prevent unnecessary exposure to microwave pulses. Equilibrium states at a desired $q_{\rm net}$ are then created by adiabatically sweeping an additional microwave field. Using this method, we are able to investigate many previously unexplored regions in the phase diagram of antiferromagnetic spinor BECs and observe three distinct quantum phases. Similarly to Refs. [1,2,11], we define three phases in the MF ground states based on ρ_0, the fractional population of the $|F = 1, m_F = 0\rangle$ state: $\rho_0 = 1$, $\rho_0 = 0$, and $0 < \rho_0 < 1$ respectively represent a longitudinal polar phase, an antiferromagnetic (AFM) phase, and a broken-axisymmetry (BA) phase. We observe two quantum phase transitions: one is between a longitudinal polar phase and a BA phase at a fixed positive $q_{\rm net}$, and the other is an AFM-BA phase transition at a given m. We also calculate the energy gap between the ground states and the first excited states in a spinor BEC, which provides an explanation for the feasibility of this method. In addition, spin domains and spatial modes are not observed in our system, and our data can be well fit by predictions of the single spatial-mode approximation (SMA).

The SMA assumes all spin states share the same spatial wave function, which has been a successful model to understand spinor microcondensates [8–13,20–22]. The fractional population ρ_{m_F} and the phase θ_{m_F} of each m_F state are thus independent of position in SMA, and $m = \rho_{+1} - \rho_{-1}$. The spin-dependent interaction energy c is proportional to the atom density, and is positive (or negative) in $F = 1$ antiferromagnetic ^{23}Na (or ferromagnetic ^{87}Rb) spinor BECs. For example, c/h is 40 Hz for our ^{23}Na system in this paper, where h is the Planck constant. After taking into account that N and m are independent of time t and neglecting all constant terms in the Hamiltonian of spinor BECs, we use the SMA to express the BEC energy E and the time evolution of ρ_0 and θ as [1,20,21]

$$E(t) = c\rho_0(t)\{[1-\rho_0(t)] + \sqrt{[1-\rho_0(t)]^2 - m^2}\cos[\theta(t)]\} + q_{\rm net}(t)[1-\rho_0(t)], \quad (1)$$

*yingmei.liu@okstate.edu

$$\dot{\rho}_0 = -\frac{4\pi}{h}\frac{\partial E(t)}{\partial \theta(t)}, \quad \dot{\theta} = \frac{4\pi}{h}\frac{\partial E(t)}{\partial \rho_0(t)}. \tag{2}$$

Here $q_{\rm net} = q_M + q_B$ is the net quadratic Zeeman energy with q_B (or q_M) being induced by magnetic (or microwave dressing) fields. The relative phase among the three m_F spin states is $\theta = \theta_{+1} + \theta_{-1} - 2\theta_0$.

By minimizing Eq. (1), we find ρ_0 in a MF ground state of $F = 1$ spinor BECs is zero if $q_{\rm net} < c(1 \pm \sqrt{1-m^2})$, or equal to one if $m = 0$ and $q_{\rm net} > -c(1 \pm 1)$, or is the root of the following equation at all other $q_{\rm net}$ and m:

$$c\left[1 - 2\rho_0 \pm \frac{(1-2\rho_0)(1-\rho_0) - m^2}{\sqrt{(1-\rho_0)^2 - m^2}}\right] - q_{\rm net} = 0, \tag{3}$$

where the $+$ (or $-$) sign applies to ferromagnetic (or antiferromagnetic) spinor BECs. Typical MF ground states of spin-1 sodium BECs are shown in Figs. 1 and 2. Our experimental phase diagram and the theoretical phase diagram based on Eqs. (1)–(3) are also plotted in Fig. 3.

II. EXPERIMENTAL SETUP

The experimental setup is similar to that elaborated in our recent publications [6,12]. A $F = 1$ BEC of 5×10^4 atoms is created by a forced evaporation in a crossed optical dipole trap. To fully polarize atoms into the $|F = 1, m_F = -1\rangle$ state, we turn on a weak magnetic-field gradient and a low magnetic bias

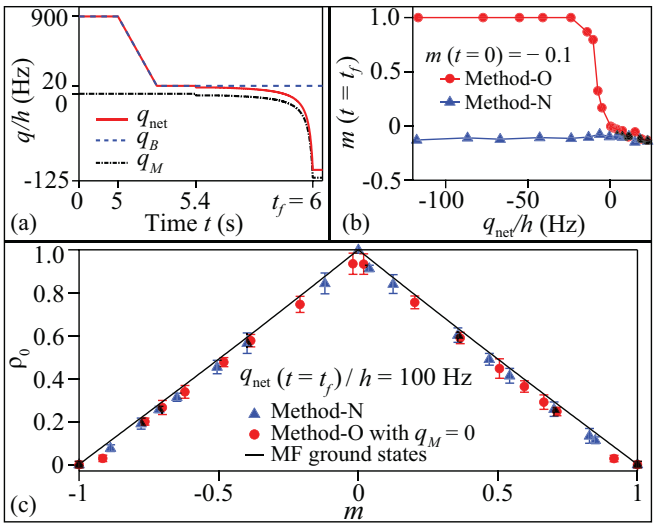

FIG. 1. (Color online) (a) Typical experimental sequence of Method-N, which is our method to create equilibrium states via adiabatically sweeping a microwave field. In this paper -150 Hz $\leqslant q_{\rm net}(t = t_f)/h \leqslant 150$ Hz. All axes are not to scale. (b) m as a function of $q_{\rm net}$ at $t = t_f$ in the two methods starting from the same initial state, i.e., $m(t = 0) = -0.1$. Note that t_f for Method-O in this panel is only 1 s, which is much shorter than the typical hold time for creating equilibrium states. (c) ρ_0 as a function of m at $q_{\rm net}(t = t_f)/h = 100$ Hz in equilibrium states created by the two methods. In this panel, Method-O prepares equilibrium states by holding BECs for 8 s in a high magnetic field, where $q_M = 0$ and $q_B/h = 100$ Hz. The solid black line represents the MF ground states (see text).

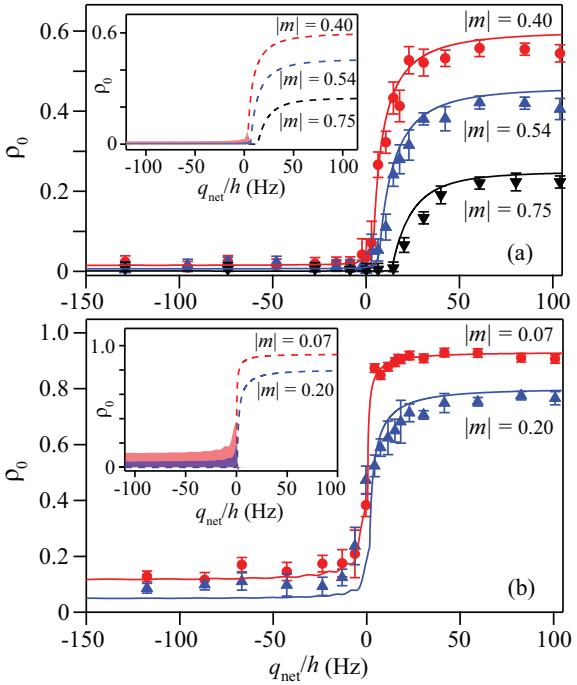

FIG. 2. (Color online) ρ_0 as a function of $q_{\rm net}$ at $t = t_f$ for three large $|m|$ in panel (a) and for two small $|m|$ in panel (b) in equilibrium states created by our Method-N. Solid lines are simulation results for the experimental processes based on Eq. (2) (see text). Insets: dashed lines are the MF ground states. Shaded areas represent the differences between our simulation results and the MF theory at various m. The black, blue, and red colors in panel (a) respectively correspond to results at $|m| = 0.75$, 0.54, and 0.40. The blue and red colors in panel (b) represent results at $|m| = 0.20$ and 0.07, respectively.

field in the forced evaporative cooling process. A resonant rf pulse of a proper amplitude and duration is applied to prepare an initial state with any desired combination of the three m_F states. This moment is defined as the starting point ($t = 0$) of our experimental sequences, as shown in Fig. 1(a). Every sequence ends at $t = t_f$. Populations of multiple spin states are then measured by a standard Stern-Gerlach absorption imaging.

We use two different methods to generate equilibrium states. The Method-O is an old and widely used method, which creates equilibrium states simply by holding a BEC at a fixed $q_{\rm net}$ for a sufficiently long time. We find that the required hold time is longer than 2 s for all positive $q_{\rm net}$ studied in this paper. This old method fails for our system in low magnetic fields (i.e, the small positive $q_{\rm net}$ region), because energy dissipates very slowly and the required hold time is longer than the BEC lifetime ($\sim$10 s) in this region. This old method is more problematic in the negative $q_{\rm net}$ region, because it leads to significant atom losses and detrimental changes in m. In order to overcome these experimental challenges associated with the old method, we have developed another method, Method-N. A comparison of these two methods starting from the same initial state is shown in Fig. 1(b), which highlights the advantage of our method. Note that m and N may not be conserved using the old method, when a microwave field induced by a near-resonant microwave pulse is applied. This is due to the fact that the microwave pulse unavoidably excites some atoms

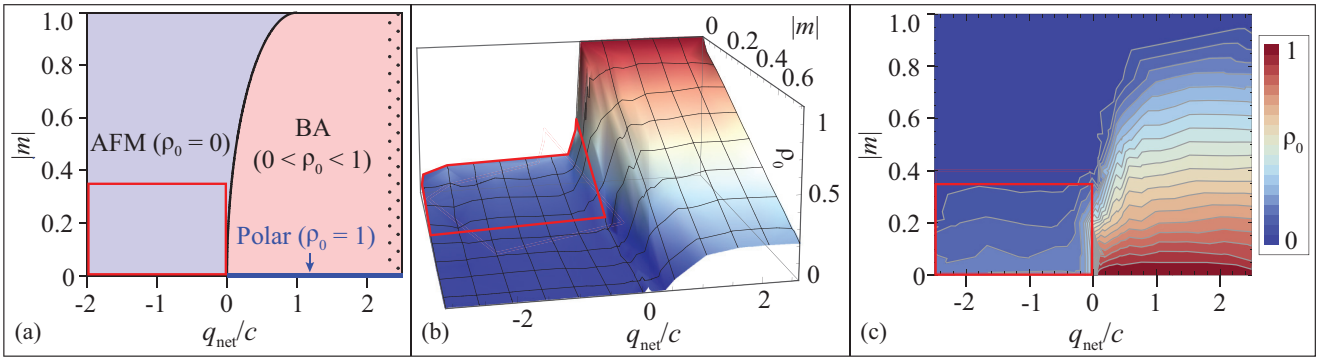

FIG. 3. (Color online) (a) MF phase diagram of spin-1 antiferromagnetic spinor BECs based on Eqs. (1)–(3). Our Method-N works everywhere except in the area marked by red solid lines, while Method-O only applies to the area filled with dots at large q_{net}. Panel (b) [or (c)] is a 3D (or a contour) plot of the experimental phase diagram consisting of data taken by Method-N at 153 different q_{net} and m. Red solid lines in panels (b) and (c) mark the region where our data are different from the MF ground states.

in a $F = 1$ spinor BEC to the $F = 2$ manifold, and more atoms are excited when the microwave pulse has a higher power or a smaller frequency detuning with respect to the $|F = 1\rangle \leftrightarrow |F = 2\rangle$ transitions.

A typical experimental sequence of our Method-N is listed in Fig. 1(a). We first hold a spinor BEC in the optical trap for 5 s at a very high magnetic field with $q_B/h = 900$ Hz. This step ensures the BEC reaches its ground states, since we and Ref. [10] find that the energy dissipation rate quickly increases with q_B. Second, we adiabatically ramp the magnetic field down to $q_B/h = 20$ Hz in 0.1 s, keep q_B at this value for 0.3 s, and then turn on a far off-resonant microwave pulse in 0.1 s. Third, we tune only the frequency of this pulse slowly within 0.5 s, in order to adiabatically sweep its corresponding microwave field to a desired q_{net}. Our approach to characterize microwave dressing fields and the frequency tuning curve for adiabatically sweeping q_{net} within the range of $-\infty$ to $+\infty$ is the same as those illustrated in our previous work [12].

In theory, once a BEC is prepared into its ground state, the BEC may stay in its ground state at each q_{net} when a microwave field is adiabatically ramped [3]. We can thus initially check whether our Method-N is applicable by comparing equilibrium states created by both our method and the old method in a region, $q_{net} \gg 0$, where the old method has been proven to generate the MF ground states [8–11]. Figure 1(c) shows such comparisons made at $q_{net}(t = t_f)/h = 100$ Hz for various magnetization m. The equilibrium states created by the two methods appear to be quite similar, and they stay very close to the same black solid line which represents the MF ground states in Fig. 1(c). This suggests that our method is adiabatic enough to replace the old method in studies related to the BEC phase diagrams. We also find that a spinor BEC returns to its original state when we ramp a microwave field from $q_M = 0$ to a fixed nonzero q_M and then back to $q_M = 0$ with Method-N, although this observation may not be sufficient to prove the process is adiabatic.

III. MAPPING THE PHASE DIAGRAM OF SPINOR CONDENSATES

We then apply our method to a much wider range of q_{net} and m, especially in the negative and small positive q_{net} regions which cannot be easily explored by the old method, as shown in Fig. 2. We find two interesting results from this figure. First, our data in Fig. 2(a) show a quantum phase transition between a BA phase and an AFM phase at each m. This BA-AFM phase transition appears to occur at a larger q_{net} when $|m|$ gets bigger, which can be well explained by the MF theory [i.e., dashed lines in the inset in Fig. 2(a)]. Another interesting result is that Method-N does allow us to access many previously unexplored regions in the phase diagram, although there is a visible discrepancy between the MF ground states and our data at a small m in the negative q_{net} region, as shown in Fig. 2(b). To understand this phenomenon, we simulate the experimental processes based on Eq. (2) by taking a proper formula to account for the time evolution of q_{net} during an adiabatic ramping of microwave fields. Figure 2 shows that the simulation results can well resemble the experimental data, while the differences between our simulation results and the MF ground states are emphasized by a shaded area at each m in the two insets in Fig. 2. These shaded areas appear to slowly increase in the negative q_{net} region when $|m|$ approaches zero. In other words, the discrepancy between our data and the MF ground states only becomes noticeable at a small $|m|$ in the negative q_{net} region. Due to this discrepancy, we find that the predicted quantum phase transition between an AFM phase and a longitudinal polar phase at $m = 0$ and $q_{net} = 0$ is replaced by a transition between a BA phase and a longitudinal polar phase. Since our experimental resolution for ρ_0 is around 0.02, Fig. 2 implies that our method is sufficient to map out the BEC phase diagram in the positive q_{net} region at each m, and in the negative q_{net} as long as $|m| \geqslant 0.4$.

Figure 3 clearly summarizes the improvement provided by Method-N, after comparing the theoretical MF phase diagram to an experimental phase diagram consisting of our data taken at 153 different q_{net} and m. All three predicted phases (i.e., an AFM, a polar, and a BA phase), an AFM-BA phase transition at a fixed m, and a transition between a longitudinal polar phase and a BA phase at a certain positive q_{net} are shown in the experimental phase diagram. Good agreement between our data and the MF ground states can be found everywhere in the two phase diagrams except in the region where $|m| < 0.4$ and $q_{net} < 0$. This problematic region has been marked by red solid lines in Fig. 3. Ramping microwave fields at a slower rate should help to diminish this problematic region; however, a slower rate requires holding a BEC in microwave

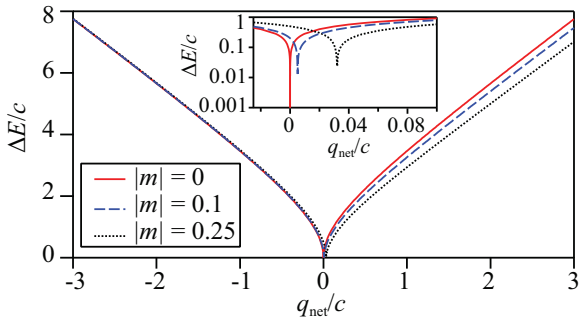

FIG. 4. (Color online) Energy gap ΔE in the unit of c as a function of $q_{\rm net}/c$ at three $|m|$ based on Eq. (4) (see text). Inset: a magnified view of the main figure in the region of $-0.025 < q_{\rm net}/c < 0.1$.

fields for a longer time and thus inevitably leads to more atom losses and a bigger change in m. In fact, we tried quite a few different microwave ramping rates, but none of them enabled a spinor BEC to reach its MF ground states when m is very small and $q_{\rm net} < 0$. The same problem also exists in simulation results: our simulation program cannot suggest a reasonable ramping rate to ensure an adiabatic sweep of $q_{\rm net}$ across a phase transition for a small m.

To understand this problem, we need to find the exact value of ΔE, the energy gap between the ground state and the first excited state in spinor BECs. Similar to Ref. [3], we can describe a spinor BEC in the Fock space. The spin-dependent part of the Hamiltonian in a $F = 1$ spinor BEC can be expressed as [3,20,23]

$$H = \sum_{i,j,k,l=-1}^{1} \left[q_{\rm net} k^2 a_k^\dagger a_k + \frac{c}{2} \sum_{\gamma} a_k^\dagger a_i^\dagger (F_\gamma)_{ij} (F_\gamma)_{kl} a_j a_l \right], \tag{4}$$

since m is conserved and there are only a finite number of atoms in a typical equilibrium state studied in this paper. Here a_k ($a_k^\dagger$) is the annihilation (creation) operator of the $|F = 1, m_F = k\rangle$ state, and $F_{\gamma=x,y,z}$ are the spin-1 matrices. By diagonalizing the Hamiltonian in Eq. (4) and performing an exact numerical many-body calculation, we can find the energy gaps. Figure 4 shows numerical examples of ΔE at three typical $|m|$. It appears that ΔE drastically drops by more than three orders of magnitude when $|m|$ and $q_{\rm net}$ approach zero, as shown in the inset in Fig. 4. Therefore, it is not surprising that adiabatically sweeping $q_{\rm net}$ across a quantum phase transition point is not feasible at a very small m, especially at $m = 0$. We can also calculate ΔE_e, the energy gap between the highest eigenstate and the second highest eigenstate of Eq. (4). The minimal value of ΔE_e at $m = 0$ appears to be larger than that of ΔE (the energy gap associated with the ground state) at $m = 0.75$. In other words, adiabatically sweeping $q_{\rm net}$ across a quantum phase transition demonstrated in this paper may be useful for confirming other important predictions, for instance, realizing massive entanglement in the highest eigenstate of antiferromagnetic spinor BECs [3].

IV. CONCLUSION

In conclusion, we have observed two types of quantum phase transitions in a spin-1 antiferromagnetic spinor BEC, and developed another method to create the equilibrium states of spinor condensates by adiabatically sweeping a microwave field. The biggest advantage of this method is to avoid significant atom losses and detrimental changes in m at large microwave fields. We have demonstrated that this method enables us to conduct an experimental study on the phase diagram of antiferromagnetic spinor BECs at various m in the negative $q_{\rm net}$ region. Our experimental phase diagram agrees with the MF theory for all m in the positive $q_{\rm net}$ region and for all negative $q_{\rm net}$ as long as $|m| \geqslant 0.4$. This method can be applied to other atomic species and may be helpful to discover interesting quantum phase transitions in other systems, for example, revealing a BA-AFM quantum phase transition in $F = 1$ ^{87}Rb spinor BECs at a negative $q_{\rm net}$.

ACKNOWLEDGMENTS

We thank the Army Research Office, the National Science Foundation, and the Oklahoma Center for the Advancement of Science and Technology for financial support. M.W. thanks the Niblack Research Scholar program.

[1] D. M. Stamper-Kurn and M. Ueda, Rev. Mod. Phys. **85**, 1191 (2013).
[2] Y. Kawaguchi and M. Ueda, Phys. Rep. **520**, 253 (2012).
[3] Z. Zhang and L.-M. Duan, Phys. Rev. Lett. **111**, 180401 (2013).
[4] T. M. Hoang, C. S. Gerving, B. J. Land, M. Anquez, C. D. Hamley, and M. S. Chapman, Phys. Rev. Lett. **111**, 090403 (2013).
[5] C. D. Hamley, C. S. Gerving, T. M. Hoang, E. M. Bookjans, and M. S. Chapman, Nat. Phys. **8**, 305 (2012).
[6] J. Jiang, L. Zhao, M. Webb, N. Jiang, H. Yang, and Y. Liu, Phys. Rev. A **88**, 033620 (2013).
[7] E. M. Bookjans, A. Vinit, and C. Raman, Phys. Rev. Lett. **107**, 195306 (2011).
[8] A. T. Black, E. Gomez, L. D. Turner, S. Jung, and P. D. Lett, Phys. Rev. Lett. **99**, 070403 (2007).
[9] Y. Liu, S. Jung, S. E. Maxwell, L. D. Turner, E. Tiesinga, and P. D. Lett, Phys. Rev. Lett. **102**, 125301 (2009).
[10] Y. Liu, E. Gomez, S. E. Maxwell, L. D. Turner, E. Tiesinga, and P. D. Lett, Phys. Rev. Lett. **102**, 225301 (2009).
[11] D. Jacob, L. Shao, V. Corre, T. Zibold, L. De Sarlo, E. Mimoun, J. Dalibard, and F. Gerbier, Phys. Rev. A **86**, 061601 (2012).
[12] L. Zhao, J. Jiang, T. Tang, M. Webb, and Y. Liu, Phys. Rev. A **89**, 023608 (2014).
[13] M.-S. Chang, Q. Qin, W. Zhang, L. You, and M. S. Chapman, Nat. Phys. **1**, 111 (2005).
[14] A. Widera, F. Gerbier, S. Fölling, T. Gericke, O. Mandel, and I. Bloch, New J. Phys. **8**, 152 (2006).
[15] J. Kronjäger, C. Becker, P. Navez, K. Bongs, and K. Sengstock, Phys. Rev. Lett. **97**, 110404 (2006).

[16] H. Schmaljohann, M. Erhard, J. Kronjäger, M. Kottke, S. van Staa, L. Cacciapuoti, J. J. Arlt, K. Bongs, and K. Sengstock, Phys. Rev. Lett. **92**, 040402 (2004).
[17] T. Kuwamoto, K. Araki, T. Eno, and T. Hirano, Phys. Rev. A **69**, 063604 (2004).
[18] F. Gerbier, A. Widera, S. Fölling, O. Mandel, and I. Bloch, Phys. Rev. A **73**, 041602(R) (2006).
[19] S. R. Leslie, J. Guzman, M. Vengalattore, J. D. Sau, M. L. Cohen, and D. M. Stamper-Kurn, Phys. Rev. A **79**, 043631 (2009).
[20] W. Zhang, D. L. Zhou, M.-S. Chang, M. S. Chapman, and L. You, Phys. Rev. A **72**, 013602 (2005).
[21] Y. Kawaguchi, H. Saito, K. Kudo, and M. Ueda, Phys. Rev. A **82**, 043627 (2010).
[22] A. Lamacraft, Phys. Rev. A **83**, 033605 (2011).
[23] W. Zhang, S. Yi, and L. You, New J. Phys. **5**, 77 (2003).

APPENDIX D

Antiferromagnetic Spinor Condensates in a Two-Dimensional Optical Lattice

This appendix includes a reprint of Ref. [128]: L. Zhao, J. Jiang, T. Tang, M. Webb, and Y. Liu, Antiferromagnetic Spinor Condensates in a Two-Dimensional Optical Lattice, Physical Review Letters, **114**, 225302 (2015).

Antiferromagnetic Spinor Condensates in a Two-Dimensional Optical Lattice

L. Zhao, J. Jiang, T. Tang, M. Webb, and Y. Liu*
Department of Physics, Oklahoma State University, Stillwater, Oklahoma 74078, USA
(Received 30 December 2014; published 4 June 2015)

We experimentally demonstrate that spin dynamics and the phase diagram of spinor condensates can be conveniently tuned by a two-dimensional optical lattice. Spin population oscillations and a lattice-tuned separatrix in phase space are observed in every lattice where a substantial superfluid fraction exists. In a sufficiently deep lattice, we observe a phase transition from a longitudinal polar phase to a broken-axisymmetry phase in steady states of lattice-confined spinor condensates. The steady states are found to depend sigmoidally on the lattice depth and exponentially on the magnetic field. We also introduce a phenomenological model that semiquantitatively describes our data without adjustable parameters.

DOI: 10.1103/PhysRevLett.114.225302 PACS numbers: 67.85.Fg, 03.75.Kk, 03.75.Mn, 05.30.Rt

A spinor Bose-Einstein condensate (BEC) confined in optical lattices has attracted much attention for its abilities to systematically study, verify, and optimize condensed matter models [1–3]. An optical lattice is a versatile technique to enhance interatomic interactions and control the mobility of atoms [4–6]. Atoms held in shallow lattices can tunnel freely among lattice sites and form a superfluid (SF) phase. The tunneling rate is suppressed while the on-site atom-atom interaction increases in deeper lattices. This may result in a transition from a SF phase to a Mott-insulator (MI) phase at a critical lattice depth, which has been confirmed in various scalar BEC systems [4–7]. In contrast to scalar BECs, spinor BECs have unique advantages due to an additional spin degree of freedom. The predicted SF-MI phase transition is remarkably different in lattice-trapped antiferromagnetic spinor BECs; i.e., the transition may be first (second) order around the tip of each Mott lobe for an even (odd) occupation number [1,8].

Spin-mixing dynamics and phase diagrams of spinor BECs in free space, due to the interplay of the spin-dependent interaction U_2 and the quadratic Zeeman energy q_B, have been well studied using sodium [9–16] and rubidium atoms [17–20]. Known phenomena in spin-1 spinor BECs include spin population oscillations resulting from coherent interconversions among two $|F=1,m_F=0\rangle$ atoms, one $|F=1,m_F=+1\rangle$ atom, and one $|F=1,m_F=-1\rangle$ atom. Spin oscillations are harmonic except near a separatrix in phase space where the oscillation period diverges. The separatrix sets a boundary between the U_2-dominated region and the q_B-dominated region [1,15]. Richer spin dynamics are predicted in lattice-trapped spinor BECs, which allow for many immediate applications. These include constructing a novel quantum-phase-revival spectroscopy driven by a competition between U_2 and spin-independent interaction U_0, understanding quantum magnetism, and realizing massive entanglement [1,3]. However, dynamics of lattice-trapped spinor BECs remain less explored, and most of such experimental studies have been conducted in ferromagnetic ^{87}Rb spinor BECs [21–24].

In this Letter, we experimentally demonstrate that a two-dimensional (2D) optical lattice can conveniently tune spin dynamics of $F=1$ antiferromagnetic spinor BECs. We find that the properties of spinor BECs remain largely unchanged in the presence of a shallow lattice, while sufficiently deep lattices introduce some interesting changes. First, in every lattice depth u_L that supports a substantial superfluid fraction, we observe spin population oscillations after taking spinor BECs out of equilibrium at a fixed q_B. Second, we demonstrate a lattice-tuned separatrix in phase space, and explain it using lattice-enhanced spin-dependent interactions. Another remarkable result is our observation of a phase transition from a longitudinal polar (LP) phase to a broken-axisymmetry (BA) phase in steady states of spinor BECs confined by sufficiently deep lattices [25]. We find the steady states depend exponentially on q_B and sigmoidally on u_L, which agrees with our phenomenological model.

We create a BEC of 7×10^4 sodium atoms fully polarized into the $|F=1,m_F=-1\rangle$ state in a crossed optical trap similar to our previous work [14]. To adiabatically load the BEC into a 2D lattice, we decompress the optical trap to a value which minimizes intraband excitations and ensures approximately constant Thomas-Fermi radii while linearly ramping the lattice potential within $t_{\mathrm{ramp}}>40$ ms. We construct the 2D lattice in the $\hat{x}$-$\hat{y}$ horizontal plane using two linearly polarized beams which originate from a single-mode laser at $\lambda_L=1064$ nm, have a waist of $\sim$90 μm at the condensate, and are retroreflected to form standing waves. To eliminate cross interference between different beams, the two lattice beams are frequency shifted by 20 MHz with respect to each other. u_L is calibrated using Kapitza-Dirac diffraction patterns. All lattice depths studied in this Letter are kept below $15.0(8)E_R$ to avoid SF-MI phase transitions and thus maintain a sufficient superfluid fraction in our system.

Here $E_R = h^2k_L^2/(8\pi^2 M)$ is recoil energy, $k_L = 2\pi/\lambda_L$ is the lattice wave number, M is the atomic mass, and h is the Planck constant. We apply a resonant rf pulse of a proper amplitude and duration to lattice-trapped BECs for preparing an initial state with any desired combination of the three m_F states at $q_B/h = 42$ Hz, and then quench q_B to a desired value. After holding atoms for a variable time duration $t_{\rm hold}$, we abruptly switch off all lattice and trapping potentials. The fractional population of each m_F state, ρ_{m_F}, is measured with Stern-Gerlach absorption imaging after a certain time of flight $t_{\rm TOF}$. The initial ρ_0 is 0.46, the initial relative phase among the three spin states is zero, and $t_{\rm TOF}$ is 6 ms unless otherwise specified. The total magnetization $m = \rho_{+1} - \rho_{-1}$ appears to be conserved in every time evolution studied in this Letter.

In the presence of a shallow lattice of $u_L < 5E_R$, we observe spin population oscillations similar to those occurring in free space, as shown in Fig. 1. Sharp interference peaks are observed after we release BECs from the shallow lattice [see Fig. 1(a) inset], which indicates coherence and superfluid behavior in the system. As the lattice is made deeper, the separatrix position shifts to a much higher q_B, and the spin oscillations damp out more quickly (especially in the vicinity of each separatrix). These fast damped oscillations make it hard to extract oscillation periods and precisely locate each separatrix even at a moderate u_L (e.g., $4.5E_R$), as shown in Fig. 1(b). A typical anharmonic spin oscillation near a separatrix is shown in the inset in Fig. 1(b). We find our system can be understood by two models: the Bose-Hubbard (BH) model discussed in Ref. [3] for $u_L > 5E_R$, and the single-spatial mode approximation (SMA) defined in Ref. [26] for $u_L < 5E_R$. The BH model has three important terms: U_0, U_2, and the tunneling energy J among adjacent lattice sites. U_2 is proportional to the atomic density in each lattice site, and is positive (negative) in $F = 1$ ^{23}Na (^{87}Rb) BECs. In fact, $U_2/U_0 \simeq 0.04$ for our ^{23}Na system [3], and $U_2 \simeq q_B$ at each separatrix for the initial state studied in Fig. 1 [15]. The observed lattice-tuned separatrix in phase space (i.e., the separatrix position shifts with u_L) is thus mainly due to the fact that U_2 greatly increases with u_L. Figure 1(b) shows a good numerical example: U_2/h is increased from 14 Hz to 32 Hz by changing u_L from $2.5E_R$ to $4.5E_R$.

Spin oscillations completely damp out and spinor BECs reach their steady states when $t_{\rm hold}$ is long enough [see Fig. 2(a)]. Sufficiently deep lattices are found to bring some interesting changes to the steady states. Figure 2(a) demonstrates one of such changes: once u_L is sufficiently large, the steady states undergo a phase transition from a LP phase (where $\rho_0 = 1$) to a BA phase (where $0 < \rho_0 < 1$) at $m = 0$. We repeat the same measurements with only one parameter changed, i.e., by blocking the retroreflected path of each lattice beam to eliminate standing waves and construct a crossed optical dipole trap (ODT). Its resulting

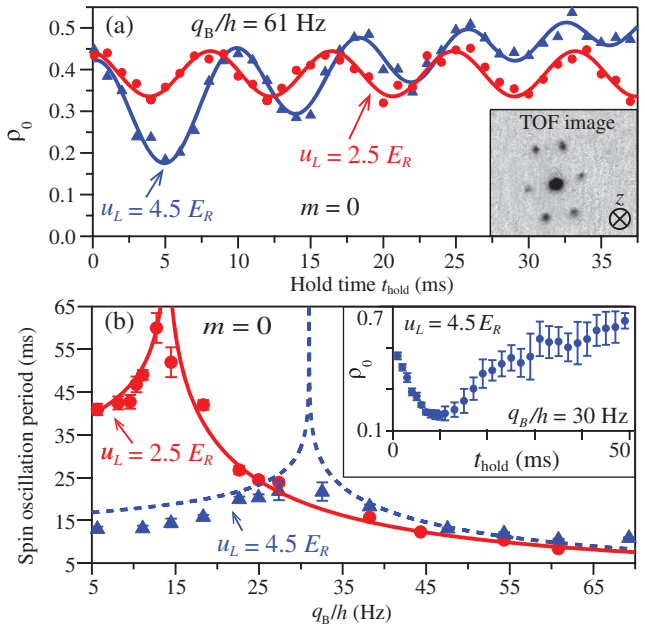

FIG. 1 (color online). (a) Time evolutions of ρ_0 when $u_L = 4.5E_R$ (triangles) and $2.5E_R$ (circles). Solid lines are sinusoidal fits to extract oscillation periods. Inset: a TOF image taken along the vertical direction (z axis) at $t_{\rm TOF} = 5$ ms. (b) Oscillation period versus q_B. Lines are fits based on SMA. Inset: time evolution of ρ_0 near a separatrix. Uncertainties are extracted from 15–20 repeated Stern-Gerlach measurements. Large uncertainties of ρ_0 near the separatrix may result from shot-to-shot fluctuations, similar to Ref. [11].

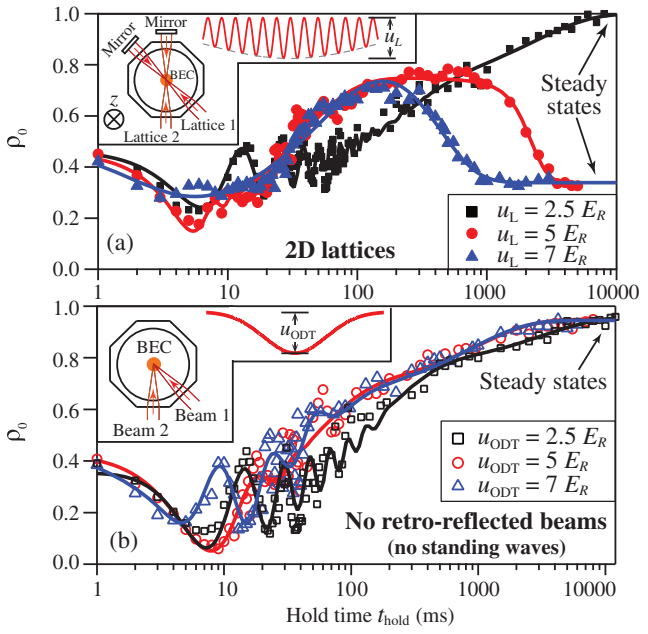

FIG. 2 (color online). (a) Time evolutions of ρ_0 at $q_B/h = 42$ Hz and $m = 0$. Inset: a schematic of our lattice setup and an illustration of the resulting lattice potential. Lines are fits to guide the eye (see Ref. [27]). (b) Similar to panel (a) except that each beam is not retroreflected.

trap depth is u_{ODT}, as illustrated in Fig. 2(b) inset. The power of every beam in Fig. 2(b) is 4 times of that in Fig. 2(a) to ensure $u_L = u_{\mathrm{ODT}}$. Our data in Fig. 2(b) show that spinor BECs at $m = 0$ always reach the LP phase when there are no standing waves. The dramatically different results shown in Figs. 2(a) and 2(b) imply a necessity to understand this LP-BA transition with lattice-modified band structures.

We then study spin oscillations and steady states within a much wider range of u_L and m. Steady states appear to depend sigmoidally on u_L at a fixed q_B, as shown in Fig. 3(a). The inset in Fig. 3(a) demonstrates another surprising result: the observed relationship between ρ_0 and m in steady states at a sufficiently large u_L is well fit by $\rho_0 = (1 - |m|)/3$, which is drastically different from a well-known mean-field prediction (i.e., $\rho_0^{D\approx 0}$ as illustrated by the black dotted line) [25]. This mean-field prediction assumes quantum depletion D is negligible, where D represents the fraction of atoms situated in non-zero momentum states. Based on Bogoliubov theory, the $D \approx 0$ assumption is correct in free space and very shallow lattices for our system [7]. We extract D from TOF images (see Fig. 3 and Ref. [28]) and confirm $D < 5\%$ at $u_L \leq 3E_R$. Note that the trapping frequency in each lattice site is much bigger than U_0/h. Our TOF images thus reflect the momentum distribution at the instant of the lattice release and enable us to directly measure D [7].

We also find that D increases with t_{hold} and u_L, and approaches one in steady states when $u_L > 10E_R$, as shown in Fig. 3(d). This lattice-enhanced quantum depletion mainly results from the lattice-flatten dispersion relation and lattice-enhanced interactions, and was originally observed in scalar BEC systems [7]. We develop one phenomenological model to incorporate the observed D and find this model can semiquantitatively describe our data without adjustable parameters, as shown in Figs. 3(a) and 4(a). In this model, the steady states are determined by a comparison between $T(\mathbf{k}, m_F = 0)$ and $T(0, m_F = \pm 1)$, where $T(\mathbf{k}, m_F)$ is the dispersion relation of the m_F state and $\mathbf{k}$ is the atom's quasimomentum. Figure 4(b) illustrates two example comparisons. Note that only the first Brillouin zone is considered, since the population in higher bands is negligible. Based on Refs. [5–7], we calculate $T(\mathbf{k}, m_F)$ as follows:

$$T(\mathbf{k}, m_F) = 4J \sum_{\alpha=x,y} \sin^2\left(\frac{\pi k_\alpha}{2k_L}\right) + E_R \frac{k_z^2}{k_L^2} + q_B m_F^2, \quad (1)$$

where a uniform density function is applied along the vertical direction without a lattice (the z axis), and J is calculated using a Wannier density function along each of the two horizontal directions with lattices. The linear Zeeman effect is ignored because it remains unchanged in coherent interconversions.

We divide $T(\mathbf{k}, m_F = 0)$ into two regions based on $T(0, m_F = \pm 1)$, i.e., set the boundary of the two regions at $\mathbf{k}_c$ which satisfies $T(\mathbf{k}_c, m_F = 0) = T(0, m_F = \pm 1)$, as marked by vertical dotted lines in Fig. 4(b). The dispersion relations are significantly flattened as u_L increases, since the predicted width of the first band is $\sim 4J$ and J exponentially reduces with u_L [6,7]. To clearly explain our model using the dispersion relations shown in Fig. 4(b), we only consider $m = 0$ and $k_y = k_z = 0$ in this paragraph. In region 1 where $0 \leq |k_x| < |\mathbf{k}_c|$, atoms in the $m_F = 0$ state always have energy smaller than those in the $m_F = \pm 1$ states. The steady states should thus be the $m_F = 0$ state (i.e., $\rho_0 = 1$), which equals $\rho_0^{D\approx 0}$. When D is big enough, atoms start to occupy region 2 where $|\mathbf{k}_c| \leq |k_x| \leq k_L$. The $m_F = 0$ atoms in region 2 are degenerate with $m_F = \pm 1$ atoms at certain other momenta. This degeneracy may account for the phenomenological relationship shown in Fig. 3(a), i.e., $\rho_0 = 1/3$ in steady states at a big u_L. Our data and the dispersion relations thus suggest that atoms in steady states may be equally distributed among the three m_F states at a big enough D.

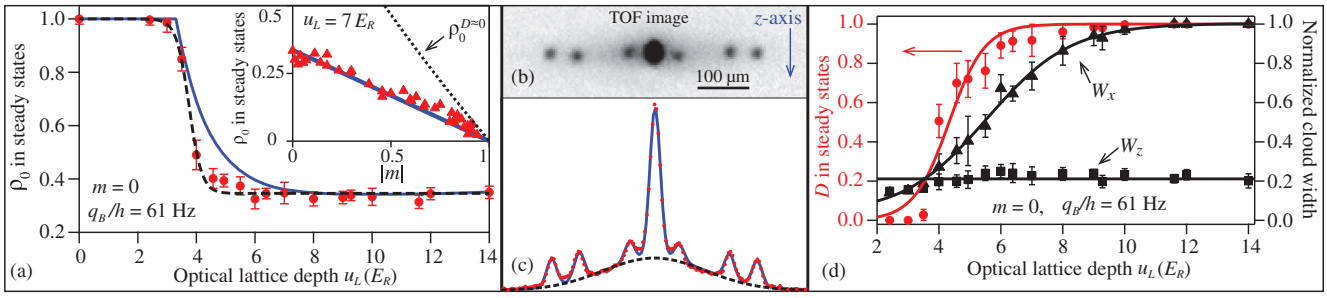

FIG. 3 (color online). (a) ρ_0 in steady states as a function of u_L (main figure) and $|m|$ (inset figure). Solid lines are predictions derived from Eq. (2). The dashed and dotted lines, respectively, represent a sigmoidal fit and $\rho_0^{D\approx 0}$ (see Ref. [25]). (b) A typical TOF image. Using method 1, the extracted D is 53% from this image (see Ref. [28]). (c) Density profile (red dotted line) of the image shown in panel (b) through all interference peaks. Using method 2 (blue solid line), the extracted D is 52.5% (see Ref. [28]). The black dashed line highlights the quantum depleted fraction. (d) W_x (triangles), W_z (squares), and D (circles) in steady states as a function of u_L. The widths are normalized by k_L. Lines are respectively sigmoid fits to W_x and D, and a linear fit to W_z.

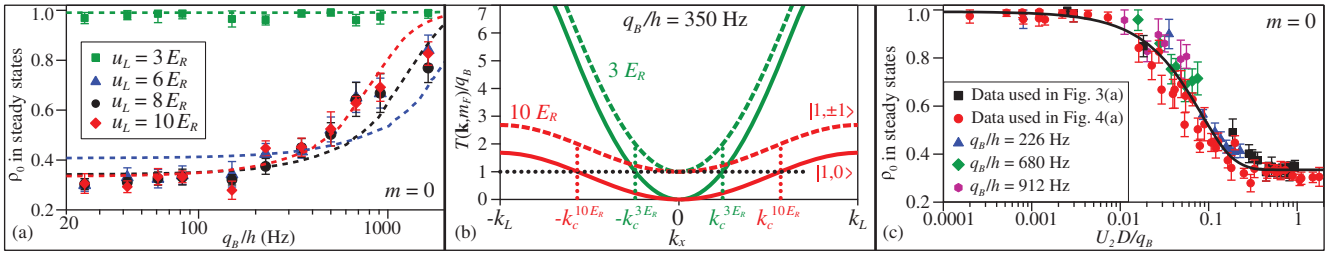

FIG. 4 (color online). (a) ρ_0 in steady states as a function of q_B. Dashed lines are predictions derived from Eq. (2). Green, blue, black, and red colors, respectively, represent results at $u_L = 3$, 6, 8, and $10E_R$. (b) Dispersion relations normalized by q_B as a function of k_x when $k_y = k_z = 0$. Solid (dashed) lines represent results of the $m_F = 0$ ($m_F = \pm 1$) states. The black horizontal dotted line marks $T(\mathbf{k}, m_F) = q_B$, and vertical dotted lines mark boundaries between region 1 and region 2 at $u_L = 3$ and $10E_R$. (c) ρ_0 in steady states versus U_2D/q_B. Black, red, blue, green, and purple colors, respectively, represent data used in Figs. 3(a) and 4(a), and additional data taken at $q_B/h = 226$, 680, and 912 Hz. The solid line is a sigmoid fit.

We can apply similar discussions and our model to all nonzero m. Thus ρ_0 in the steady states is expressed as

$$\rho_0 \approx \int_{\text{region 1}} n(\mathbf{k})\rho_0^{D\approx 0} d\mathbf{k} + \int_{\text{region 2}} n(\mathbf{k})\frac{1-|m|}{3} d\mathbf{k}. \quad (2)$$

The normalized atomic density in steady states, $n(\mathbf{k})$, is calculated by the following phenomenological formula: $n(\mathbf{k}) = (1-D)\delta_{\mathbf{k}} + D\exp[-(k_x^2/W_x^2 + k_y^2/W_y^2 + k_z^2/W_z^2)/2]/A$, where W_x and W_z are the half widths of a 2D Gaussian fit to a TOF distribution within the first Brillouin zone, $W_y = W_x$, A is a normalization factor, and δ is a Dirac-delta function [29]. Figure 3(d) shows that W_x and D sigmoidally increase with u_L, and saturate at their peak values when $u_L > 10E_R$; i.e., atoms occupy all available states and quantum depletion saturates the first Brillouin zone in a deep lattice. In contrast, W_z appears to be independent of u_L, which implies a constant system temperature.

The observed sigmoidal dependence of steady states on u_L and the exponential dependence on q_B can be explained by our model [Eq. (2)], as respectively shown in Figs. 3(a) and 4(a). Quantitative agreements between our model and data are found everywhere except in high magnetic fields where $q_B/h > 1000$ Hz, and in a lattice where $4E_R \le u_L \le 6E_R$. Limited imaging resolutions and heating induced by an extra magnetic coil in creating high q_B may both contribute to the discrepancy.

To better understand the LP-BA phase transition, we plot ρ_0 versus U_2D/q_B (a dimensionless ratio) at $m = 0$ in Fig. 4(c). Here U_2/q_B is the key factor determining the spinor dynamics in free space, D represents the lattice-induced effect, and both D and U_2 increase with the spin-independent interaction U_0. Two interesting results are found in Fig. 4(c): all 80 data points taken at very different u_L and q_B are fit by one sigmoid function; and the critical point of the LP-BA transition appears to be $U_2D/q_B \sim 0.01$. (In contrast, each predicted separatrix locates around $U_2/q_B = 1$ based on SMA and parameters studied in Fig. 4.) The LP-BA transition may thus result from a competition between q_B and the "effective" interaction U_2D; i.e., regions with strong enough interactions may prefer the BA phase. In principle, we can verify this using other methods which can efficiently tune interatomic interactions, e.g., via Feshbach resonances.

In conclusion, we have conducted the first experimental study on dynamics and the phase diagram of lattice-trapped antiferromagnetic spinor BECs. A lattice-tuned separatrix in phase space and the LP-BA phase transition in steady states have been observed. We have found that ρ_0, D, and thus the main findings of this Letter are nearly independent of t_{TOF}. We have also developed a phenomenological model that describes our data without adjustable parameters.

We thank the Army Research Office and the National Science Foundation for financial support.

*yingmei.liu@okstate.edu

[1] D. M. Stamper-Kurn and M. Ueda, Rev. Mod. Phys. **85**, 1191 (2013).
[2] Y. Kawaguchi and M. Ueda, Phys. Rep. **520**, 253 (2012).
[3] K. W. Mahmud and E. Tiesinga, Phys. Rev. A **88**, 023602 (2013).
[4] M. Greiner, O. Mandel, T. Esslinger, T. W. Hasch, and I. Bloch, Nature (London) **415**, 39 (2002).
[5] D. Jaksch, C. Bruder, J. I. Cirac, C. W. Gardiner, and P. Zoller, Phys. Rev. Lett. **81**, 3108 (1998).
[6] M. P. A. Fisher, P. B. Weichman, G. Grinstein, and D. S. Fisher, Phys. Rev. B **40**, 546 (1989).
[7] K. Xu, Y. Liu, D. E. Miller, J. K. Chin, W. Setiawan, and W. Ketterle, Phys. Rev. Lett. **96**, 180405 (2006).
[8] G. G. Batrouni, V. G. Rousseau, and R. T. Scalettar, Phys. Rev. Lett. **102**, 140402 (2009).
[9] A. T. Black, E. Gomez, L. D. Turner, S. Jung, and P. D. Lett, Phys. Rev. Lett. **99**, 070403 (2007).
[10] Y. Liu, S. Jung, S. E. Maxwell, L. D. Turner, E. Tiesinga, and P. D. Lett, Phys. Rev. Lett. **102**, 125301 (2009).
[11] Y. Liu, E. Gomez, S. E. Maxwell, L. D. Turner, E. Tiesinga, and P. D. Lett, Phys. Rev. Lett. **102**, 225301 (2009).

[12] E. M. Bookjans, A. Vinit, and C. Raman, Phys. Rev. Lett. **107**, 195306 (2011).
[13] D. Jacob, L. Shao, V. Corre, T. Zibold, L. De Sarlo, E. Mimoun, J. Dalibard, and F. Gerbier, Phys. Rev. A **86**, 061601(R) (2012).
[14] J. Jiang, L. Zhao, M. Webb, N. Jiang, H. Yang, and Y. Liu, Phys. Rev. A **88**, 033620 (2013).
[15] L. Zhao, J. Jiang, T. Tang, M. Webb, and Y. Liu, Phys. Rev. A **89**, 023608 (2014).
[16] J. Jiang, L. Zhao, M. Webb, and Y. Liu, Phys. Rev. A **90**, 023610 (2014).
[17] M.-S. Chang, Q. Qin, W. Zhang, L. You, and M. S. Chapman, Nat. Phys. **1**, 111 (2005).
[18] T. Kuwamoto, K. Araki, T. Eno, and T. Hirano, Phys. Rev. A **69**, 063604 (2004).
[19] J. Kronjäger, C. Becker, P. Navez, K. Bongs, and K. Sengstock, Phys. Rev. Lett. **97**, 110404 (2006).
[20] H. Schmaljohann, M. Erhard, J. Kronjäger, M. Kottke, S. van Staa, L. Cacciapuoti, J. J. Arlt, K. Bongs, and K. Sengstock, Phys. Rev. Lett. **92**, 040402 (2004).
[21] C. Becker, P. Soltan-Panahi, J. Kronjäger, S. Dörscher, K. Bongs, and K. Sengstock, New J. Phys. **12**, 065025 (2010).
[22] A. Widera, F. Gerbier, S. Fölling, T. Gericke, O. Mandel, and I. Bloch, Phys. Rev. Lett. **95**, 190405 (2005).
[23] P. L. Pedersen, M. Gajdacz, F. Deuretzbacher, L. Santos, C. Klempt, J. F. Sherson, A. J. Hilliard, and J. J. Arlt, Phys. Rev. A **89**, 051603(R) (2014).
[24] A. Widera, F. Gerbier, S. Fölling, T. Gericke, O. Mandel, and I. Bloch, New J. Phys. **8**, 152 (2006).
[25] Based on the mean-field theory [16], the ground states of antiferromagnetic $F = 1$ spinor BECs at a positive q_B are in one of the following three phases: (a) an antiferromagnetic phase where $\rho_0^{D\approx 0} = 0$, when $q_B < U_2(1 - \sqrt{1 - m^2})$; (b) a LP phase where $\rho_0^{D\approx 0} = 1$, when $m = 0$; (c) a BA phase where $\rho_0^{D\approx 0}$ is the root of the following equation: $1 - 2\rho_0^{D\approx 0} - [(1-2\rho_0^{D\approx 0})(1-\rho_0^{D\approx 0}) - m^2]/[\sqrt{(1-\rho_0^{D\approx 0})^2 - m^2}] = q_B/U_2$.
[26] W. Zhang, D. L. Zhou, M.-S. Chang, M. S. Chapman, and L. You, Phys. Rev. A **72**, 013602 (2005).
[27] The fitting functions used in Figs. 2(a) and 2(b) are respectively $\rho_0(t) = A_0 - A_1 e^{-t/\tau_0} - A_2/(1 + A_3 e^{-t/\tau_1}) + A_4 e^{-t/\tau_2} \sin(\omega e^{t/\tau_3} t + \phi)$ and $\rho_0(t) = A_0 - A_1 e^{-t/\tau_0} - A_2 e^{-t/\tau_1} + A_4 e^{-t/\tau_2} \sin(\omega e^{t/\tau_3} t + \phi)$, where A_0, A_1, A_2, A_3, A_4, τ_0, τ_1, τ_2, τ_3, ω and ϕ are fitting parameters.
[28] We extract N_D (the number of atoms in all nonzero momentum states) from TOF images with two fitting methods which render similar results. Method 1 is suggested by Ref. [7]: we mask off all the interference peaks, and conduct a 2D Gaussian fit to the background for extracting N_D. In method 2, we plot a density profile of a TOF image through all interference peaks, and then fit the density profile with a combination of eight Gaussian functions, i.e., one function to each interference peak, and the eighth one to the broad background for extracting N_D.
[29] The normalization factor A is an integration, $\int \exp[-(k_x^2/W_x^2 + k_y^2/W_y^2 + k_z^2/W_z^2)/2] d\mathbf{k}$, over the first Brillouin zone.

VITA

Jie Jiang

Candidate for the Degree of

Doctor of Philosophy

Dissertation: SODIUM SPINOR BOSE-EINSTEIN CONDENSATES: ALL-OPTICAL PRODUCTION AND SPIN DYNAMICS

Major Field: Photonics

Biographical:

Personal Data: Born in Shanghai, China on May 01, 1987.

Education:

Completed the requirements for the Doctor of Philosophy in Photonics at Oklahoma State University, Stillwater, Oklahoma in December, 2015.

Completed the requirements for the Bachelor of Science in Optical Information Science at University of Shanghai for Science and Technology, Shanghai, China in 2009.

Professional Memberships:

American Physical Society